The Dissertation Committee for Adam Michael Crook
certifies that this is the approved version of the following dissertation:

Molecular Beam Epitaxial Growth of Rare-Earth Compounds for Semimetal/Semiconductor Heterostructure Optical Devices

Committee:

Seth Bank, Supervisor

Edward Yu

Julien Cheng

John Zhang

Mikhail Belkin

Molecular Beam Epitaxial Growth of Rare-Earth Compounds for Semimetal/Semiconductor Heterostructure Optical Devices

by

Adam Michael Crook, B.S.; M.S.E.

DISSERTATION

Presented to the Faculty of the Graduate School of

The University of Texas at Austin

in Partial Fulfillment

of the Requirements

for the Degree of

DOCTOR OF PHILOSOPHY

THE UNIVERSITY OF TEXAS AT AUSTIN

May 2012

Dedicated to my wife, Katie.

Acknowledgments

This dissertation would not have been possible without the help and support of many people. First and foremost, I would like to thank my adviser, Professor Seth Bank. His passion for science is contagious and his attention to detail is something to admire. He has been a constant source of guidance, both technical and in life. Whether he was teaching us MBE, or exchanging emails at 3 am, he has exceeded even the highest expectations I could have had when joining his group. I aspire to follow his good examples as I continue forward with my career.

I would like to thank Professors Edward Yu, Julien Cheng, Mikhail Belkin, and John Zhang for taking time out of there busy schedules to serve on my committee. Their insightful comments at my qualifier helped to shape the direction of this work.

I also would like to acknowledge Hari Nair, my fellow system Bravo grower and founding member of the LASE group. In addition to retooling, maintaining, and growing on system Bravo with me, Hari has directly contributed to the development of every aspect of this dissertation. His ability and willingness to challenge me has consistently lead to deeper understanding.

I would like to acknowledge the contributions of several collaborators who have directly added to this work. Domingo Ferrer, whose TEM images

have proven invaluable for the development of the ErAs film growth. Professor Harris's group from Stanford, who helped us out with processing when system Bravo was first coming up. Keun Woo Park, from Professor Edward Yu's group, whose scanning probe characterization of ErAs nanostructures helped to illustrate some misconceptions about ErAs growth. Jong Ho Lee from Professor Deji Akinwande's group, who has not only processed and characterized ErAs films, but is also pursuing their incorporation into devices.

I would also like to acknowledge the profound impact that my undergraduate advisor, Professor Mark Rodwell from UCSB, had on me. Without Professor Rodwell taking a chance on me during my undergraduate studies and providing the guidance and freedom to successfully execute a research project, it is hard to imagine I would be where I am today. From the post-doctoral scholars in his group (namely Erik Lind and Seth Bank), I had the opportunity to see the level of skill and commitment required to make it in research. I am also grateful for Uttam Singisetti and Zach Griffith, who taught me processing methodology capable of producing the world's fastest transistor.

Finally, I would like to acknowledge the rest of the current and former LASE group members, Erica Krivoy, Rodolfo Salas, Scott Maddox, Vaishno Dasika and Robert Chen. They have contributed in numerous ways including with MBE maintenance, growth, processing, and help with reading papers and reviewing presentations.

Molecular Beam Epitaxial Growth of Rare-Earth Compounds for Semimetal/Semiconductor Heterostructure Optical Devices

Publication No. _____

Adam Michael Crook, Ph.D.
The University of Texas at Austin, 2012

Supervisor: Seth Bank

Heterostructures of materials with dramatically different properties are exciting for a variety of devices. In particular, the epitaxial integration of metals with semiconductors is promising for low-loss tunnel junctions, embedded Ohmic contacts, high-conductivity spreading layers, as well as optical devices based on the surface plasmons at metal/semiconductor interfaces. This thesis investigates the structural, electrical, and optical properties of compound (III-V) semiconductors employing rare-earth monopnictide (RE-V) nanostructures. Tunnel junctions employing RE-V nanoparticles are developed to enhance current optical devices, and the epitaxial incorporation of RE-V films is discussed for embedded electrical and plasmonic devices.

Leveraging he favorable band alignments of RE-V materials in GaAs and GaSb semiconductors, nanoparticle-enhanced tunnel junctions are inves-

tigated for applications of wide-bandgap tunnel junctions and lightly doped tunnel junctions in optical devices. Through optimization of the growth space, ErAs nanoparticle-enhanced GaAs tunnel junctions exhibit conductivity similar to the best reports on the material system. Additionally, GaSb-based tunnel junctions are developed with low p-type doping that could reduce optical loss in the cladding of a 4 μm laser by $\sim$75%. These tunnel junctions have several advantages over competing approaches, including improved thermal stability, precise control over nanoparticle location, and incorporation of a manifold of states at the tunnel junction interface. Investigating the integration of RE-V nanostructures into optical devices revealed important details of the RE-V growth, allowing for quantum wells to be grown within 15 nm of an ErAs nanoparticle layer with minimal degradation (i.e. 95% of the peak photoluminescence intensity).

This investigation into the MBE growth of ErAs provides the foundation for enhancing optical devices with RE-V nanostructures. Additionally, the improved understanding of ErAs growth leads to development of a method to grow full films of RE-V embedded in III-V materials. The growth method overcomes the mismatch in rotational symmetry of RE-V and III-V materials by seeding film growth with epitaxial nanoparticles, and growing the film through a thin III-V spacer. The growth of RE-V films is promising for both embedded electrical devices as well as a potential path towards realization of plasmonic devices with epitaxially integrated metallic films.

Table of Contents

Acknowledgments v

Abstract vii

List of Figures xi

Chapter 1. Introduction 1

1.1 Why Rare-Earth Monopnictides? . . . 2

1.1.1 Epitaxial Metal/Semiconductor Heterostructures . . . 3

1.1.2 Rare-Earth Pnictide Material Properties . . . 3

1.1.3 Rare-Earth Pnicide Growth . . . 4

1.1.4 Rare-Earth Pnictide Devices . . . 6

1.1.5 Universal Band-Alignment Model . . . 7

1.2 Tunnel Junctions in Optical Devices . . . 8

1.2.1 High-Efficiency Solar Cells . . . 10

1.2.2 GaAs-Based Vertical Cavity Surface Emitting Lasers . . . 14

1.2.3 Mid-Infrared Diode Lasers . . . 15

1.3 RE-V Plasmonics . . . 23

1.4 Epitaxially Embedded RE-V Films . . . 24

1.5 Organization of Dissertation . . . 27

Chapter 2. Molecular Beam Epitaxy 29

2.1 Conventional III-V MBE . . . 30

2.2 Mixed Group-V Alloys . . . 31

2.3 Surface Segregation Model . . . 35

2.4 Dilute Nitrides . . . 38

2.5 Erbium Incorporation in GaAs . . . 46

Chapter 3. Low-Loss Tunnel Junctions **53**
3.1 Conventional Tunnel Junctions 53
3.2 Advanced Semiconductor Tunnel Junctions 56
3.3 Embedded Semimetallic Nanoparticles 60
3.3.1 GaAs-Based Tunnel Junctions 61
3.3.2 Microscopic Tunnel-Junction Measurements 65
3.3.3 Graded-Heterostructure Tunnel Junctions 70
3.3.4 GaSb-Based Tunnel Junctions 72
3.4 Conclusion 78

Chapter 4. ErAs Nanostructures for Optical Devices **81**
4.1 Parasitic Erbium Incorporation 84
4.2 Proximity to ErAs Nanoparticles 87
4.3 Managing Parasitic Erbium 92
4.4 Conclusions 96

Chapter 5. RE-V Plasmonics **98**
5.1 Rare-Earth Pnictide IR-Absorption 98
5.2 Optical Properties of ErAs Films 102
5.3 Conclusions 106

Chapter 6. ErAs Film Growth **107**
6.1 Nanoparticle-Seeded Film Growth Method 108
6.2 Optical Investigation of ErAs Film Overgrowth 116
6.3 Conductivity of Erbium Arsenide Films 120
6.4 Erbium Incorporation Model 125

Chapter 7. Conclusion **128**

Bibliography **153**

List of Figures

1.1 Illustration of the surface of GaAs surface (top) and ErAs surface (bottom). The two distinct phases of GaAs overgrowth of ErAs are illustrated. 5

1.2 Illustration of the universal band-alignment model for Er-V compounds on various substrates. Compiled by Bobby Brar. . 8

1.3 Schottky barrier as a function of alloy composition for ErAs films grown on varying alloys of InAlAs/InGaAs on InP substrates. The open circles are measurements from electrical conductivity and the solid circle is from CV measurements. From [41]. 9

1.4 Illustration of conventional tunnel junction operation (a) forward bias (solar cell operation) and (b) reverse bias (injector for laser). Arrows indicate direction of electron tunneling. The gradients in majority carrier concentrations give the direction of majority carrier current on each side of the junction. . . . 11

1.5 Air mass 1.5 (AM1.5) spectrum of solar energy flux density. From [43]. 12

1.6 Maximum output power for room-temperature, continuous-wave operation of single laser results. Type-I diode lasers (green circles) show decreasing power with wavelength. Interband cascade lasers (blue triangles) show peak performance around 3.7 μm emission wavelength with degradation at shorter and longer wavelengths. Quantum cascade lasers (red squares) show bigh-power operation for $\lambda \geq 3.8\,\mu$m, the record wavelength for InGaAs/AlInAs QCLs on InP. 16

1.7 Internal loss and efficiency for two mid-IR diode laser designs. Despite the lower interal loss from the narrow core design, there is no improvedment in internal efficiency, which monotonically descreases with wavelength. 17

1.8 Plot of the laser emission energy as a function of the As mol fraction in the QW active region. The calculated split-off energy reduces faster than the emission wavelength contributing to parasitic loss and poor high-temperature performance. . . . 19

1.9 Characteristic temperature for type-I GaSb-based diode lasers as a function of split-off energy to emission wavelength separation. 20

1.10 (a) Polarization dependent absorption spectra for 2 ML ErSb superlattice. (b) Wavelength of the absorption peak for orthoganol polarizations as a function of nanoparticle deposition. From [72] 25
1.11 Epitaxially embedded ScErAs film, lattice matched to GaAs. The GaAs overgrowth exhibits planar defects. From [20] . . . 26

2.1 Schematic of a molecular beam epitaxy chamber 29
2.2 Sample structures for cladding alloy calibrations via XRD and QW active region characterization via XRD and PL 32
2.3 Photoluminescence spectra for laser core structures grown with varying substrate temperature. 33
2.4 Photoluminescence spectra for laser core structures grown with varying antimony overpressure. 34
2.5 As mol fraction, measured by HR-XRD, for varying As flux and growth temperatures 36
2.6 Illustration of incorporation from a surface segregation layer . 37
2.7 Steady state nitrogen incorporation in surface segregation model and experimental nitrogen incorporation at varying substrate temperature and growth rate 41
2.8 Nuclear reaction analysis Rutherford back-scattering (NRA-RBS) results for nitrogen incorporation of GaNSb samples grown at 0.66 μm/hr. The total nitrogen is obtained from random axis yield while the substitutional nitrogen is obtained from the difference between random axis and channeling yields when aligned to $< 100 >$, $< 110 >$, and $< 111 >$ directions. Adapted from [104] 43
2.9 Photoluminescence spectra for GaInSb quantum well grown with and without a nitrogen pulse during the QW. Adapted from [104] 44
2.10 Illustration of conventional ErAs/GaAs heterostructure growth. (a) Erbium initially accumulates at the surface. (b) When the critical surface areal density for ErAs nanoparticle formation is reached, ErAs nanoparticels form. The particles seed as $\sim$4 ML particles on each side and expand laterally until a full film is formed. (c) GaAs overgrowth of ErAs films results in two distinct island orientations due to the mismatch in rotational symmetry. (d) The GaAs overgrowth is highly defective due to inversion domain boundaries and micro-twins where the islands meet. (e) If the ErAs deposition is limited to self-assembled nanoparticles and the GaAs overgrowth is seeded by the exposed GaAs. (f) The ErAs nanostructures can be embedded in single phase GaAs. 47

2.11 Cross-sectional TEM image of ErAs nanoparticle embedded at an GaAs/AlAs interface. 48
2.12 High-resolution X-ray diffraction of superlattice consisting of 60 periods of (1.2 ML Eras / 20 nm GaAs). As grown, the sample shows anomalous peaks that are suppressed with thermal annealing at 800°C under AsH_3 overpressure. 50
2.13 High-resolution X-ray diffraction of superlattice consisting of 40 periods of (1.2 ML ErAs / 30 nm GaAs). As grown, the sample shows a shoulder on the substrate/zero-order superlattice peak that is suppressed with thermal annealing at 800°C under AsH_3 overpressure. 51

3.1 Illustration of conventional tunnel junction operation under forward and reverse biases. The solid circles represent electrons and the circle outlines represent holes. Only the majority carrier profiles are represented. The arrow shows the tunneling direction for electrons. 55
3.2 Band structure of type-II heterostructure tunnel junction . . . 57
3.3 Band structure of defect-enhanced tunnel junction 59
3.4 Tunnel Junction Structure 63
3.5 Conductivity of ErAs nanoparticle enhanced tunnel junctions with varying ErAs deposition 64
3.6 Illustration of sample structure and measurement setup for conductive atomic force microscopy of ErAs nanoparticle enhanced tunnel junctions. From [125]. 66
3.7 Conductive atomic force microscopy of ErAs nanoparticle enhanced tunnel junction grown at varying substrate temperature 67
3.8 Conductive atomic force microscopy of ErAs nanoparticle enhanced tunnel junctions with varying ErAs deposition 69
3.9 Calculated band diagrams for GaAs tunnel junctions with GaInAs graded n-sides with and without ErAs nanoparticles embedded at the tunnel junction interface. The ErAs nanoparticle width is increased for illustration. 71
3.10 Conductivity vs voltage for abrupt GaAs and graded GaInAs tunnel junctions with and without ErAs nanoparticle embedded at the tunnel junction interface. 72
3.11 Calculated band profiles for conventional GaSb tunnel junctions and ErSb nanoparticle enhanced tunnel junctions of varying p-type doping. 74

3.12 Current density of ErSb nanoparticle enhanced tunnel junctions with varying p-type doping 76
3.13 Band diagram for prototype laser employing n-type cladding and ErSb nanoparticle-enhanced tunnel junction to replace the p-type cladding. 78
3.14 Calculated cladding loss from overlap of optical mode (shown in bottom left corner) with each layer for three cladding designs: (a) conventional low-doped p-type cladding, (b) n-type cladding with conventional tunnel junction, and (c) n-type cladding with ErSb nanoparticle-enhanced tunnel junction and reduced p-type doping. 79

4.1 Photoluminescence structure used to quantify the optical quality of III-V layers. The AlAs barriers prevent photogenerated carriers from diffusing to the surface or the underlying epitaxial layers, providing maximum sensitivity to non-radiative recombination causing defects. 83
4.2 Band diagram of photoluminescence structure used to quantify the optical quality of III-V layers. Only carriers generated by absorbing the pump beam between the carrier blocking layers can contribute to emission. Because the carrier blocking layers prevent photogenerated carriers from diffusing to the underlying epitaxial layers or the surface, where nonradiative recombination would be expected, only defects in the PL structure are probed. 84
4.3 Peak PL intensity for PL structures, shown in Fig 4.1, with varying erbium cell temperature from the idle temperature of 500°C to the growth temperature of ∼1000°C. 86
4.4 Photoluminescence structure for varying ErAs nanoparticle proximity to QW in PL structures 88
4.5 Peak photoluminescence intensity for varying spacer thickness between AlAs carrier blocking layer and embedded ErAs nanoparticle layer (structure illustrated in Figure: 4.4b). The lowest PL intesities are attributed to enhanced Er incorporation into the QW. The increased PL intensities are attributed to reduced surface concentration after the AlAs and ErAs interfaces. . . . 89
4.6 Peak photoluminescence intensity for varying spacer thickness between InGaAs quantum well and embedded ErAs nanoparticle layer(structure illustrated in Figure: 4.4a). The lowest PL intesities are attributed to enhanced Er incorporation into the QW. The increased PL intensities are attributed to reduced surface concentration after the AlAs and ErAs interfaces. . . . 90

4.7 Secondary ion mass spectrometry scans of erbium and oxygen concentrations in photoluminescence structures grown with the erbium cell hot throughout the growth. 91

4.8 Illustration of the sample structure utilized to investigate methods of overcoming parasitic erbium incorporation into PL structures grown after ErAs nanoparticle layers. The growth interruption required to cool the erbium cell was ∼100 min. 93

4.9 Photoluminescence spectrum for sample grown with the erbium cell idle and no ErAs nanoparticle layer as well as a sample that was As-capped after an ErAs nanoparticle layer, capped with 5 nm GaAs spacer. 94

4.10 Photoluminescence spectrum for sample grown without ErAs nanoparticle layer as well as samples with 1 and 10 nm GaAs spacers. 95

4.11 Peak PL intensity for samples grown with varying GaAs spacer layers after nanoparticle growth, prior to the growth interruption to cool the erbium cell. 97

5.1 Transmission spectra for ErAs nanoparticle superlattice samples of varying ErAs deposition. 99

5.2 The transmission spectra of the 0.25 ML ErAs nanoparticle superlattice with PL spectrum for GaInAs quantum well photoluminescence structure overlaid. 100

5.3 Photoluminescence spectra of PL structures growth with and without ErAs nanoparticle layers. The absorption feature of the ErAs nanoparticles is spectrally aligned to the PL emission peak, shown in Fig. 5.2, however there is nealy no difference in PL intensity and no observable shift in the emission wavelength, as would be expected for Purcell enhancement of spontaneous emission. 101

5.4 (a) Reflectivity of 500 nm ErAs film. The Drude edge appears around 3000 nm. (b) Transmission through 500 nm ErAs film. The two absorption peaks near 2200 and 2800 nm are attributed to band-to-band transitions away from zone center. 104

5.5 Real, $\epsilon^{'}$, and imaginary, $\epsilon^{''}$, parts of dielectric constant extracted using *RefFIT* from the transmission and reflection data of 500 nm ErAs film (Fig. 5.4). The plasma frequency, λ_p, is apparent where $\epsilon^{'}$ crosses zero. 105

6.1 Illustration of the atomic structure of the (100) surface. (a) two unique phases of GaAs surface. (b) ErAs surface 108

6.2 Illustration of the nanoparticle-seeded film growth method. (a) At the initation of an erbium flux, erbium accumulates at the GaAs surface. (b) Beyond the critical areal density for nanoparticle formation, ErAs nanoparticles precipitate out. The nanoparticles are embedded at the surface and have characteristic size of ∼4 ML. (c) The nanoparticles are overgrown with a thin GaAs spacer layer that is seeded by the exposed substrate. (d) ErAs film growth persists by diffusion of erbium adatoms to the nanoparticle seed layer which expands laterally until a full film is formed. The GaAs spacer layer serves as a template for single phase III-V overgrowth. 110

6.3 Cross-section TEM of multi-layer structure consisting of ErAs films with successively thicker GaAs spacer. The GaAs spacer thickness is overlaid on the film. The top layer has no GaAs spacer, which represents the conventional layer-by-layer growth method. 111

6.4 High-resolution TEM of (a) 5 ML ErAs film grown with the conventional (0 nm spacer thickness) and (b) 5 ML ErAs film growth with the nanoparticle-seeded film growth method (1 nm spacer thickness). The conventionally grown film clearly exhibits planar defects in the GaAs overgrowth while such defects are suppressed in the nanoparticle-seeded ErAs film. 113

6.5 High-resolution TEM image of the nanoparticle-seeded ErAs layer grown with 3.0 nm GaAs spacer. The two distinct nanoparticle layers (denoted lower & upper) correspond to the nanoparticle seed layer (lower) and the parasitic surface nanoparticle layer (upper). 114

6.6 Cross-section TEM of multi-layer structure consisting of ErAs films with successively higher ErAs depositions. (a) bottom 4 layers consisting of 1.33 ML ErAs nanoparticle seed layer, 1.83 ML, 2.33 ML, and 2.83 ML from bottom to top. (b) High-resolution TEM of nanoparticle seed layer. (c) High-resolution TEM of 5.33 ML ErAs film. The vertical extent of the nanoparticle-seeded films appears to be constant with much less roughness for the full films than the nanoparticle seed layer. 116

6.7 Photoluminescence spectra for ErAs-free control sample, conventionally grown ErAs film, and nanoparticle-seeded ErAs film. While the conventional ErAs film does not show any PL yield above the noise floor, the nanoparticle-seeded ErAs film exhibits only ∼10× degradation in the peak PL intensity. 118

6.8 Illustration of the sample structure and contact scheme for TLM structures to measure the electrical conductivity of the ErAs films. 121

6.9 Resistance vs Length for 10 ML ErAs film grown with nanoparticle-seeded film growth method. 121

6.10 Sheet resistance and corresponding conductivity of ErAs films grown with the nanoparticle-seeded film growth technique. The dashed line is the calculated conductivity for surface roughness scattering limited transport with roughness characterized by the nanoparticle seed layer. 122

6.11 Temperature dependence of resistivity of 5 ML and 10 ML ErAs films grown with the nanoparticle-seeded film growth method. The resistivity is normalized to the room temperature conductivity. 124

6.12 Calculated erbium concentration profiles for varying nanoparticle-seeded film growth conditions. (a) Varying erbium flux with constant GaAs spacer thickness. (b) Varying GaAs spacer thickness with constant erbium flux. The x-intercept corresponds to the location of the nanoparticles and the y-intercept corresponds to the surface concentration of erbium. 126

Chapter 1

Introduction

This dissertation focusses on enhancing optical devices through the incorporation of semimetallic rare-earth monopnictide[1] (RE-V) materials (specifically ErAs and ErSb). Previous Investigations of ErAs/GaAs tunnel junctions have demonstrated significant enhancement in electrical properties of GaAs tunnel junctions. However, a detailed investigation into the effects of integrating RE-V nanostructures into III-V optical devices had not been conducted. Several groups have noted parasitic erbium incorporation into layers grown with the erbium cell hot but have not reported the implications for optical devices. In fact, a previous attempt at improving the efficiency of tandem solar cells by incorporating ErAs nanoparticle enhanced tunnel junctions failed to demonstrate an improvement in power conversion efficiency [1]. In this chapter, the advantages of incorporating RE-V nanostructures into optical devices will be introduced. Specifically, Section 1.1 introduces the RE-V materials system and discusses the properties of RE-V materials that make them well-suited to epitaxially embedded metal/semiconductor heterostructures. Section 1.2 details applications requiring high-conductivity, low-optical-loss tunnel junc-

[1] Pnictide refers to a compound with a group-V element, monopnictide is a single group-V rather than an alloy.

tions, which cannot be realized with conventional approaches. Section 1.3 will discuss the potential for epitaxially integrated RE-V plasmon-enhanced devices. Section 1.4 discusses the shortcomings in the conventional approach to epitaxially embedded ErAs films and introduces the nanoparticle-seeded film growth method. Finally, Section 1.5 details the organization of this dissertation.

1.1 Why Rare-Earth Monopnictides?

Metal/semiconductor heterostructures are integral to the operation of many optoelectronic devices.[2] It comes as no surprise; metal contacts have been intensely researched for several decades. Conventional *ex situ* metallization results in highly non-ideal interfaces, due to the difficulty completely removing native oxides and the formation of interfacial alloys. Most of the effort in metal/semiconductor heterostructures has focused on removal of native oxide, passivation of semiconductor surfaces, and designing alloys to mitigate the poor surface quality. An attractive alternate approach to improve metal/semiconductor interfaces is to deposit metals *in situ* directly on the semiconductor surface, such that no surface oxide is present. For metals with compatible crystal structures, epitaxial contacts not only lack an interfacial oxide but also have the potential to have a well-ordered interface. Rare-Earth pnictides are particularly attractive for epitaxially embedded contacts because

[2]Metal contacts are required to source and sink current as well as modify electrical fields within the device.

the rocksalt crystal structure is similar to III-V's zinc blende and the cubic lattice constants are comparable. Additionally, the interface between RE-V and III-V is thermodynamically stable for both ErAs/GaAs and ErSb/GaSb.

1.1.1 Epitaxial Metal/Semiconductor Heterostructures

Several epitaxial metals have been demonstrated on semiconductors. The most successful metal/semiconductor heterostructures are the silicides on silicon, which can be grown epitaxially through solid phase reactions [2–4] as well as by molecular beam epitaxy (MBE) [5, 6]. Epitaxial metal/semiconductor heterostructures have also been investigated on the compound semiconductors: aluminum has been or grown on GaAs by MBE [7, 8]; iron can be grown epitaxially on GaAs [9], but the interface is not stable [10], and the growth conditions are not compatible with normal III-V growth [7, 8]. Other material systems have also been demonstrated, such as the transition metal/group-III compounds [11, 12] and rare-earth pnictides (RE-V) [13]. But only the RE-V materials result in a thermodynamically stable interface. Like most metallic structures, the RE-V compounds have been relegated to the device periphery due to incompatible material properties for epitaxial growth and overgrowth, namely the need for both interfacial stability and crystal structures compatibility [13].

1.1.2 Rare-Earth Pnictide Material Properties

This dissertation focusses on ErAs and ErSb materials grown on GaAs and GaSb substrates respectively. The relevant bulk materials properties for ErAs and ErSb are given in Table 1.1. There is significant overlap of the conduction and valence bands making ErAs and ErSb semimetallic [14]. ErAs forms in a rocksalt crystal structure with a cubic lattice constant that is only 1.6% mismatched from the GaAs substrate. ErSb has similar electrical and structural properties, but only a 0.2% mismatch to GaSb substrates. Both materials result in a thermodynamically stable interface when grown on their respective III-V substrate. However, both materials are highly-reactive and will completely oxidize at room temperature in ambient conditions if no diffusion barrier is present on the surface.

Table 1.1: Physical Properties of ErAs and ErSb

	ErAs [15, 16]	ErSb [17, 18]
crystal structure	rocksalt	rocksalt
lattice constant	5.7427 Å	6.1081 Å
substrate	GaAs	GaSb
lattice mismatch	1.6%	0.2%
bulk conductivity	70 $\mu\Omega$cm	30 $\mu\Omega$cm
electron concentration	1.8×10^{20} cm^{-3}	$\sim3\times10^{20}$ cm^{-3}
electron mobility	$\sim$1100 cm^2/Vs	$\sim$700 cm^2/Vs
hole concentration	3.3×10^{20} cm^{-3}	
hole mobility	$\sim$540 cm^2/Vs	
Schottky barrier	$\sim$0.88 eV	0.5$-$0.6 eV

1.1.3 Rare-Earth Pnicide Growth

Investigation into rare-earth monopnictides began in an effort to reproduce the success of silicides on silicon in compound semiconductors. Palmstrøm and Sands initially reported MBE growth of ErAs on GaAs in the late 1980s [15, 19, 20]. The defects they observe can be attributed to stacking faults in the III-V overgrowth related to the additional symmetry of the rock-salt crystal structure compared to the zinc blende [15, 17, 21]. The symmetry of the (100) surface of ErAs and GaAs is illustrated in Fig. 1.1. Overgrowth of the RE-V films with III-V results in island formation of the two distinct phases of the III-V. When the islands grow together stacking faults form at the boundary. The surface energetics of GaAs and ErAs present an additional challenge to GaAs overgrowth of ErAs. This will be discussed in detail in Chapter 2.

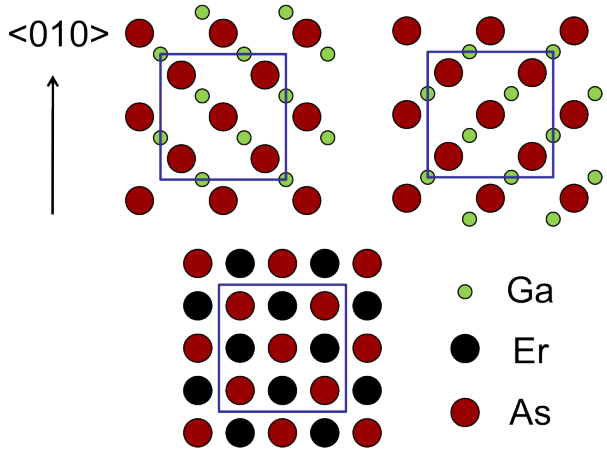

Figure 1.1: Illustration of the surface of GaAs surface (top) and ErAs surface (bottom). The two distinct phases of GaAs overgrowth of ErAs are illustrated.

ErAs heterostructures have been epitaxially embedded into compound semiconductor devices with high-quality overgrowth by two general methods: researchers doping GaAs layers with high erbium concentration observed ErAs precipitates [22–26]; additionally, the mismatch in rotational symmety can be overcome by limiting the RE-V growth at a III-V surface to self-assembled nanoparticles and seeding overgrowth with the underlying III-V material. Both approaches result in high-quality epitaxially embedded heterostructures and composite materials [27–30].

1.1.4 Rare-Earth Pnictide Devices

Applications for RE-V materials involve epitaxially embedded nanostructures. Embedding ErAs nanoparticles at the interface of p^+-n^+ GaAs tunnel junctions was shown to greatly enhance the tunneling current in both forward and reverse bias, as well as eliminate the Esaki peak [31]. Similar tunnel junctions were employed in tandem solar cells [1], and heterodyne photomixers for terahertz generation [32]. Composite materials employing a random alloy of ErAs precipitates embedded in a GaInAs host matrix show promise for enhancing the thermoelectric figure of merit ZT [33–36]. Other RE-V materials have also been investigated for enhanced thermoelectric materials [37, 38]. Superlattices of ErAs nanoparticles have been employed as fast-photoconductive switches for terahertz power generation [39, 40]. While the several successful applications to devices demonstrate the utility of heterostructure systems with very different material properties, all of these de-

vices utilize the RE-V nanostructures either as phonon scattering centers or non-radiative recombination centers. As such, the devices are insensitive to degradation in optical quality of the surrounding materials associated with the incorporation of the nanostructures.[3] Incorporation into optical devices with demanding requirements for optical quality, such as high-efficiency lasers and solar cells, require detailed investigation into the integration of RE-V nanostructures with optically active materials.

1.1.5 Universal Band-Alignment Model

Perhaps the most important property of RE-V heterostructure materials is the heterojunction discontinuity at the RE-V/III-V interface (the Schottky barrier height). To a good approximation, the Schottky barrier in RE-V materials can be determined by assuming that the position of the RE-V Fermi-level is constant, in terms of absolute energy, and the barrier height will track the electron affinity of the semiconductor material. This model is illustrated in Fig. 1.2 for Er-V compounds on InAs, GaAs, and InP substrates. The model works very well for films of ErAs connected contacting materials of varying alloy composition (shown in Fig. 1.3) [41]. Measurements of ErAs band-alignment on one material system, such as GaAs, yields an ac-

[3] In the case of the tandem solar cell of Ref. [1] the devicee would be sensitive to reduction of the carrier lifetime due to the incorporation of parasitic erbium. However, in the employed device structure, the bandgaps where chosen to close together, such that the top cell had excess absorption for current matching, masking any effect of erbium doping. Note that the tandem solar cell employing ErAs nanoparticles has a lower power conversion efficiency than the single-junction GaAs control.

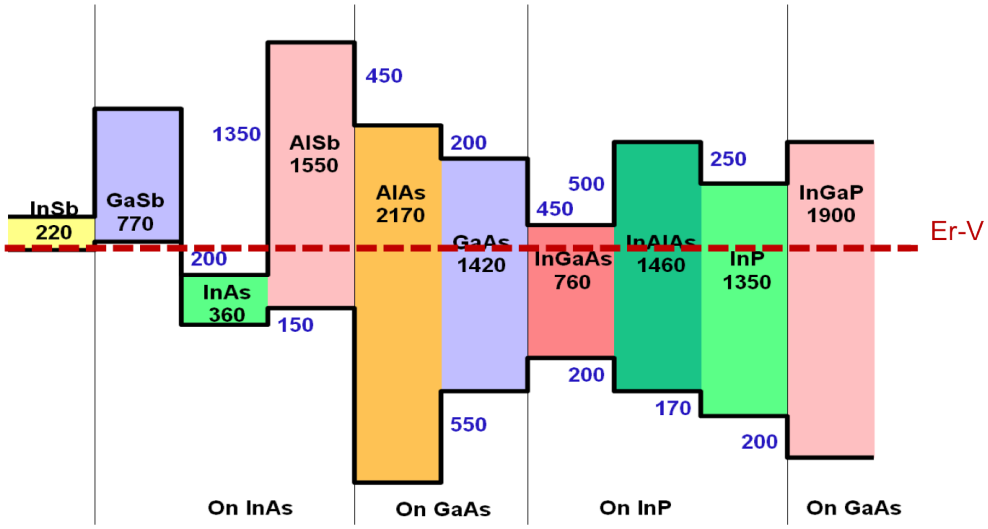

Figure 1.2: Illustration of the universal band-alignment model for Er-V compounds on various substrates. Compiled by Bobby Brar.

curate prediction of the band-alignments for materials on other substrates; however, devices utilizing heterostructures and composites of RE-V materials are generally very sensitive to the exact value of the Er-V level. For example, conductivity of RE-V Schottky contacts, as well as nanoparticle-enhanced tunnel junctions, depends exponentially on the pinning position of the ErAs nanoparticles [41, 42]. The dark current of photomixers also has an exponential dependence on the Schottky barrier height as the conduction in the nominally undoped semiconductor is dominated by the Fermi-level position of the nanoparticles with respect to the host material band edges. The same is true for thermoelectric materials employing RE-V nanostructures.

Nanostructured RE-V materials show very similar band alignments to

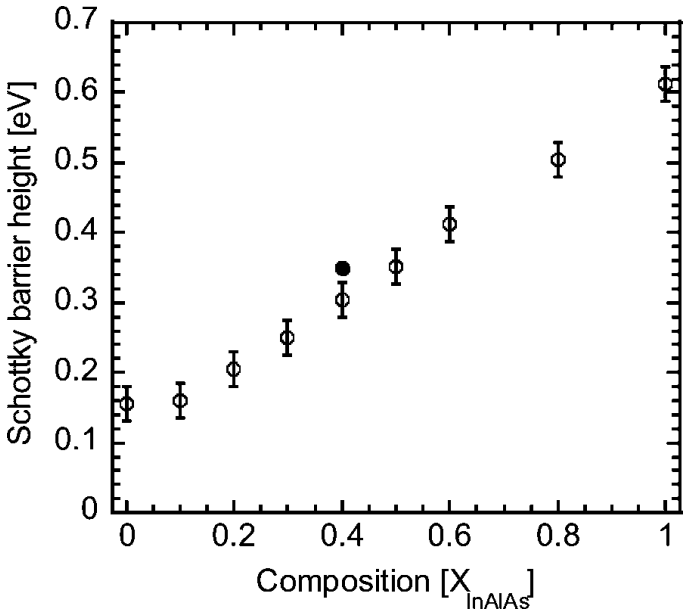

Figure 1.3: Schottky barrier as a function of alloy composition for ErAs films grown on varying alloys of InAlAs/InGaAs on InP substrates. The open circles are measurements from electrical conductivity and the solid circle is from CV measurements. From [41].

the films, however morphology and strain appear to be important in shifting the Schottky barrier height. The implications for tunnel junction conductivity will be discussed in detail in Chapter 3.

1.2 Tunnel Junctions in Optical Devices

Here, optical devices which could benefit from tunnel junctions with simultaneously high electrical conductivity and low optical loss are discussed. Heavily doped $p-n$ junctions can have sufficiently narrow depletion widths such that quantum mechanical tunneling between the conduction and valence band states can become favorable. As such, the tunnel junctions can be used to convert electron-current in an n-doped layer to hole-current in a p-doped layer with minimal voltage dropped across the tunnel junction. This is particularly attractive for devices requiring series connection of $p-n$ junctions, such as multi-junction solar cells, or those with parasitic losses associated with a particular carrier population, such as long-wavelength lasers and VCSELs. Figure 1.4 illustrates conventional tunnel junctions used to source or sink current. Under forward bias operation, the tunnel junction acts as a recombination center. Electrons travel toward the tunnel junction on the n-side, and holes travel toward the tunnel junction on the p-side. In reverse bias, the junction sources electrons and holes that are directed away from the tunnel junction on the n and p-side respectively.

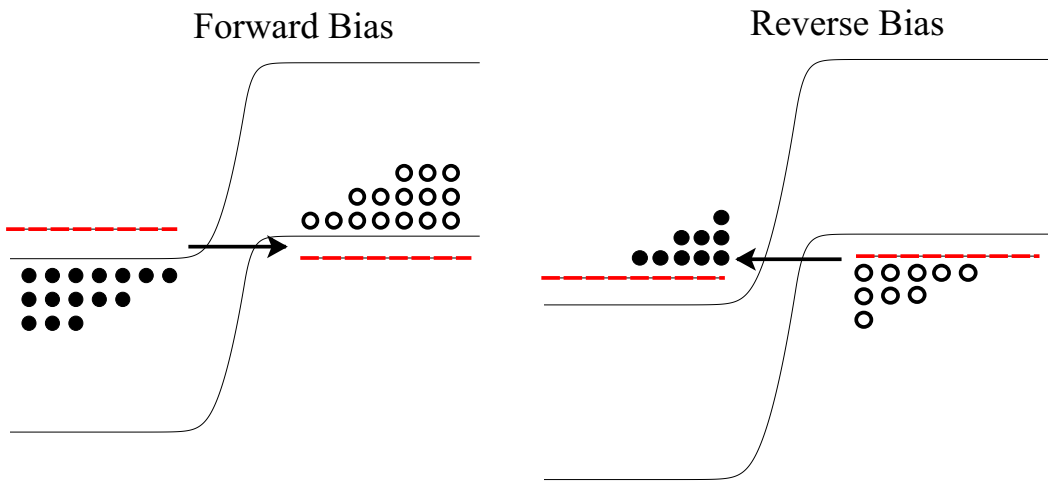

Figure 1.4: Illustration of conventional tunnel junction operation (a) forward bias (solar cell operation) and (b) reverse bias (injector for laser). Arrows indicate direction of electron tunneling. The gradients in majority carrier concentrations give the direction of majority carrier current on each side of the junction.

1.2.1 High-Efficiency Solar Cells

Harnessing of solar radiation is the most promising, inexhaustible, clean-energy technology. Semiconductor photovoltaics absorb solar radiation with energy in excess of the bandgap and convert the photons into electrical energy. Because the photogenerated electron-hole pairs can only be extracted with a maximum voltage equal to the bandgap of the semiconductor[4], efficiency is limited by the quantum defect (the difference of the energy of the photon and the bandgap energy of the semiconductor). The broad spectrum of the

[4]The actual extraction voltage is set by the separation of the quasi-Fermi levels in the solar cell, wich is less than the bandgap due to the finite temperature of the carriers.

solar radiation (shown in Fig. 1.5) limits the power conversion efficiency of a single junction to 29% [44]. The most successful approach to improve the efficiency of photovoltaic energy conversion is to employ multiple junctions with varying bandgap energy. In high-efficiency, multi-junction solar cells, the junctions are serially connected such that the largest bandgap junction absorbs the highest energy photons before they reach the next junction. Because the cells are transparent to the radiation that is below their bandgaps, the maximum energy from each photon is extracted. The interfaces between the

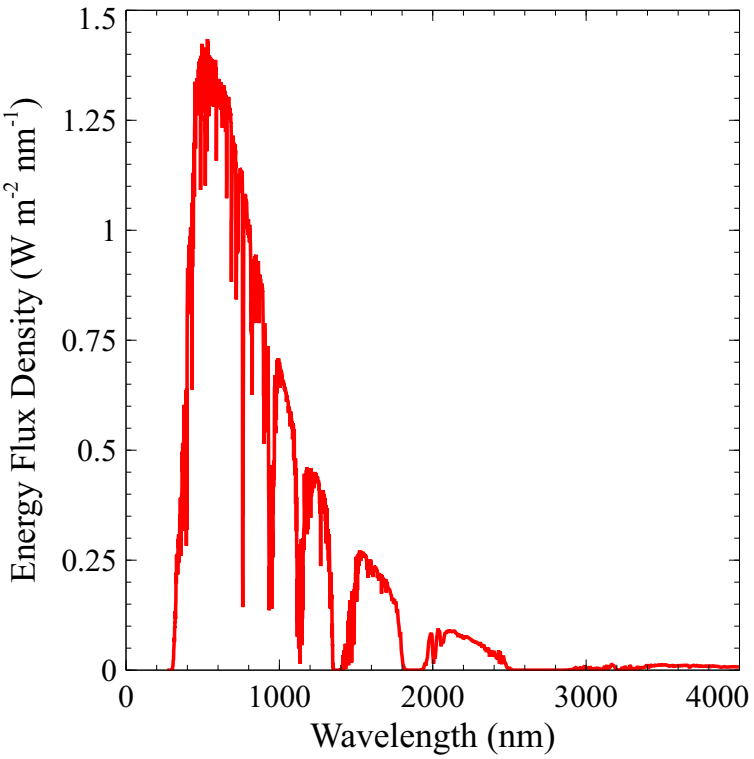

Figure 1.5: Air mass 1.5 (AM1.5) spectrum of solar energy flux density. From [43].

serially connected junctions is a p-n junction biased in the opposite direction. To prevent parasitic voltage drop at the interface, a tunnel junction can be used to recombine the electron current from on cell with the hole current from the other.

The tunnel junctions located between subsequent cells are required to be transparent at the photon energies below the bandgap of the junction that directly precedes it[5]. This is problematic for conventional tunnel junctions which have an exponential degradation in tunneling probability with bandgap. Embedding ErAs nanoparticles at the interface of GaAs $p-n$ junctions has been shown to greatly improve the tunnel junction conductivity [31]. The semimetallic ErAs nanoparticles break the tunneling process into a two steps, each with reduced height and width. The tunnel junction essentially has tunneling performance of small bandgap material with the absorption properties of the wide bandgap semiconductor. Solar cells employing such tunnel junctions have been demonstrated in tandem solar cells in the AlGaAs/GaAs material system [1]. While such tunnel junctions showed dramatic performance increase compared to the conventional tunnel junction, the efficiency of the tandem cell was not improved over the GaAs control or even other reports in the same material system [45].

This apparent discrepancy could be due to parasitic erbium incorpo-

[5]Absorption in the tunnel junction not only reduces the current by eliminating photons that would have been absorbed in subsequent cells, but also reduces the voltage due to the oposite polarity of the tunnel junction.

ration into layers grown with the erbium cell hot but the shutter closed [46]. Detailed investigation of the incorporation of ErAs nanostructures in optical devices is presented in detail in Chapter 4. It is interesting to note, however, the current world record solar cell efficiency (Solar Junction has NREL verified 43.5% efficiency) is held by a company that also has a patent disclosure filed for the integration of ErAs nanoparticle-enhanced tunnel junction with dilute-nitride materials [47].

1.2.2 GaAs-Based Vertical Cavity Surface Emitting Lasers

Tunnel junctions are used in VCSELs for both conventional and intracavity structures: buried tunnel junctions can achieve current confinement in intracavity contacted VCSELs [48]; Replacing the p-type distributed Bragg reflector mirror (DBR) with an n-type DBR and a tunnel junction can reduce electrical and optical losses of the DBR [49]. The ability to "hide" the tunnel junction in an optical null of the standing wave reduces the optical loss requirements for the tunnel junctions in VCSELs. Heavily-doped tunnel junctions can meet the requirements of VCSELs on both InP and GaSb-based VCSELs due to the availability of low bandgap materials and favorable band alignments for tunnel junction fabrication; however, the large native bandgap of GaAs and the lack of alloys with favorable band discontinuities, makes growth of highly conductive tunnel junctions particularly problematic.

One approach that has yielded high-conductivity tunnel junctions on GaAs is to use low temperature grown GaAs near the tunnel junction inter-

face. This approach is not suitable for incorporation into VCSELs (particularly those employing dilute-nitride active regions) due to the thermal budget required for growth of the top DBR.

ErAs nanoparticle-enhanced tunnel junctions are attractive for VCSELs because of the high current density [50] and the thermal stability of the ErAs/GaAs interface.

1.2.3 Mid-Infrared Diode Lasers

High-power, high-efficiency, room temperature (RT), continuous-wave (CW) operation of diode lasers will meet the requirements of compact sources for a number of applications such as: tunable diode laser absorption spectroscopy (TDLAS) for industrial gas monitoring of chemicals with molecular absorption in the $2-5\,\mu$m wavelength region [51, 52], mid-infrared free-space communication in the $3-4\,\mu$m band - especially near $3.8\,\mu$m - where atmospheric absorption (mainly due to water vapor and carbon dioxide) is low [53], laser surgery and medical diagnostic sources where human tissue has strong absorption in the region [54], as well as missile countermeasure applications requiring $4.2\,\mu$m sources [55]. The three primary approaches to semiconductor sources in the region are type-I diode lasers, type-II interband cascade lasers (ICLs) and quantum cascade lasers (QCLs). Figure 1.6 plots the maximum output power for RT-CW operation reported for each of the technologies as a function of wavelength. Type-I diode lasers exhibit high output powers at short wavelengths, but efficiency degrades and output power drops with

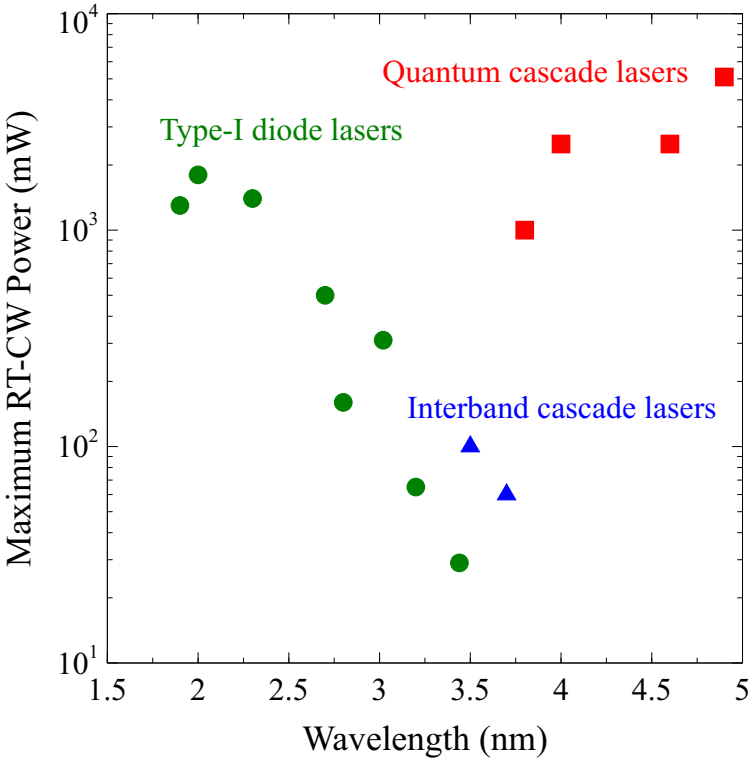

Figure 1.6: Maximum output power for room-temperature, continuous-wave operation of single laser results. Type-I diode lasers (green circles) show decreasing power with wavelength. Interband cascade lasers (blue triangles) show peak performance around 3.7 μm emission wavelength with degradation at shorter and longer wavelengths. Quantum cascade lasers (red squares) show bigh-power operation for $\lambda \geq 3.8\,\mu$m, the record wavelength for InGaAs/AlInAs QCLs on InP.

extension of the emission wavelength. Similarly, QCLs exhibit high power operation over the entire range that CW-RT operation ($\lambda \geq 3.8\,\mu$m); however, output powers decrease at shorter wavelengths and thermal management of the increasing threshold power density limits the CW operation. Like QCLs, ICLs suffer from thermal management problems. Despite this, RT-CW operation has been demonstrated over most of the operating range, but output powers and efficiency are uniformly low.

This section will focus on the extension of the operating wavelength of type-I diode lasers in the $3-4\,\mu$m wavelength range. Figure 1.7 shows the internal loss and the external efficiency of type-I diode lasers from the Belenky group. As the wavelength increases, the internal loss increases, and there is a corresponding reduction in the external efficiency. The conventional approach to extending the emission wavelength is to increase the alloy composition of the small bandgap material in the quantum well active region. In the GaSb material system, this is accomplished by adding indium to the quantum well. Because of the large lattice constant of InSb and GaSb, the additional indium must be accompanied by an increasing arsenic composition to meet strain requirements. Figure 1.8 shows the emission energy of lasers with varying arsenic mole fraction in the QW active region. Increasing the arsenic concentration results in the reduction of the valence band discontinuity between the QW and barriers in the core of the laser active region. The reduction in the valence band confinement has been addressed by incorporating quinary alloys as the barrier material; However, the reduced split-off band separation (Δ_{so})

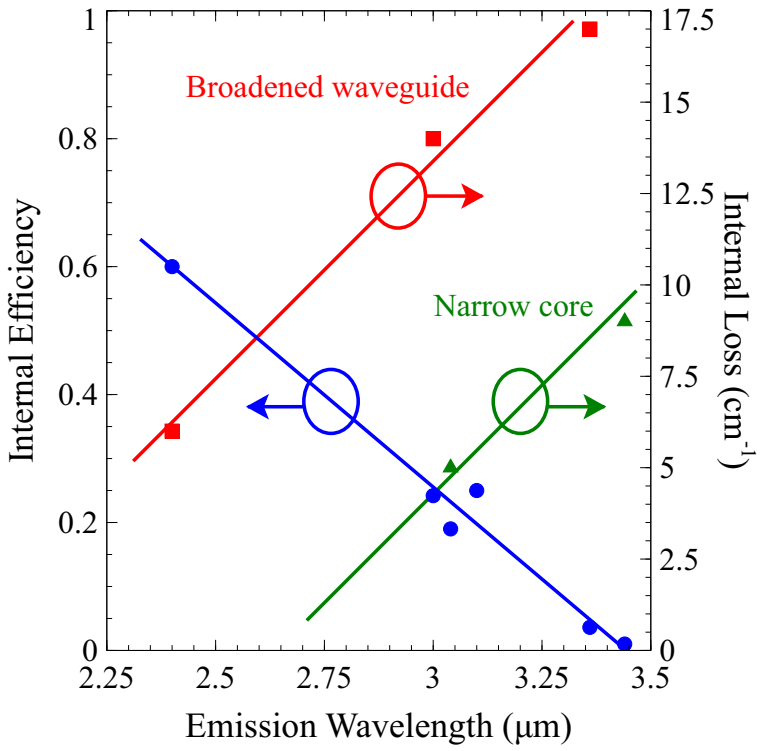

Figure 1.7: Internal loss and efficiency for two mid-IR diode laser designs. Despite the lower interal loss from the narrow core design, there is no improvedment in internal efficiency, which monotonically descreases with wavelength.

for arsenic containing materials contributes to parasitic losses and cannot be overcome with conventional approaches. The importance of Δ_{so} on room tem-

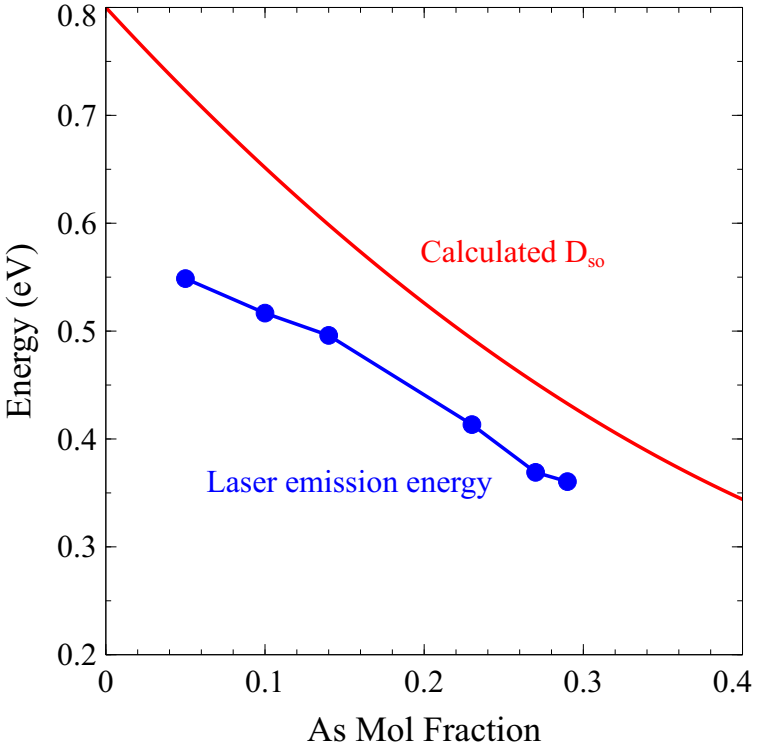

Figure 1.8: Plot of the laser emission energy as a function of the As mol fraction in the QW active region. The calculated split-off energy reduces faster than the emission wavelength contributing to parasitic loss and poor high-temperature performance.

perature laser performance can be seen in the characteristic temperature (T_0) of GaSb lasers of varying emission wavelength. Figure 1.9 plots the characteristic temperature for lasers with varying difference in energy between the Δ_{so} and emission wavelength. The difference in Δ_{so} and emission energy decreases with increasing emission wavelength, and there is a corresponding reduction in

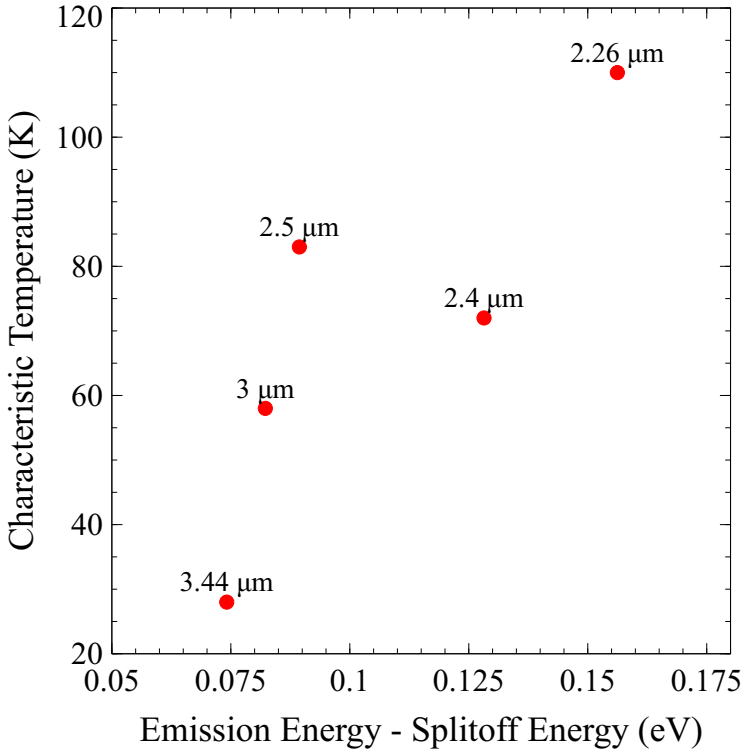

Figure 1.9: Characteristic temperature for type-I GaSb-based diode lasers as a function of split-off energy to emission wavelength separation.

T_0. This has profound impact on laser performance as low T_0 values will increase threshold current values near room temperature, resulting in increased carrier concentration and thus higher free-carrier absorption (FCA) and Auger losses as well.

An alternate approach to is to grow a metamorphic buffer layer to increase the substrate lattice constant and reduce the amount of As required to manage the strain in the quantum well [56]. The metamorphic approach has had success at small changes in lattice constant, however extension of this method to long wavelength operation will face challenges associated with threading dislocations formed during buffer relaxation. A lattice matched approach would benefit from the low defect density substrate and the superior thermal properties of lattice matched materials. One such approach to extension of the emission wavelength is the so-called dilute-nitride materials, which have been successfully used in GaAs-based lasers to extend the emission wavelength to $>1.55\,\mu$m [57]. However, progress has been extremely limited on the GaSb material system [58].

Adding small amounts of nitrogen to conventional III-V materials results in a reduction of both the bandgap and the lattice constant due to the conduction band anticrossing the nitrogen level [59]. The nitrogen reduces the bandgap by only affecting the conduction band. This allows for independent control over the bandgap and band discontinuities of the quantum well. Additionally, the reduction in bandgap has little affect on the split-off band which should be favorable for characteristic temperature. This makes dilute-nitride

active regions, a particularly promising approach to extension of the emission wavelength of type-I diode lasers.

Advances in GaSb-based dilute-nitride active regions for mid-IR diode lasers are discussed in Chapter 2. In particular, an optimal growth space is proposed in which substitutional nitrogen incorporation is optimized. This growth regime enables room-temperature photoluminescence emission to be observed from GaInNSb quantum wells on GaSb for the first time.

Simply reducing the bandgap of the quantum well will not necessarily lead to improved long-wavelength laser performance. As the wavelength increases, several parasitic processes increase: the optical mode broadens, resulting in increased overlap with the cladding; the optical loss per carrier increases $\sim\lambda^2$; the electron mass is reduced, increasing Auger recombination and decreasing differential gain. Even at sub-3 μm wavelengths, issues with cladding loss have required mid-IR lasers to trade between electrical conductivity of the p-type cladding and optical loss associated with intervalence-band absorption of the free-holes [60–63]. An alternate approach to will likely be required to increase the emission wavelength to cover the technologically important $3-5\,\mu$m range. An attractive approach would be to remove the p-type cladding.

In edge emitting lasers, replacing the p-type cladding with an n-type cladding and a tunnel junction, similar to the approach for VCSELs, may not result in the same performance enhancement, due to a lack of a vertical standing wave at which to place the tunnel junction. Instead, using a

tunnel junction would replace a thick, lightly-doped layer with a thin, heavily-doped one. Also, the tunnel junction would be placed closer to the core of the waveguide where optical field strength is greater. GaSb tunnel junctions, employing ErSb nanoparticles offer the potential to break the trade-off between the optical loss and electrical conductivity of the p-type cladding. Because the Schottky barrier for holes is very small ($\sim$200 meV), a highly assymetric doping profile can be utilized to minimize the number of holes in the laser cladding. Such tunnel junctions are discussed in detail in Chapter 3.

1.3 RE-V Plasmonics

In addition to enhancing optical devices with tunnel junctions, the RE-V materials are promising for epitaxially integrated active plasmonic structures. Metallic structures, with feature sizes that are small compared to the wavelength of optical radiation, have become extremely useful for photonic devices [64]. Surface plasmons have been exploited for molecular sensing [65], light focusing [66], near-field optical microscopy [67], and enhanced near-field semiconductor absorption [68]. The integration of metallic nanoparticles (e.g. silver, gold, copper, etc.) is currently limited to ex situ deposition about the device periphery, as most metal systems cannot be epitaxially integrated into semiconductors [13]. As such, desirable plasmonic structures, such as a semiconductor emitter surrounded by metallic films, are prohibitively complicated to achieve with conventional fabrication methods [69]. Rare-earth pnictide materials offer a potential platform to investigate plasmonic structures in an

epitaxially compatible material system. The fundamental plasmonic properties of the RE-V materials remain largely unexplored.

Nanostructures of RE-V materials embedded in III-V semiconductors exhibit absorption properties in the infrared that have been attributed to surface plasmon resonance [70–72], or band-to-band transitions shifted due to quantum confinement [71]. Figure 1.10 show polarization dependent loss measurements for superlattices of ErSb nanoparticles embedded in GaSb from [72]. Important features of the nanoparticle morphology, namely the elongation of ErSb nanoparticles along the $[0\,\bar{1}\,1]$, manifest in the absorption measurements. As deposition is increased, the particles increase in size and elongate along the fast diffusion direction. The results in a red shift of the peak in the absorption consistent with surface plasmon resonance.

In Chapter 5, we investigate the ErAs/GaAs heterostructures as a potential prototype material system for all-epitaxial plasmon-enhanced devices. In particular, we attempt to enhance spontaneous emission by spectrally aligning the peak wavelength of the ErAs absorption to the emission from a quantum well active region. Bulk optical properties are used to extract the plasmonic properties of ErAs films.

1.4 Epitaxially Embedded RE-V Films

The ErAs films have seen renewed attention lately for terahertz Schottky contact detectors [41, 73], and Ohmic contacts to GaInAs [74]. Both applications benefit from the very high quality III-V/RE-V interface and min-

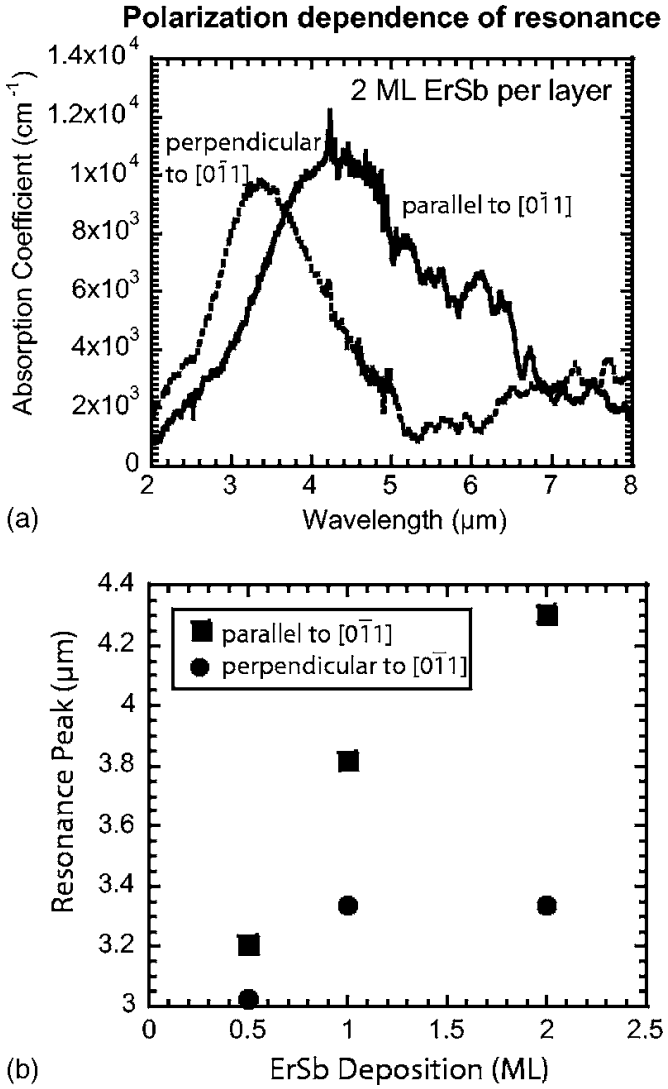

Figure 1.10: (a) Polarization dependent absorption spectra for 2 ML ErSb superlattice. (b) Wavelength of the absorption peak for orthoganol polarizations as a function of nanoparticle deposition. From [72]

imal reaction depth. However, in both devices, the ErAs films are located at the device surface, limiting integration to a single metal layer. Electrical devices, such as a metal base transistor, as well as plasmonic devices, could benefit from moving the metal/semiconductor heterostructure into the core of the device.

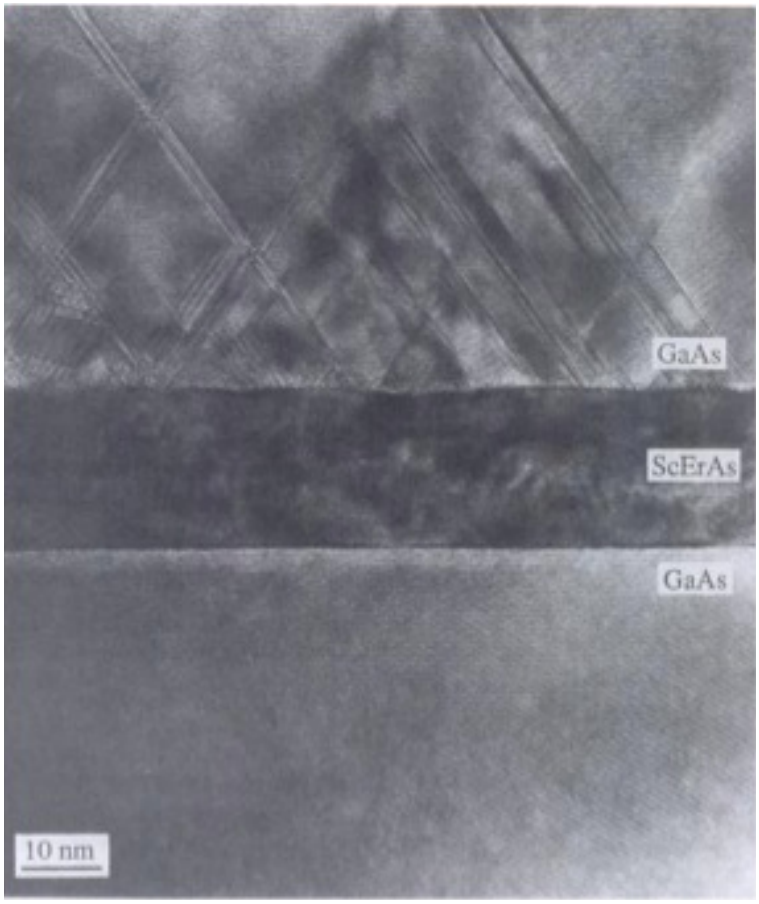

Figure 1.11: Epitaxially embedded ScErAs film, lattice matched to GaAs. The GaAs overgrowth exhibits planar defects. From [20]

Conventional layer-by-layer approach to III-V/RE-V/III-V heterostructures results in highly defective overgrowth of the RE-V films, shown in Fig. 1.11, due to symmetry related defects. Chapter 2 discusses the overgrowth of ErAs nanostructures, which is accomplished by lateral overgrowth the ErAs nanoparticles with overgrowth seeded by the exposed GaAs. Chapter 4 demonstrates the ability to grow high-optical-quality III-V layers by depleting the surface of erbium utilizing subsurface ErAs nanostructures to scavenge the surface erbium. Chapter 6 discusses the potential to exploit these phenomena to grow full films of ErAs through a thin layer of GaAs that preserves the substrate symmetry [75]. This nanoparticle-seeded film growth method provides a path towards epitaxially integrated active plasmonics on the GaAs platform.

1.5 Organization of Dissertation

This dissertation focusses on the integration of rare-earth pnictide materials into optical devices. Subsequent chapters detail several experiments critical to identifying parasitic erbium incorporation, determining the incorporation mechanism of erbium in III-V semiconductors in both the dilute and nanoparticle regime, and overcoming challenges required to incorporate RE-V/III-V heterostructures to enhance optical devices. In particular, Chapter 2 discusses the molecular beam epitaxy growth technique with a detailed discussion of erbium incorporation into GaAs. These incorporation dynamics are fundamental to both achieving high optical quality overgrowth of RE-V nanostructures and embedding full films of ErAs in GaAs. Chapter 3 discusses the

use of RE-V nanoparticles at $p-n$ junction interfaces to create tunnel junctions that simultaneously display low optical and electrical losses. Chapter 4 provides a detailed investigation into the optical quality of III-V layers grown with ErAs nanostructures. The fundamental chalenge of parasitic erbium incorporation and surface segregation is overcome by utilizing preferential incorporation at subsurface ErAs nanoparticles. Chapter 6 extends the concept to embed full films of ErAs with the nanoparticle-seeded film growth technique. This growth method overcomes the mismatch in rotational symmetry in the material system. Finally, in Chapter 7 conclusions based on the preceding chapters are presented, along with potential future research directions.

Chapter 2

Molecular Beam Epitaxy

This chapter provides a description of the molecular beam epitaxy (MBE) growth method used in this work. Subsequent sections describe the specific challenges associated with (i) growth of mixed group-V compound (III-V) semiconductor alloys, (ii) incorporation of nitrogen into GaSb based materials, and (iii) incorporation of rare-earth monopnictide (RE-V) nanostructures in GaAs and GaSb host materials.

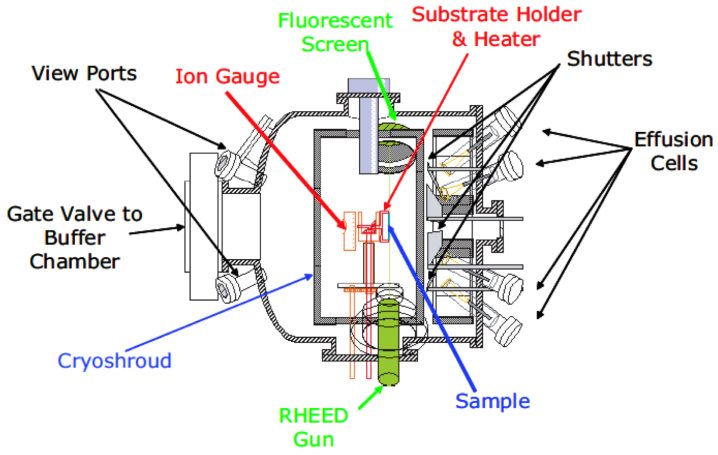

Figure 2.1: Schematic of a molecular beam epitaxy chamber. Adapted from [76].

2.1 Conventional III-V MBE

Molecular beam epitaxy is an ultra-high vacuum crystal growth technique. It consists of ultra-pure (typically $> 99.99995\%$) atomic or molecular sources which are heated in effusion cells to produce a flux, the so-called molecular beam. The molecular beam is then either allowed to persist to the substrate or blocked by a mechanical shutter. Because of the ultra-high vacuum environment, the mean free path of the molecules is much larger than the dimensions of the chamber. As such, there is minimal interaction between molecular beams of the different sources.[1] Normal operation of III-V MBE is to use excess group-V flux and control the growth rate with the group-III fluxes, which have sticking coefficients near unity. As such, the group-III alloy composition can easily be varied by changing the group-III flux ratios. The surface mobility of the adatoms is controlled predominantly by the substrate temperature and the group-V overpressure. The decoupling of the growth rate and surface diffusion is particularly important in the growth of materials that are not thermodynamically favored, as the metastable alloys can be pseudomorphically stabilized as the growth front moves. Interested readers are directed to one or more of the several good references that give more complete treatments of the growth method [77–80].

[1] Note while this is true to first, or even second order, the parasitic incorporation of erbium around the shutter causes severe degradation in the optical quality of layers grown with the erbium cell hot. This subject is treated in detail in Chapter 4

2.2 Mixed Group-V Alloys

Things get more complicated when the group-V elements need to be alloyed. Unlike the group-III adatoms, which have unity sticking coefficients under normal growth conditions, the group-V fluxes are in excess, resulting in less than unity sticking coefficients. As such, group-V species must compete for anion vacancies. Additionally an As for Sb exchange reaction [81] near the surface makes incorporation sensitive to group-V flux, substrate temperature, and growth rate [82–86].

For thick layers where lattice matching is of paramount importance, such as the cladding layers in a separate-confinement-heterostructure lasers, precise control over the alloy composition is required. Several methods to control the composition have been employed; however, there has yet to be a comparison of the methods for optical quality of the resulting films by measuring a meaningful parameter such as laser threshold. Things are additionally complicated by the reported optimal growth temperatures for GaInAsSb QW lasers which range from 350°C to 475°C [87, 88].

To control the alloy composition for the lasers we use a method that is similar to [89, 90]. We hold the Sb/III BEP ratio constant at 2.2x for the laser core and 2.5x for the cladding layers. The group-III fluxes are chosen so barrier and quantum well alloys could be grown with the same fluxes. This prevents a growth interruption at the barrier/QW interface. We focussed on low growth temperature to mitigate the As for Sb exchange reaction and to make the laser compatible with future incorporation of nitrogen into the quantum well. With

this method we found PL emission intensity to have only a weak dependance on substrate temperature and As overpressure.

The photoluminescence and alloy composition calibration sample structures are shown in Fig. 2.2. The optical quality of the laser core structures show little dependence on growth temperature or Sb-overpressure over the growth region that we investigated. Figure 2.3 shows the PL spectra for samples grown at varying growth temperatures. Similar to previous reports, there appears to be an optimal growth temperature for the parameters used in our investigation, however, the dependence on temperature is very weak allowing for investigation of dilute-nitrides at low growth temperatures. Figure 2.4 shows the PL spectra for laser core samples grown at a substrate temperature 420°C with varying Sb-over-pressures.

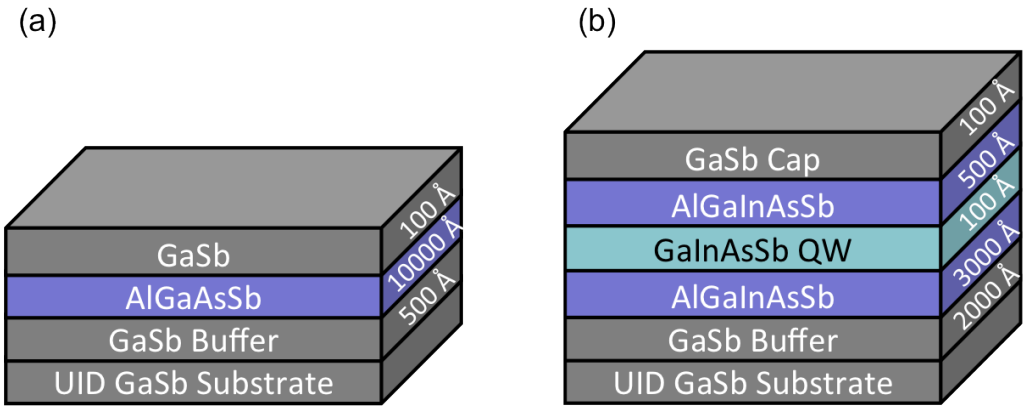

Figure 2.2: (a) Cladding alloy calibration sample structure. (b) Laser core calibration sample. Measurements of PL and XRD give alloy composition and emission strength.

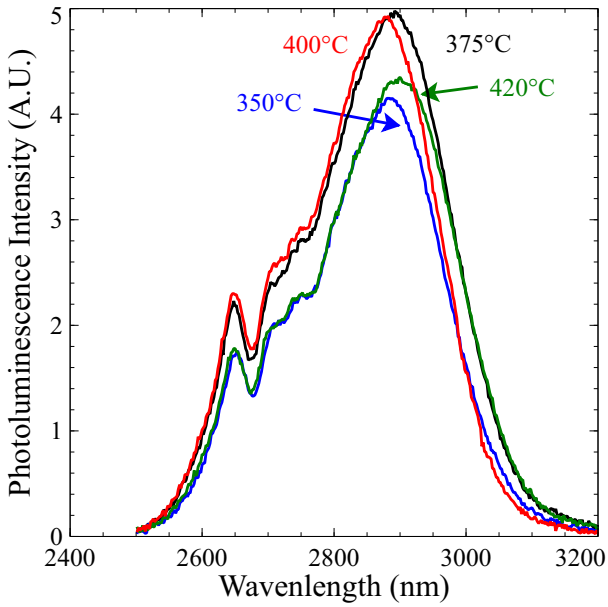

Figure 2.3: Photoluminescence spectra for laser core structures grown with varying substrate temperature.

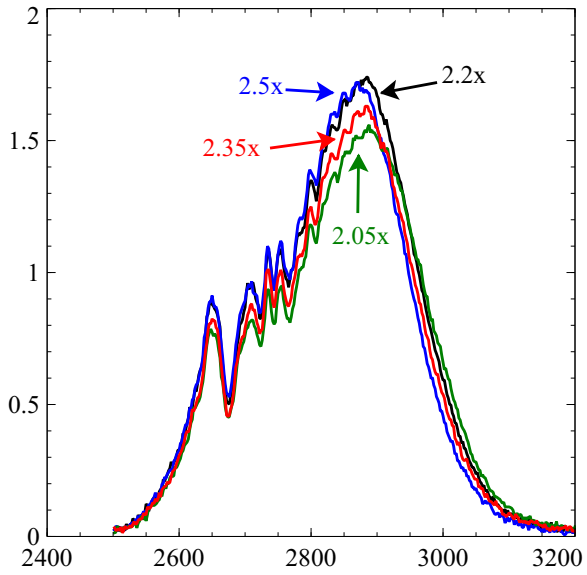

Figure 2.4: Photoluminescence spectra for laser core structures grown with varying antimony overpressure.

Things like surface residence time and surface diffusion length can change alloy composition and vary with temperature and total group-V flux differently for different group-V adatoms. Additionally, differences in bond-strength can result in an exchange reaction which is particularly problematic in the mixed As/Sb structures grown for our mid-IR lasers. Figure 2.5 plots the As mol fraction, measured with XRD, as a function of growth temperature and As flux. Because the incorporation is a strong function of temperature over the entire growth space investigated, precise control of the substrate temperature is of paramount importance.

2.3 Surface Segregation Model

When growing alloys consisting of elements or materials with mismatched enthalpies of formation (bond strengths), there is a tendency for an exchange reaction near the surface. Early investigation into the surface segregation phenomenon was focused on explaining anamolous doping profiles for Sn-doped GaAs [91, 92]. Surface segregation has also been observed for oxygen [93], manganese [94], erbium [26, 28, 46, 95], indium [96], bismuth [97]. as well as other metals and dopants [98]. Figure 2.6 illustrates the incorporation into the epitaxial layer, where incorporation occurs from a surface layer rather than directly from the impinging vapor.

A simple mass balance model can then be developed for the incorporating atom.

$$\frac{dn_s}{dt} = F - (k_{ev} + k_{in})n_s \tag{2.1}$$

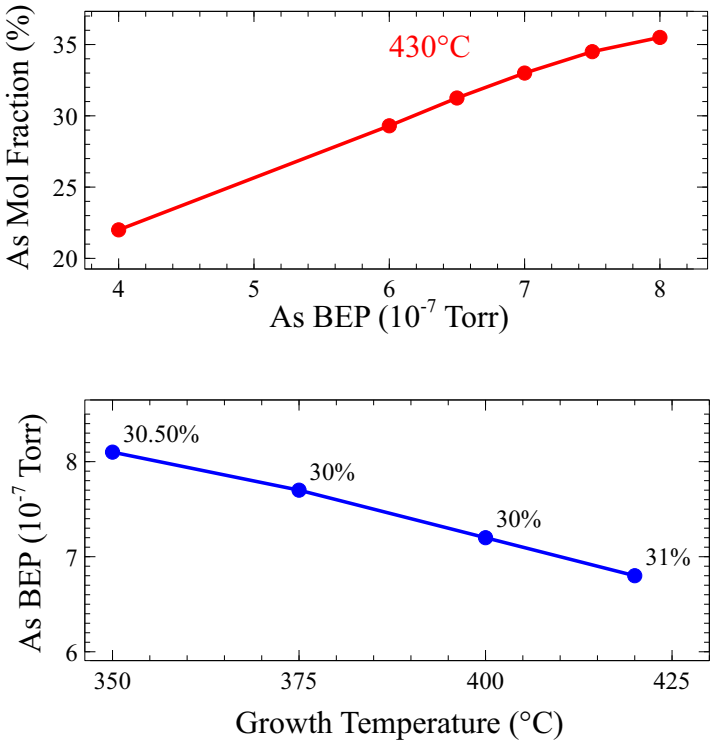

Figure 2.5: (Top) As incorporation into $Al_{.23}Ga_{.42}In_{.35}As_xSb_{1-x}$ with varying As beam equivalent pressure (BEP). The Sb BEP was fixed at 2.2 times the effective Ga BEP, corresponding to just above stoichiometry. (Bottom) As BEP required for nominally identical As mol fractions for $Al_{.23}Ga_{.42}In_{.35}As_xSb_{1-x}$ grown at varying substrate temperature.

where n_s is the surface concentration, F is the impinging flux, k_{ev} is the rate constant for evaporation from the surface, and k_{in} is the rate constant for incorporation to the epilayer.

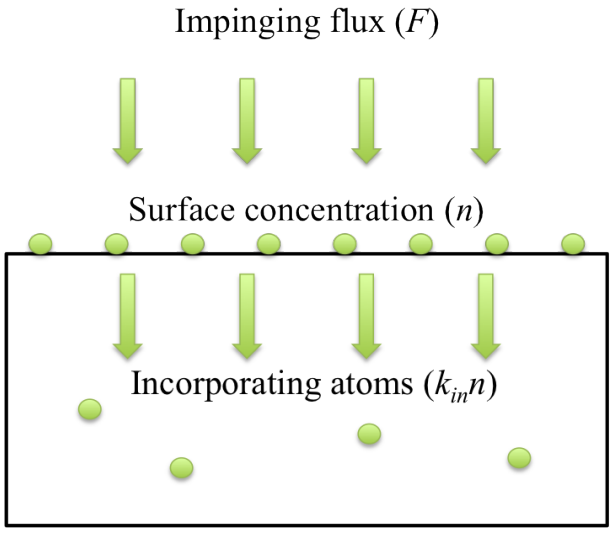

Figure 2.6: Illustration of the incorporation of adatoms from a surface segregation layer.

In the case of the incorporation of erbium and nitrogen, the evaporation of the surface segregation layer is small compared to the incorporation into the epi-layer, $k_{ev} \ll k_{in}$, resulting in the steady-state condition,

$$n_s = \frac{F}{k_{in}}. \tag{2.2}$$

where k_{in} is dependent on the growth conditions. Because the surface segregation is thermodynamically favored, the rate constant decreases with growth temperature and increases with growth rate. Therefore, the highest surface

concentrations are obtained for low growth rate, high temperature growth regimes.

Perhaps more interesting is the incorporation dynamics in the case when there is an abrupt change in either the impinging flux, F, or the surface segregation constant, k_{in}. One well studied case of such an interface is the oxygen incorporation at an AlAs/GaAs interface. Under a constant background oxygen flux, the incorporation of oxygen will have spikes in the oxygen concentration at the interfaces where the Al concentration is decreasing in the growth direction. The origin of the peaks is the decrease in the surface segregation coefficient in the material with lower Al content, due to the stronger Al-O bond. As such, the surface oxygen layer cannot segregate to the from the AlAs to the GaAs surface [99]. Transient effects, namely reduced surface concentration after an ErAs nanoparticle layer, will be required to understand the optical quality experiments on ErAs overgrowth in Chapter 4. Namely, we propose a reduction of the surface erbium layer concentration, and thus the parasitic incorporation of erbium, after the growth of an ErAs nanoparticle layer as the mechanism for reduced Er-doping near the ErAs nanoparticles. The implications for optical quality will be discussed in detail in Chapter 4.

2.4 Dilute Nitrides

Growth of dilute-nitride GaAs-based materials has been described in excruciating detail in other work [100]. Here we focus on incorporation into GaSb, in particular the growth conditions which result in optically active

dilute-nitride layers. The nitrogen incorporation will be discussed in terms of a surface segregation analysis; however, surface heating from the plasma cell may play an important role in the incorporation dynamics.

In the GaAs material system, high quality materials are generally grown at low substrate temperatures [57], or very fast III-V growth rates [101]. These growth conditions have been termed "the kinetic advantage" because the surface is far away from thermodynamic equilibrium, where nitrogen incorporation is not favored. Additionally, the nitrogen incorporation in this regime is a weak function of surface temperature, earning the growth regime the title "unity sticking coefficient regime". We notice that these growth conditions also result in the lowest nitrogen surface concentration if the nitrogen is incorporating into the epitaxial layer from a surface layer. In GaAs-based dilute-nitrides, the favorable plasma conditions are just enough power to remain in the inductively coupled plasma region [102, 103], and a DC electric field applied across the plasma cell aperture was used to deflect energetic ions away from the substrate. However, similar growth conditions in GaSb-based materials have not resulted in room temperature photoluminescence from dilute-nitride samples [104].

Additionally, samples that do not display photoluminescence tend to also show a higher nitrogen concentration when measured using SIMS rather than using XRD. This is consistent with the nitrogen split-interstitial (which is known to be a non-radiative recombination center [105, 106]) as the cause of the degraded optical quality, but does not reduce the lattice constant as

substitutional nitrogen does.

Therefore, the hypothesis that surface concentration of a segregating nitrogen surface layer governs the type of incorporation into the epitaxial layer, such that, substitutional nitrogen incorporate for low surface concentrations, and increasing amounts of split interstitials incorporate with increasing surface concentration. To test this hypothesis, a series of samples were grown with varying substrate temperature and growth rate. The sample structure consisted of a 200 nm GaSb buffer, a 100 nm GaNSb layer, and a 20 nm GaSb cap. The plasma cell was maintained at 300W forward power with a nitrogen flow of 0.3 sccm. Figure 2.7 shows an illustration of the proposed growth space (top) and experimental measurements of the nitrogen incorporation for XRD measurements under varying growth conditions.

An alternate approach to determining nitrogen concentration is to use nuclear reaction analysis Rutherford back-scattering (NRA-RBS). By looking at the nitrogen yield in both random orientation and channeling along a crystalline axis, one can distinguish between interstitial and substitutional nitrogen. When aligned to a crystalline axis, the substitutional nitrogen is screened by the antimony sublattice; however, in random orientation, both the substitutional and interstitial nitrogen contribute to NRA-RBS signal. Results from NRA-RBS for the same samples plotted in Fig. 2.7 with the slower growth rate, 0.66 μm/hr, are plotted in Fig. 2.8. The nitrogen incorporated on substitutional sites follows a similar trend for the XRD and NRA-RBS measurements; however, NRA-RBS reveals the total nitrogen incorporation in

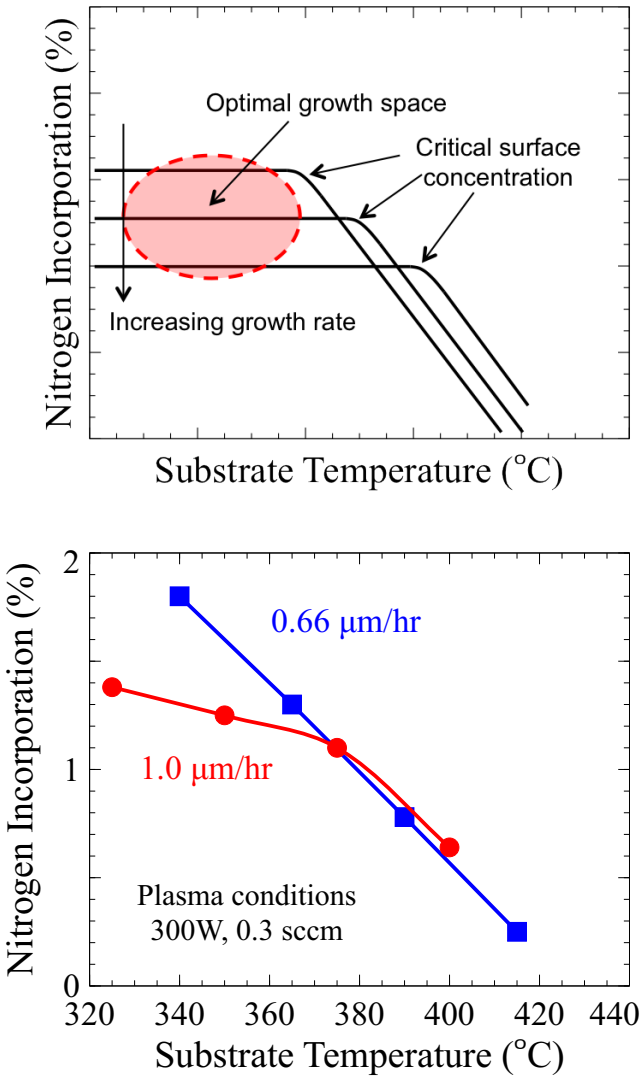

Figure 2.7: (top) Illustration of nitrogen incorporation model where a critical surface concentration for the formation of split interstitials exhists. (bottom) Nitrogen incorporation, measured by XRD, for samples grown at varying growth temperature with low (0.66 μm/hr) and high (1.0 μm/hr) growth rates. Adapted from [104]

the sample to be constant.

These results can be understood in terms of a surface segregation model: the flux of nitrogen that is going to incorporate is set by the plasma conditions, such that no "active" nitrogen is lost from the surface; the nitrogen will segregate to the growth surface building up a surface concentration until the incorporation into the epitaxial layer equals the flux from the nitrogen cell; the surface concentration required for the same incorporation is lower at lower growth temperatures.

This model suggests a potential path to achieve optically active dilute-nitride layers in GaSb would be to use a reactive surfactant (similar to Sb on GaAs materials [57, 107]) to suppress segregation of nitrogen to the surface. Unfortunately, our machine does not have Bi, the analogous material on the GaSb platform. Fortunately, an alternate approach is to use the transient at the initiation of the nitrogen flux to incorporate nitrogen at less than the steady-state concentration level. This results in a broadening of the nitrogen concentration profile but suppresses the formation of split interstitials. To test this growth method, quantum wells of GaInNSb in GaSb with a single nitrogen pulse during the quantum well. A similar sample was grown with a GaInAsSb/AlGaInAsSb QW for long-wavelength emission. The photoluminescence spectra for the samples are shown in Fig. 2.9. This represents the first demonstration of room-temperature photoluminescence from dilute-nitride materials on GaSb. This is promising for extension of the emission wavelength of type-I diode lasers in the $3-4\,\mu$m region. Look for lasers based

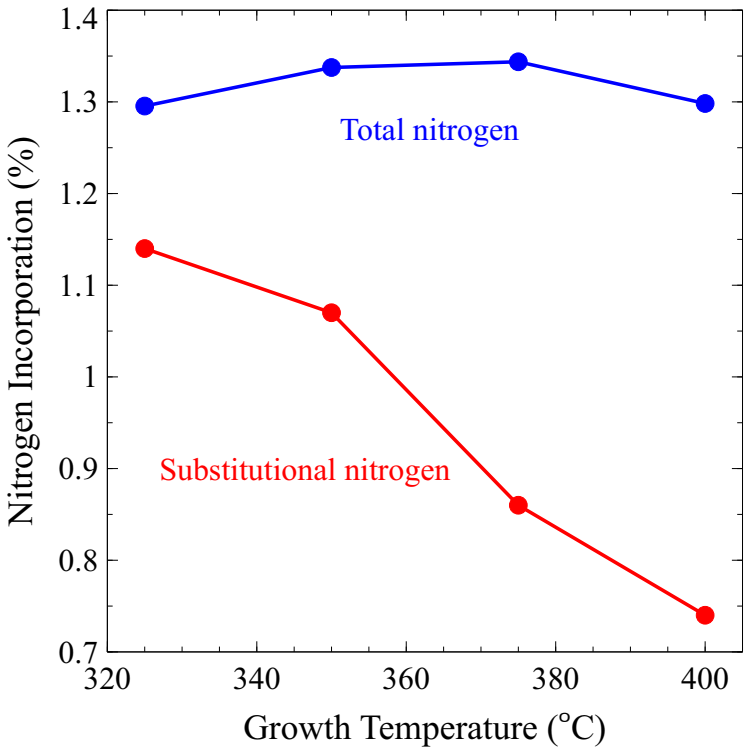

Figure 2.8: Nuclear reaction analysis Rutherford back-scattering (NRA-RBS) results for nitrogen incorporation of GaNSb samples grown at 0.66 μm/hr. The total nitrogen is obtained from random axis yield while the substitutional nitrogen is obtained from the difference between random axis and channeling yields when aligned to $< 100 >$, $< 110 >$, and $< 111 >$ directions. Adapted from [104]

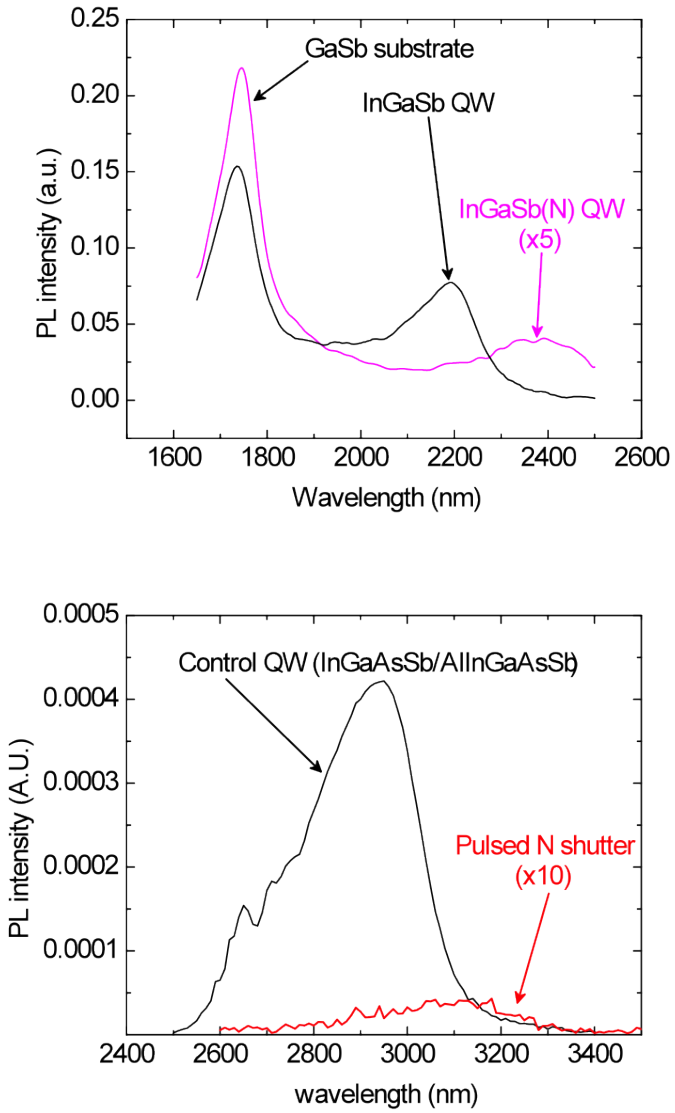

Figure 2.9: Photoluminescence spectra for GaInSb quantum well grown with and without a nitrogen pulse during the QW. Adapted from [104]

on this and surfactant-mediated dilute-nitrides to appear in Hari Nair's papers and dissertation when system Bravo maintenance is complete.

2.5 Erbium Incorporation in GaAs

Various applications have motivated research groups to examine erbium incorporation into GaAs under differing growth conditions. The two primary approaches to embedding ErAs structures in III-V materials include precipitation of ErAs nanoparticles out of heavily erbium-doped layers [22, 25–27, 108] and the intentional deposition of ErAs nanoparticles at a III-V surface [29]. Observations from Er-doped GaAs provides a foundation for the incorporation model for erbium into GaAs. Layers grown with low erbium concentration result in substitutional incorporation, i.e. erbium on a gallium site [108]. With higher erbium concentrations, the erbium incorporates in interstitial sites which were identified by transmission electron microscope imaging to be rocksalt ErAs precipitates [22]. The arsenic sublattice is coherent across the ErAs/GaAs interface, suggesting that erbium displaces gallium during ErAs nanoparticle formation [30]. Even for layers doped heavily enough for ErAs precipitates to form, a gap between the initiation of the erbium-doped layer and the appearance of the first ErAs precipitates is observed [24]. These observations suggest that erbium segregates to the surface and the substitutional incorporation corresponds to the kinetic incorporation at the moving growth front (illustrated in Fig. 2.6). The ErAs rocksalt nanoparticles represent a different incorporation mechanism that is only present at sufficiently high surface erbium concentration. The gap between the initiation of the heavily Er-doped layer and the first ErAs precipitates can be understood as the time that it takes for the surface erbium concentration to build up to the critical density

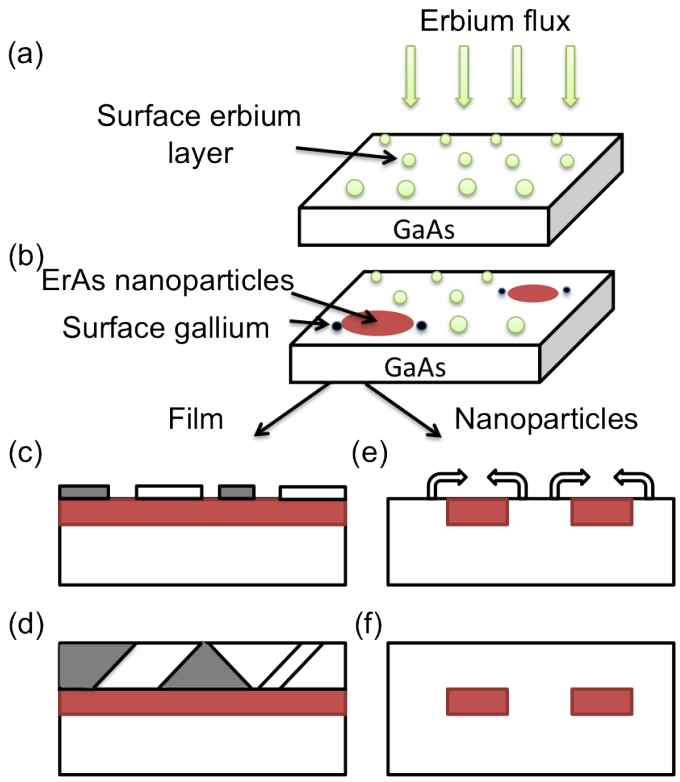

Figure 2.10: Illustration of conventional ErAs/GaAs heterostructure growth. (a) Erbium initially accumulates at the surface. (b) When the critical surface areal density for ErAs nanoparticle formation is reached, ErAs nanoparticels form. The particles seed as ∼4 ML particles on each side and expand laterally until a full film is formed. (c) GaAs overgrowth of ErAs films results in two distinct island orientations due to the mismatch in rotational symmetry. (d) The GaAs overgrowth is highly defective due to inversion domain boundaries and micro-twins where the islands meet. (e) If the ErAs deposition is limited to self-assembled nanoparticles and the GaAs overgrowth is seeded by the exposed GaAs. (f) The ErAs nanostructures can be embedded in single phase GaAs.

for nanoparticle formation. This particle formation is consistent with the embedded growth mode observed for nanoparticle growth on a static surface [30]. Cross sectional TEM image of ErAs grown at an interface between GaAs and AlAs, shown in Fig. 2.11, provides direct evidence of the embedding of the ErAs nanoparticles.

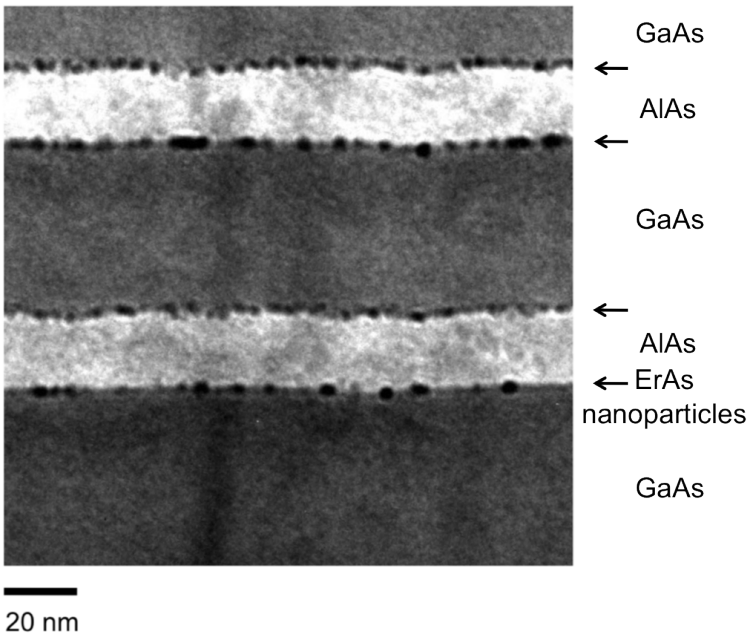

Figure 2.11: Cross-sectional TEM image of an ErAs nanoparticle layer embedded in a GaAs surface and overgrown with AlAs. The embedding of the ErAs nanoparticle layer is apparent from the ErAs nanoparticles (dark spots) below the AlAs/GaAs interface. Image courtesy of Demitri Klenov

Once ErAs precipitates are present at the growth surface, the surface erbium preferentially incorporates into the ErAs nanoparticles. This is evident for Er-doped GaAs layers grown under varying growth conditions, where the

ErAs particle size depends on the surface mobility of the erbium adatoms. The largest particles, and even extended structures such as wires or trees, are realized for the highest surface mobilities [24] . To date, applications have required investigation into a single growth regime. Investigation of the optical quality of the overgrowth of ErAs nanostructures illucidates the two distinct incorporation regimes. Attempts to integrate ErAs nanostructures within optical devices [46] have required reduction in parasitic erbium incorporation (previously observed by Jourdan [28] et al.). It was shown that the key parameter to achieve high optical quality III-V material above the ErAs layers is the amount of GaAs overgrowth between the ErAs nanoparticle layer and the surface while cooling the erbium cell [46].

Simply embedding high quality nanoparticles into III-V materials is only half of the problem. Devices such as fast photoconductors for THz generation require multiple nanoparticle layers to be incorporated with little separation and high quality III-V material between. Such structures have been reported in the ErAs/GaAs material system [39]. Investigation of the thermal stability of such structures reveals interesting details about the ErAs interface. If the superlattice spacing is sufficiently small, anomalous features start to appear in XRD, suggesting degradation of the superlattice structure. Because lateral conductivity in the III-V semiconductor between ErAs nanoparticle layers is a critical parameter for devices such as heterodyne photomixers, the structural quality of such superlattice is of paramount importance. Figure 2.12 and 2.13 show XRD scans for ErAs superlattices consisting of 1.2 ML ErAs

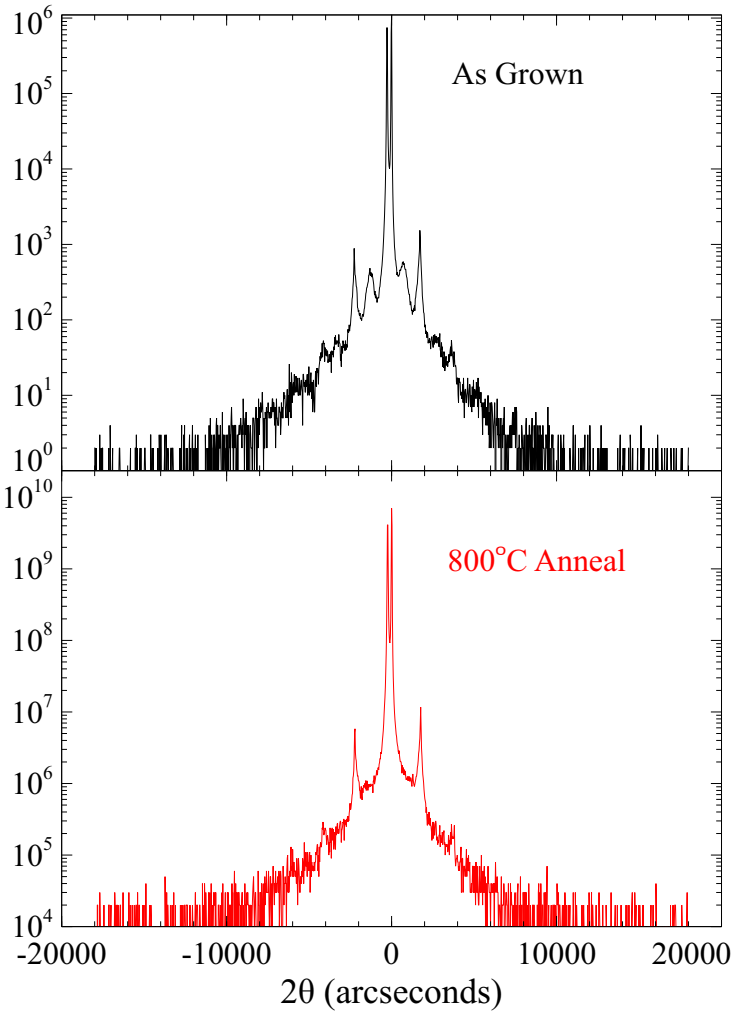

Figure 2.12: High-resolution X-ray diffraction of superlattice consisting of 60 periods of (1.2 ML Eras / 20 nm GaAs). As grown, the sample shows anomalous peaks that are suppressed with thermal annealing at 800°C under AsH_3 overpressure.

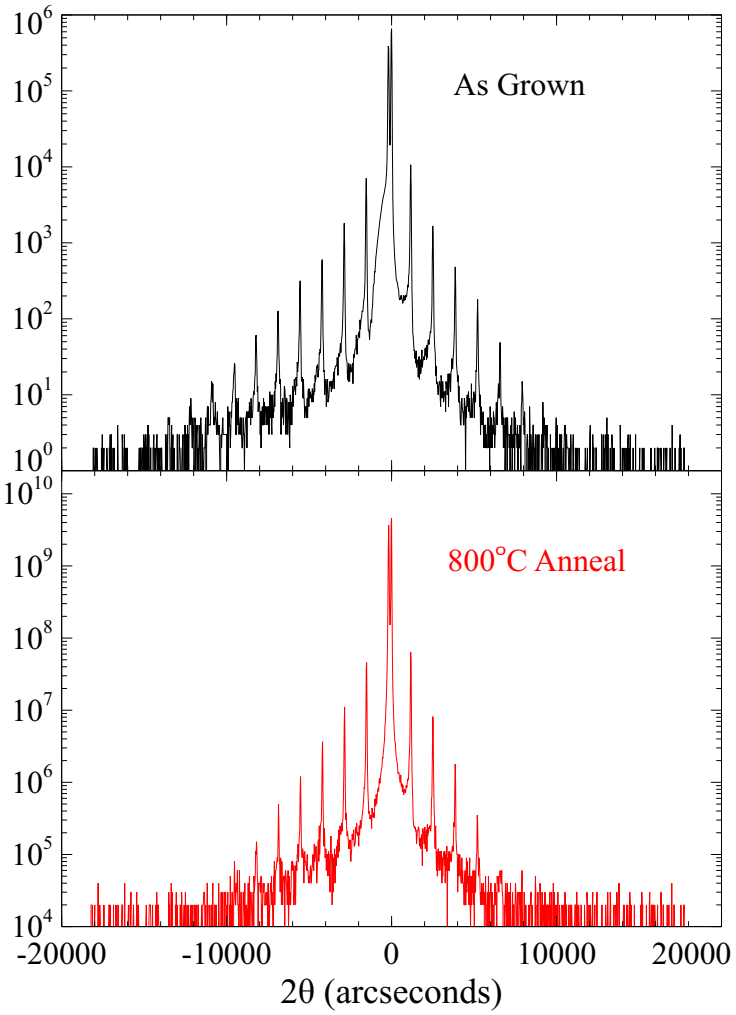

Figure 2.13: High-resolution X-ray diffraction of superlattice consisting of 40 periods of (1.2 ML ErAs / 30 nm GaAs). As grown, the sample shows a shoulder on the substrate/zero-order superlattice peak that is suppressed with thermal annealing at 800°C under AsH_3 overpressure.

deposition per period and periods of 20 and 30 nm respectively. Both of the samples show degradation in the structural quality for the as-grown samples that is suppressed with thermal annealing to 800°C in an AsH_3 atmosphere in an ambient pressure MOCVD.

This improvement in the structural quality of ErAs containing materials speaks to the thermal stability of the ErAs/GaAs interface. This is particularly promising for incorporation of ErAs nanostructures into devices requiring post-growth thermal annealing such as those with dilute-nitride active regions.

Chapter 3

Low-Loss Tunnel Junctions

Semiconductor opto-electronic devices employ tunnel junctions for low-loss interconnections between majority carrier regions of different polarity. A classic example is the use of tunnel junctions between serially connected junctions in high-efficiency multijunction solar cells [109]. Additionally, some optical devices require both electrons and holes, but have significantly higher losses associated with one of the carriers. Examples of this are electrical losses in the p-type AlAs/GaAs distributed Bragg reflector [110] for vertical-cavity surface emitting lasers (VCSELs) and free carrier absorption losses in the p-type cladding of mid infrared diode lasers [63, 111–113]. In all of these opto-electronic devices, the tunnel junction requirements are similar. Namely, the tunnel junctions should have simultaneously high electrical-conductivity and low optical-loss.

3.1 Conventional Tunnel Junctions

In 1958, Leo Esaki observed anomalous conductivity at low bias in heavily-doped germanium $p-n$ junctions [114]. The current was due to quantum mechanical tunneling between the conduction and valence bands in the

high-field region of the diode (illustrated in Fig. 3.1). This phenomenon is the basis for conventional tunnel junctions (also known as Esaki diodes). For the incorporation into optical devices, both the electrical and optical losses of the tunnel junction are of paramount importance. Here, design criteria for high-conductivity tunnel junctions, and the implications for optical loss, are established using a simple model to calculate tunneling probability. Several good reference treat band-to-band tunneling in semiconductors (for example [115]). For the sake of clarity, several simplifying approximations will be used. Namely, we calculate the band-to-band tunneling probability by assuming a nearly free electron with conduction band effective mass tunnels through a triangular barrier with height (Φ_B), and width L. The WKB tunneling model can then be applied to capture the important device parameters and make qualitative predictions of tunneling enhancement for varying devices. In this case the tunneling probability (T) is given by:

$$T = \exp\left[\frac{-4\sqrt{2qm^*}}{3\hbar}\Phi_B^{1/2}L\right], \tag{3.1}$$

where m^* is the electron effective mass, q is the elemental electron charge, and $\hbar$ is the reduced Plank's constant. For a highly doped semiconductor with Fermi-level at the band edges, we replace Φ_B with the bandgap of the semiconductor E_g and the barrier width L with the depletion width of a $p-n$ junction (W_d), which is calculated, assuming abrupt doping profiles and using the depletion approximation, to be:

$$W_d = \sqrt{\frac{2\epsilon_r\epsilon_0}{q}\left(\frac{N_A+N_D}{N_AN_D}\right)E_g}\,. \tag{3.2}$$

where N_A and N_D are the acceptor and donor concentration is the tunnel junction. The tunneling probability can be expressed in terms of semiconductor parameters:

$$T = \exp\left[\frac{-8\sqrt{m^*\epsilon}}{3\hbar}\left(\frac{N_A + N_D}{N_A N_D}\right)^{\frac{1}{2}} E_g\right] . \tag{3.3}$$

Therefore, a small bandgap semiconductor with maximum achievable doping levels, N_A and N_D, are required to maximize the conductivity of a conventional tunnel junctions.

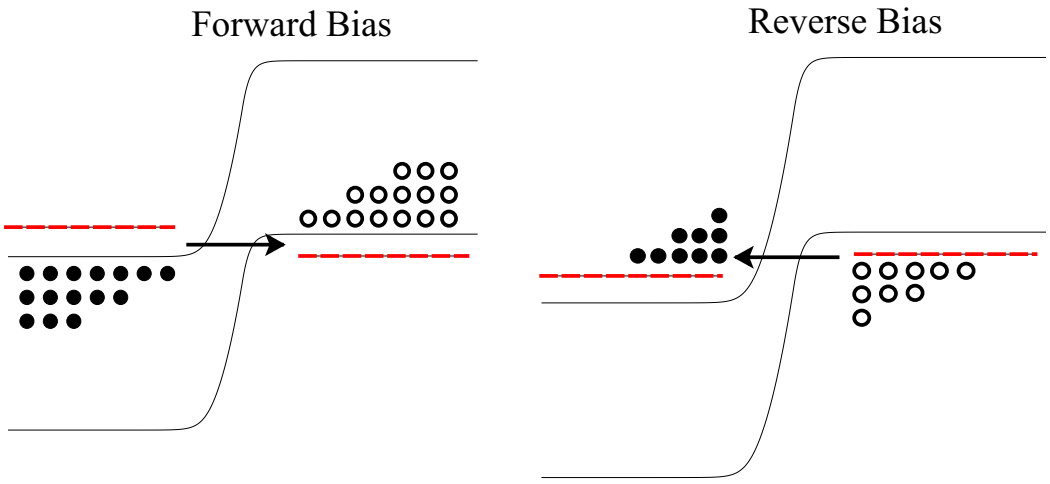

Figure 3.1: Illustration of conventional tunnel junction operation under forward and reverse biases. The solid circles represent electrons and the circle outlines represent holes. Only the majority carrier profiles are represented. The arrow shows the tunneling direction for electrons.

3.2 Advanced Semiconductor Tunnel Junctions

Obviously, optical losses associated with a small bandgap, or heavily doped layers prohibit incorporation into certain devices, particularly solar cells and long-wavelength lasers. As such, several approaches to improve tunneling performance have been investigated. The two primary approaches to enhance tunnel junction conductivity are to use heterojunction discontinuities that reduce the tunneling barrier. This approach is illustrated in Fig. 3.2 for type-II band alignments[1]. As the heterojunction discontinuities are increased, type-III band alignments[2] (e.g. InAs/GaSb) can result. Tunnel junction based on type-III heterostructures display very low resistivity, comparable to Ohmic contacts [116]. Type-III heterostructure tunnel junctions have been incorporated into laser devices in VCSELs [117] and to interconnect stages in interband cascade lasers (ICLs) [118]. However, high-conductivity type-III tunnel junctions are still heavily doped, and mismatching the doping concentration reduces the conductivity [116]. Even nominally undoped TJs used in ICLs have high free-carrier concentration from "self-doping" of the confined layers [118]. Additionally, the optical confinement is problematic for incorporation at the cladding/core interface of diode lasers.

The reduced tunneling barrier for heterostructure $p-n$ junctions utilizing favorable band-discontinuities alloys for increased electrical conductivity

[1] A type-II band alignment has one band-edge of each material lie within the bandgap of the other

[2] Type-III band alignment has the conduction band of the n-type material overlap the valence band of the p-type material.

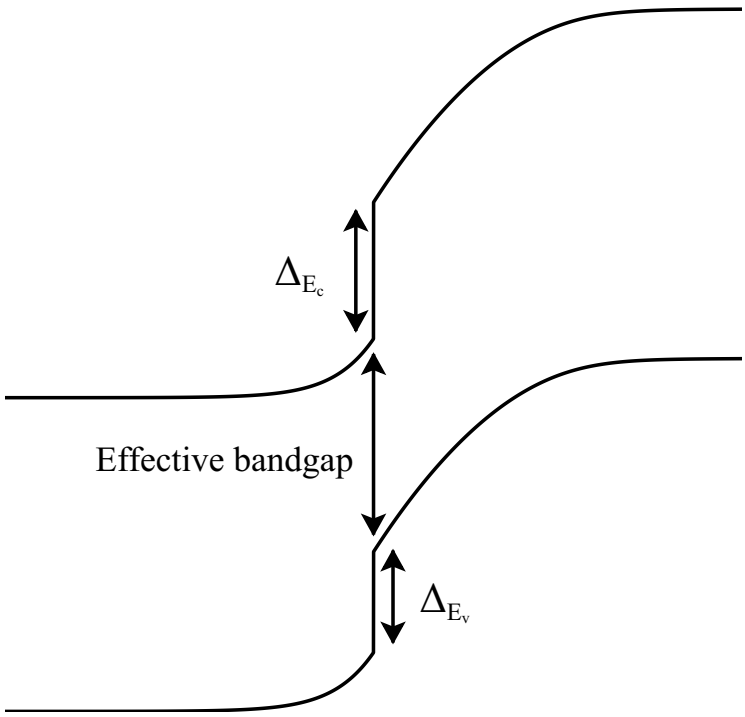

Figure 3.2: Illustration of a type-II heterostructure tunnel junction. The barrier to current flow is reduced by the sum of the heterojunction discontinuities (Δ_{E_c} and Δ_{E_v}) from the largest bandgap of the alloys.

for tunnel junctions with minimal increase in optical losses. The sub-bandgap absorption is localized near the heterostructure interface, resulting in very low single-pass absorption. However, the depletion width is dominated by the lowest doped layer of the tunnel junction making free-carrier-absorption loss a concern. This tunnel junction configuration is particularly attractive for solar cell applications where the band-to-band absorption is the dominant parasitic loss. For laser applications, where free carrier absorption loss is generally the dominant parasitic concern, the heterojunction approach is far less promising. Additionally, the choice of substrate affects the band-discontinuities available, limited by strain considerations. Devices grown on InP and GaSb both have lattice matched alloys with large band discontinuities; however, devices on GaAs substrates do not have access to favorable band alignments for tunnel junctions.

An alternate approach to low resistance tunnel junctions involves utilizing defects in the high-field region of the tunnel junction to enhance carrier recombination or generation. Figure 3.3 illustrates defect-enhanced tunneling in low-temperature-grown (LT) GaAs tunnel junctions. Trap assisted tunneling in low-temperature grown GaAs, combined with increased silicon dopant concentration, has resulted in $<10^{-4}\,\Omega\text{cm}^2$ tunnel junction resistivity [119]. However, performance significantly degrades upon thermal annealing making this approach poorly suited to interconnecting optical devices.

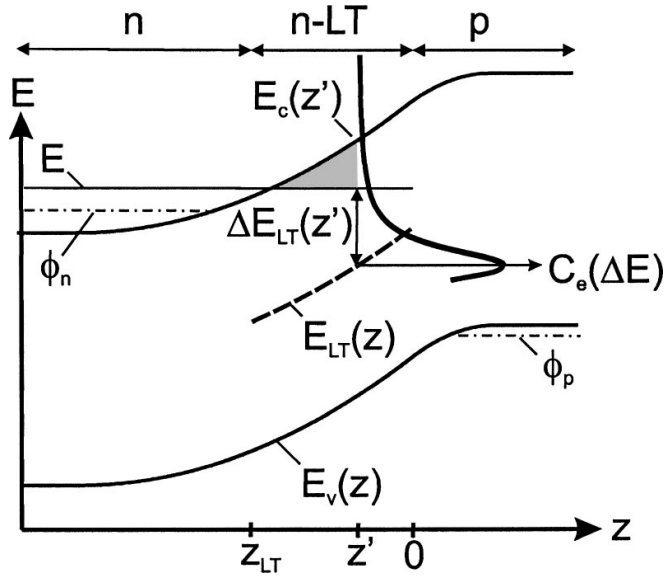

Figure 3.3: Schematic band structure of an n-LT diode under forward bias. At this bias and above the deep defects in the whole LT layer become energetically accessible as recombination centers. The current increase is therefore solely due to increasing tunneling probability. The diagram Ce(E) depicts the expected decrease of electron capture probability for inelastic tunneling of an electron in the n layer with an energy E into a deep defect at the position z within the LT layer. From [31].

3.3 Embedded Semimetallic Nanoparticles

One particularly attractive class of defect-enhanced tunnel diodes employ semimetallic rare-earth pnictide nanoparticles at the $p-n$ interface. The growth of the nanoparticles is described in detail in Chapter 2. The RE-V nanoparticles are attractive for tunnel junction because they provide a manifold of states to tunnel into, the interface is thermodynamically stable, and growth conditions are compatible with conventional III-V growth. Additionally, by controlling the morphology of the nanoparticles, the parasitic absorption can be tuned away from the devices active band. From a device perspective, the RE-V nanoparticles pin the Fermi-level at the interface of the $p-n$ junction. This breaks the tunneling into a two-step process, each with reduced height and width. Because the nanoparticles pin the Fermi-level, the built in potential dropped on each side of the tunnel junction is controlled by the nanoparticles and not the doping. As such, the two sides of the tunnel junction are isolated and can be independently optimized.

The two materials systems presented in this section represent the limiting cases of nanoparticle enhanced tunnel junctions in terms of suppressing band-to-band absorption or free carrier absorption losses in tunnel junctions. ErAs nanoparticles are used in GaAs tunnel junctions to increase the tunnel current of a wide-bandgap semiconductor by employing RE-V nanoparticles that pin the Fermi-level near midgap. Nanoparticles with midgap alignment provide the maximum enhancement in tunneling current. Additionally, GaSb tunnel junctions with ErSb nanoparticles embedded at the interface

are introduced to obtain lightly p-doped tunnel junctions well suited to the cladding/core interface of mid-IR GaSb-based lasers. The ErSb nanoparticles pin the Fermi-level near the valence band in GaSb, resulting in very low potential drop across the p-side of the junction regardless of doping concentration.

In both cases, the band-to-band and free-carrier absorption losses of the tunnel junctions are greatly reduced compared to conventional tunnel junctions with comparable electrical conductivity, making this class of tunnel junction particularly attractive for embedded interconnects in optical devices. Additionally, the thermal stability of the interface is promising for optical devices requiring post-growth thermal process, such as the dilute-nitrides discussed in Chapter 2.

3.3.1 GaAs-Based Tunnel Junctions

The first attempt to embed ErAs nanoparticles at the interface of $p{-}n$ junctions resulted in $\sim 10^3\times$ enhancement in the tunneling current under forward and reverse bias [31]. In a side-by-side comparison to defect-enhanced tunneling with low-temperature grown GaAs, the ErAs nanoparticle enhanced tunnel junctions exhibited higher conductivity in both forward and reverse bias. Additionally, no Esaki peak was observed making the ErAs tunnel junctions particularly well suited to solar cell applications [31]. In fact, GaAs tunnel junction employing ErAs nanoparticles was used to interconnect the AlGaAs and GaAs cells in a tandem solar cell [1]. ErAs nanoparticle-enhanced tunnel junctions were also used to interconnect $p{-}i{-}n$ junctions in nip-nip

photomixer for tera-Hertz generation [32]. However, initial investigation into the ErAs tunnel junctions remained prohibitively resistive for applications requiring current densities in excess of $1\,\mathrm{kA/cm^2}$ such as VCSELs.

Because ErAs has a broad growth space, and the nanoparticle morphology is known to be sensitive to the growth conditions [50, 120, 121], one might expect that the tunnel junction resistivity could be improved by optimizing the growth of the ErAs layer. The particle morphology is a strong function of surface mobility of erbium adatoms. As such, the growth temperature, arsenic overpressure and ErAs growth rate all contribute to the morphology of the ErAs seed crystals. After the formation of ErAs nanoparticles, additional erbium preferentially incorporates at the exhisting ErAs nanoparticles. This additional ErAs deposition results in lateral expansion of the ErAs nanoparticles increasing the surface coverage with little effect on the vertical shape of the nanoparticles. Note however, the growth temperature has a strong effect on the vertical height [22].

GaAs tunnel junctions with ErAs nanoparticles embedded at the interface were grown under varying growth conditions. In all of the tunnel junctions the n-type (Si) doping was $5\times10^{18}\,\mathrm{cm^{-3}}$ and p-type (Be) doping was $1\times10^{19}\,\mathrm{cm^{-3}}$. Figure 3.4 shows the layer structure for the nanoparticle enhanced tunnel junctions. Because all of the samples were grown on an n-type substrate, the nanoparticles were deposited at the n-interface of the tunnel junction. Because of the embedding nature of ErAs growth, the nanoparticles are slightly shifted to the n-side, potentially resulting in asymmetric contact

to the two sides of the tunnel junction.

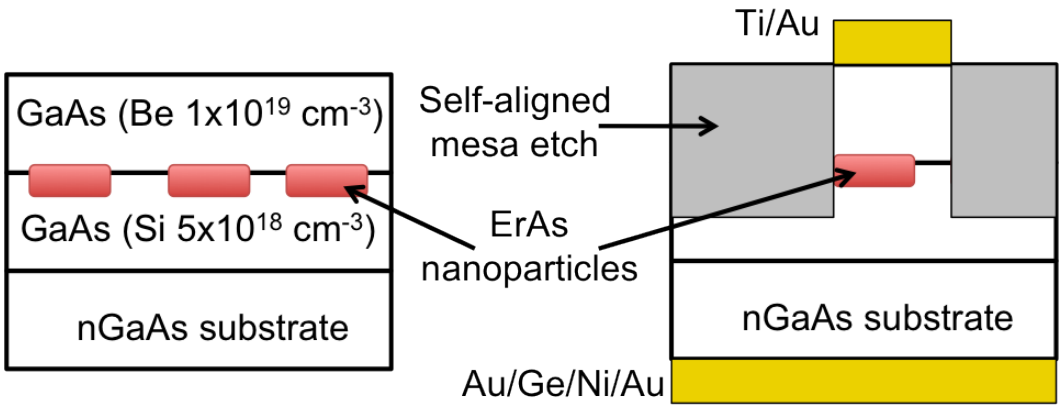

Figure 3.4: Layer structure (left) and device structure (right) of ERAs nanoparticle-enhanced tunnel junctions.

Samples were processed into mesa structures. A patterned Ti/Au top contact was evaporated and lifted off. A blanket back metalization of Au/Ge/Ni/Au was evaporated. The top contact was used as the mask for a self-aligned inductively coupled plasma etch using $SiCl_4$/Ar chemistry.

Figure 3.5 plots the J-V for GaAs tunnel junction employing varying ErAs nanoparticle deposition at the interface of the $p{-}n$ junction. All of the samples were grown at 530°C substrate temperature. Note that the growth temperature was ∼70°C lower than the first investigations of the ErAs enhanced tunnel junctions [1, 31]. The sample with 1.33 ML ErAs deposition exhibited specific contact resistivity of $\sim 1.7{\times}10^{-4}\,\Omega\text{cm}^2$ compared to the $1{\times}10^{-3}\,\Omega\text{cm}^2$ previously observed. This 10× enhancement in tunneling resistance is likely due to the reduced growth temperature as the amount of ErAs

deposition is similar. Additionally the p-type doping was actually reduced by a factor of 5×. One particularly interesting observation was increasing the ErAs

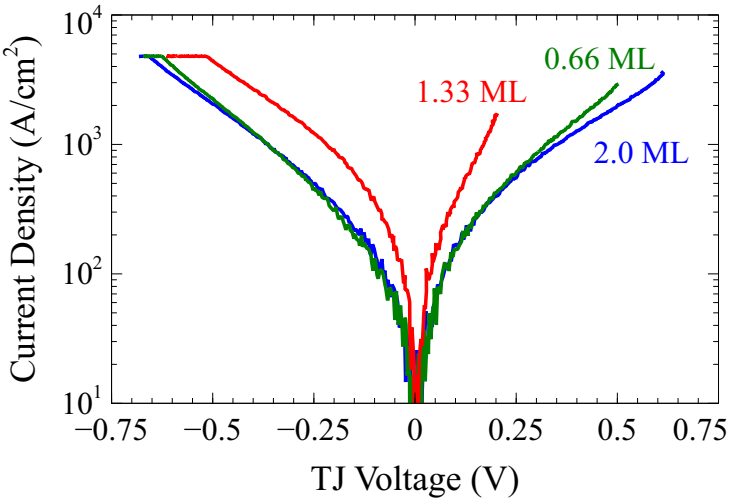

Figure 3.5: Conductivity vs voltage for ErAs nanoparticle enhanced tunnel junctions of varying deposition. Adapted from [50]

deposition from 1.33 ML to 2.0 ML resulted in a reduction in the conductivity of the tunnel junction despite the increased surface coverage of ErAs.

One possible interpretation of the decrease in resistivity despite the increasing surface concentration was a competition between Schottky barrier height and surface coverage resulting in an optimal ErAs deposition. Study of the Schottky barrier height vs substrate orientation found that the height of the barrier was a strong function of the substrate orientation for ScErAs films lattice matched to GaAs [16]. One would expect larger surface coverage of low barrier $< 110 >$ facets for smaller particles. Unfortunately, from macroscopic measurements, we can only make inferences from general trends in particle

morphology with growth conditions. To confirm particle size dependence of conductivity, current measurements through individual nanoparticles would be required.

3.3.2 Microscopic Tunnel-Junction Measurements

The measurement of mesa tunnel junction structures was successful in identifying growth parameters for which conductivity is optimized. However, with minimum mesa radii $\sim$15 μm, only macroscopic average of the conductivity of ErAs tunnel junctions could be obtained. In order to discern the physical mechanism for the enhanced tunneling current at low temperatures and optimized deposition, local current density measurements must be conducted. Because the ErAs nanoparticles are separated by 10s of nanometers, local probe measurements with conductive atomic force microscopy, widely used to characterize dislocations and current leakage paths on III-V semiconductors in nanoscale [122–124], can reveal details of the tunneling behavior on a length scale similar to the critical dimension of the ErAs nanostructures. The sample structure and measurement setup for microscopic current measurements is illustrated in Fig. 3.6. A critical parameter when designing the structure was found to be the thickness of the GaAs overgrowth. If the thickness was too great, lateral resolution is lost; however, too thin overgrowth results in oxidation of the ErAs nanoparticles. We chose the p-type cap thickness of 1.5 nm, the minimum thickness where there was a clear enhancement in samples with ErAs nanoparticles compared to control samples without ErAs

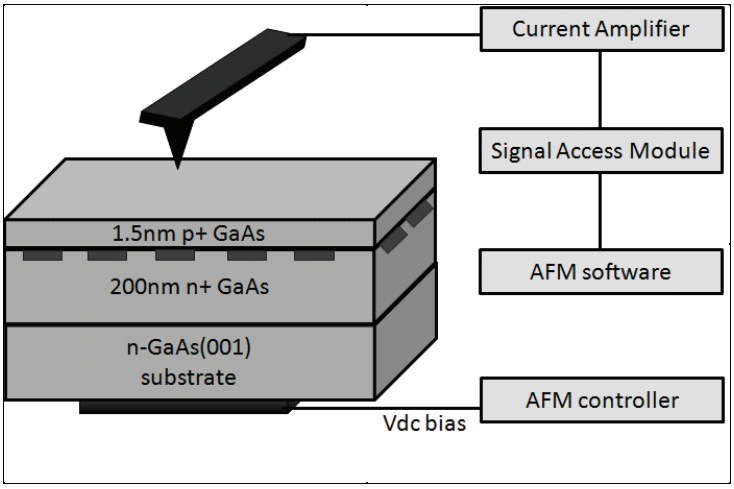

Figure 3.6: Illustration of sample structure and measurement setup for conductive atomic force microscopy of ErAs nanoparticle enhanced tunnel junctions. From [125].

nanoparticles. Scans of the local conductivity were taken with the sample stage biased +0.5 V from the probe tip. Scans give surface topography and local current simultaneously.

Figure 3.7 shows the local current images for GaAs tunnel junction, with 1 ML of ErAs embedded at the $p-n$ interface, grown with varying substrate temperatures of 485°C, 515°C, 545°C, and 575°C. The topography is also shown from the 485°C sample. The contrast observed in the conductivity scans originates from the large difference in tunnel junction resistivity when ErAs nanoparticles are present below the sample probe tip. The integrated current density for the $1\,\mu\text{m}\times1\,\mu\text{m}$ scan area are plotted in Figure 3.7. With 1 ML ErAs deposition, little variation in the average current density is ob-

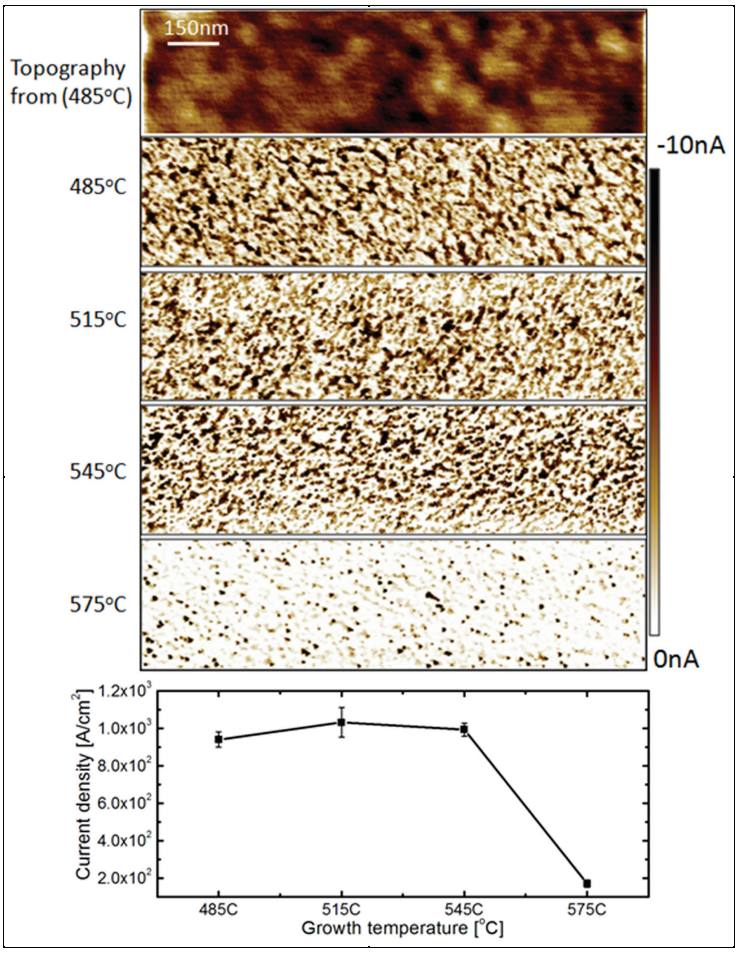

Figure 3.7: Conductive atomic force microscopy of ErAs nanoparticle enhanced tunnel junction grown at varying substrate temperature. The average current density over $1\,\mu\text{m} \times 1\,\mu\text{m}$ scans is plotted below. Adapted from [125].

served for samples grown in the range 485−545°C; however, a significant drop in the current density is observed for the highest temperature growth, 575°C. This degradation in current density is primarily due to a decrease in surface coverage rather than a reduction in the magnitude of the current in the areas exhibiting ErAs nanoparticles.

The surface coverage dependance can also be investigated by varying the amount of ErAs deposition. Because of the preferential incorporation of erbium adatoms into ErAs nanoparticle seeds, after sufficient erbium deposition to form ErAs nanoparticles, additional erbium incorporates at the edges and the nanoparticles grow laterally until coalescing into a film [30]. As such, to a good approximation the surface coverage is linear with increasing deposition.

Samples sets consisted of 0.4 ML, 0.8 ML, 1.2 ML, and 1.6 ML ErAs deposition. Figure 3.8 shows the cAFM images of sample sets grown at 530°C and 575°C. At each deposition the sample grown at 530°C exhibited higher current density than the corresponding sample grown at 575°C. The current density scales linearly with deposition over the entire range for the samples grown at 530°C. However, each sample grown at the elevated growth temperature has lower current density and corresponding reduced surface coverage. Because equal amounts of ErAs was grown, this implies that the vertical extent of the nanoparticles increases dramatically at the growth temperature of 575°C. This observation is in contrast to the conventionally accepted growth method that, electrostactic stabilization of the rocksalt crystal structure governs nanoparticle formation, and subsequent erbium expands the nanoparticles laterally

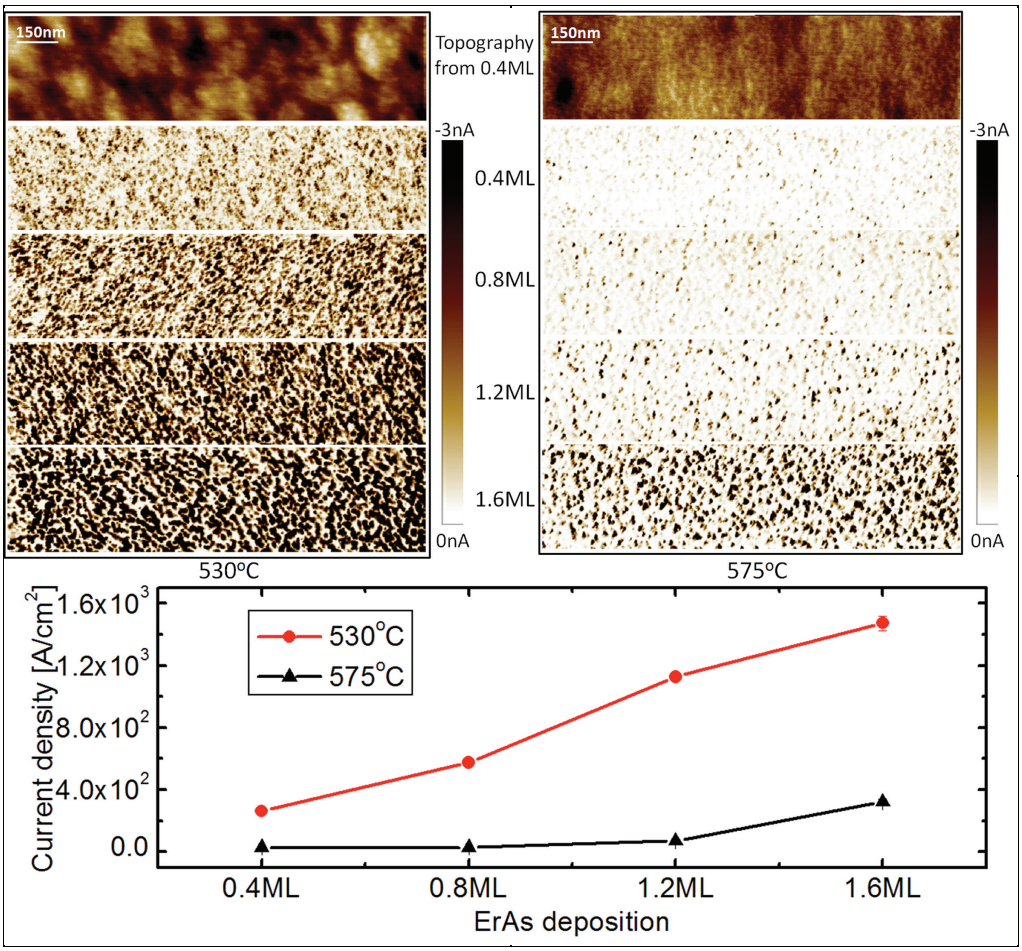

Figure 3.8: Conductive atomic force microscopy measurements of ErAs nanoparticle enhanced tunnel junctions of varying deposition grown at 530°C (top left) and 575°C (top right). The average current density over the entire scan area is plotted below. Both samples sets show a monotonic increasing trend with increased ErAs deposition, however the surface coverage for the higher growth temperature is much lower. From [125].

[20, 29, 30, 50, 126]. Instead, these conductivity results suggest nanoparticle formation that is dependent on the growth conditions, in particular the growth temperature [46, 75].

3.3.3 Graded-Heterostructure Tunnel Junctions

The morphology and the surface coverage of ErAs nanoparticles was found to play important roles in the resistivity of the GaAs tunnel junctions employing the ErAs nanoparticles at the $p{-}n$ interface. The macroscopic and microscopic measurements of the tunnel junctions are consistent with tunneling limited by the n-type Schottky barrier. Even so, the ErAs/GaAs tunnel junctions are comparable to the best observed on the GaAs material system [119, 127]. Further improvement in the tunnel current will require reduction in the barrier to current flow either by enhancing the doping or reducing the barrier height.

The Schottky barrier of ErAs films has been show to follow the universal alignment model very well [128], that is the ErAs Fermi-level can be assumed to be constant in energy and the relative alignment between ErAs and alloys of differing composition can be found from the difference band-discontinuities of the alloys. Therefore, grading the n-side of the tunnel junction with an alloy that has a negative conduction band offset to GaAs will reduce the n-side Schottky barrier. Unfortunately, alloys with large negative conduction band offsets to GaAs also have an unacceptable amount of strain. The exception of course are dilute-nitride materials [129], however erbium is highly reactive

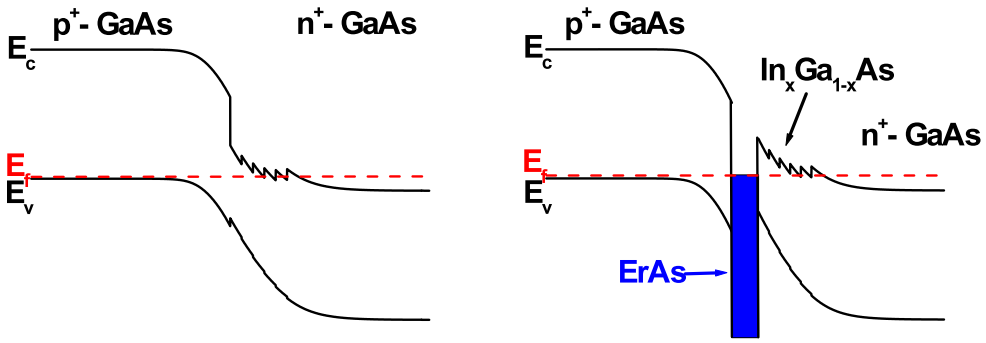

Figure 3.9: Calculated band diagrams for GaAs tunnel junctions with GaInAs graded n-sides with and without ErAs nanoparticles embedded at the tunnel junction interface. The ErAs nanoparticle width is increased for illustration.

with nitrogen, so much so that after dilute-nitride growths, the chamber will not pump down until the erbium cell has been outgassed above normal growth temperatures.

Proof of principle devices are investigated that utilize digital grades from GaAs to $Ga_{0.5}In_{0.5}As$ on the n-side of the tunnel junction. Band structures for conventional and nanoparticle enhanced tunnel junctions employing the GaInAs grade are shown in Figure 3.9. The grade consisted of linear compositional grade in 5 steps of 2 nm each. The conductivity of GaAs tunnel junction with and without ErAs nanoparticle enhancement are compared to similar junctions with GaAs to GaInAs digitally graded n-side in Fig. 3.10. There is clear enhancement in the tunneling current for the graded tunnel junction compared to the abrupt junction for the samples without ErAs nanoparticles.

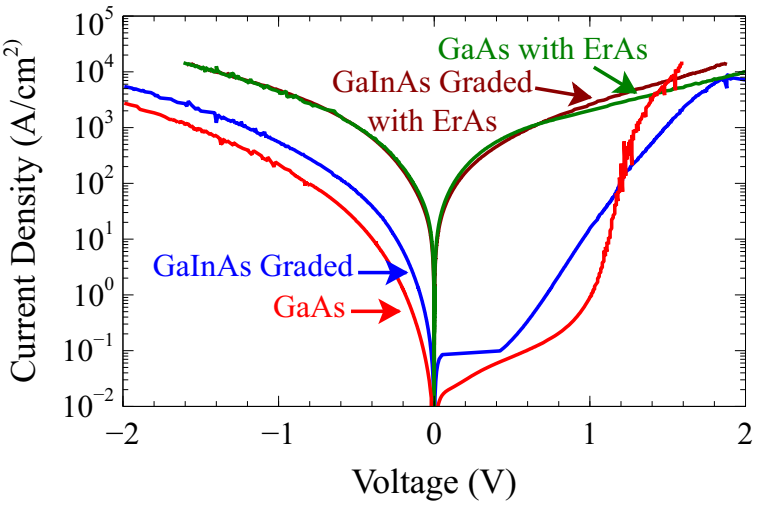

Figure 3.10: Conductivity vs voltage for abrupt GaAs and graded GaInAs tunnel junctions with and without ErAs nanoparticle embedded at the tunnel junction interface.

However, there is very little difference between the abrupt and graded tunnel junctions with ErAs nanoparticles. This suggests that the p-side of the tunnel junction plays a more important role in the ErAs nanoparticle-enhanced tunnel junctions than hypothesized. This could be due to the reduced p-type doping or the embedding of the ErAs nanoparticles.

3.3.4 GaSb-Based Tunnel Junctions

Extension of the emission wavelength of type-I diode lasers to be competitive with QCLs at and beyond the 4 μm wavelength range requires improvement of the quantum well active region and reduction of the cladding free-carrier absorption loss. Recent progress with the dilute-nitride active re-

gion in GaSb materials is promising for the QW active region [104]. Here we introduce a method to develop low-p-type doped tunnel junctions to replace the p-type cladding in edge emitting GaSb-based diode lasers.

Unlike GaAs, GaSb has a small native bandgap. As such, high quality GaSb tunnel junctions are readily available [130]. Additionally, alloys with favorable band alignments for low resistivity tunnel junctions are easily lattice matched to GaSb substrates (namely InAsSb/GaSb). While such tunnel junctions have been employed successfully in interband cascade lasers (ICLs), the optical parameters are not well suited to confining the optical mode at cladding/core interfaces. An alternate approach is to utilize embedded metal nanoparticles to relax the constraint on the lowest doping level employed in a tunnel junction.

One dimension poisson simulations of conventional and nanoparticle enhanced tunnel junctions were conducted using the commercial software package Bandprof. The ErSb and GaSb materials parameters were from Ref. [17]. The ErSb/GaSb material system is particularly attractive for producing highly mismatched doping profiles with little effect on tunnel junction conductivity because $\Delta_{Ec} >> \Delta_{Ev}$. Therefore, the tunnel junction electrical properties are dominated by the n-side of the tunnel junction over a large range of p-type doping levels. The equillibrium band diagrams for conventional and nanoparticle enhanced tunnel junctions were calculated for fixed n-type doping concentration of $5\times10^{18}\text{cm}^{-3}$ and varying p-type doping concentrations. The simulated band diagrams are shown in Fig. 3.11. Looking at the depletion regions and

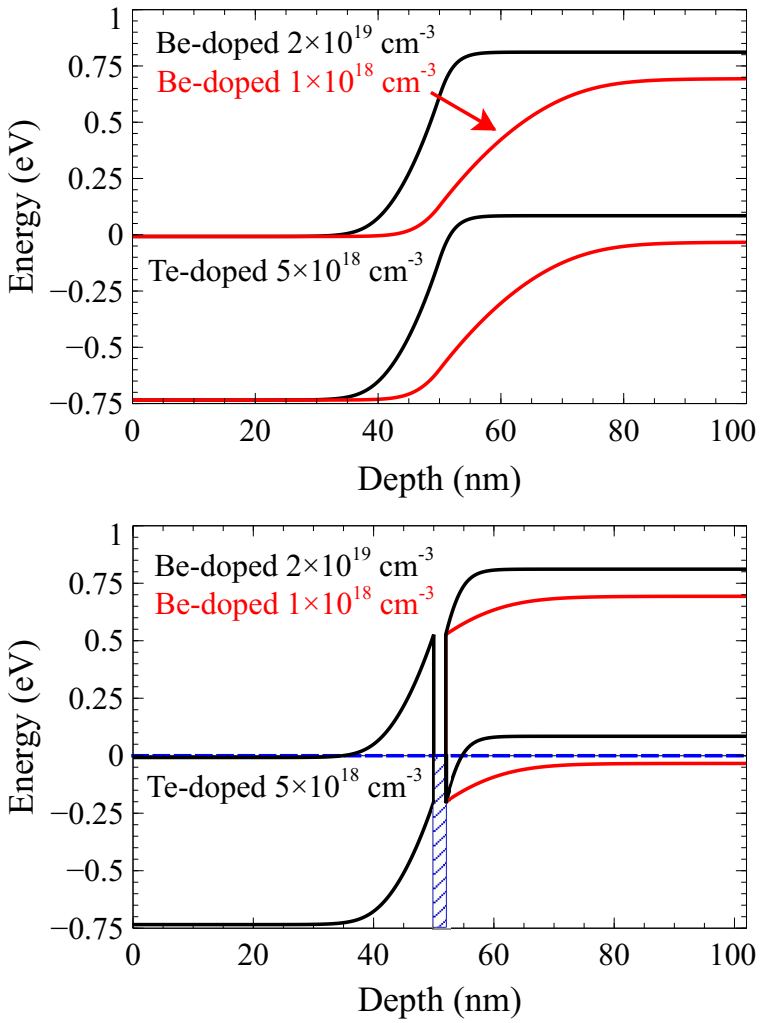

Figure 3.11: Calculated band profiles for conventional GaSb tunnel junctions and ErSb nanoparticle enhanced tunnel junctions of varying p-type doping.

the built in potential, the advantage of the ErSb nanoparticle enhanced tunnel junctions become apparent. In conventional tunnel junctions, the tunneling probability is sensitive to both doping profiles. The depletion width and the built-in voltage drop are both primarily on the lowest doped side of the $p-n$ junction. As a result, tunnel junctions with mismatched doping profiles are generally prohibitively resistive. The ErSb nanoparticles offer a path to reduction in the doping profile on the p-side of the tunnel junction due to the pinning of the Fermi-level at the semiconductor/semimetal interface. Because the barrier is set by the particle morphology, the built-in potential dropped on either side of the tunnel junction is fixed without regard to the doping on either side. The small Schottky barrier of ErSb nanoparticles, only $\sim 0.2\,\mathrm{eV}$ barrier for holes [17], allows for a large reduction in p-type doping (2×10^{19} to $1\times10^{18}\,\mathrm{cm}^{-3}$) with only a modest increase in the barrier width on the p-side. Notice, the n-side of the tunnel junction is not effected by the change in p-type doping, which is in stark contrast to the conventional tunnel junction case.

When biasing the nanoparticle-enhanced tunnel junction the portion of the applied bias that is dropped across each side of the nanoparticle layer is set by the current continuity condition. Because of the large density of states at the Fermi level, the nanoparticles can accommodate the positive or negative charge required without substantial movement Fermi level within the nanoparticles.

Figure 3.12 plots the current density vs voltage for the set of GaSb tunnel junctions. All of the tunnel junctions were grown at 460°C with n-type

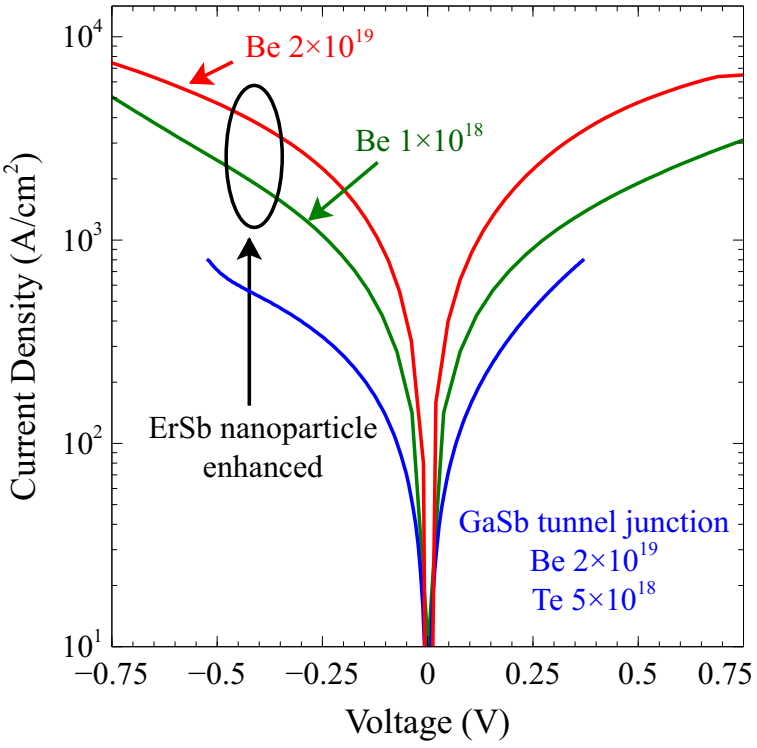

Figure 3.12: Conductivity vs voltage for ErSb nanoparticle enhanced tunnel junctions of varying p-type doping.

doping of 5×10^{18}cm^{-3}. The control tunnel junction had a p-type doping of 1×10^{19}cm^{-3}. Adding ErSb at the interface of an otherwise identical tunnel junction resulted in improvement of the tunneling current by $\sim$10$\times$. The modest improvement in the tunneling results from the little change in the n-type barrier owing to the band-alignment of ErSb in GaSb. This advantage is clear when a 10x reduction in the p-type carrier concentration has only a modest effect on the tunneling current. In fact, free-carrier absorption loss of the nanoparticle-enhanced tunnel junction is expected to be significantly lower than the more heavily doped conventional tunnel junction.

An estimate of the potential benefit of such low p-type doped tunnel junctions for use in cladding of diode lasers (Band diagram shown in Fig. 3.13) is calculated with the absorption data from [131]. The optical overlap for each layer in the cladding is calculated using finite-difference method. The cladding structures and corresponding internal loss values are shown in Fig. 3.14.

Switching from a p-type cladding to a conventional tunnel junction results in the improvement in internal loss from 21 cm^{-1} to 13 cm^{-1}. Replacing the conventional tunnel junction with a nanoparticle-enhanced tunnel junction results in reduction of both the series resistance and the internal loss. The nanoparticle-enhanced tunnel junction with low p-type doping concentration is calculated to have only 5 cm^{-1} of internal loss, corresponding to a $\sim$75% reduction in the cladding loss. The reduced cladding loss will be critically important to the development of long-wavelength lasers where parasitic losses, such as Auger recombination, increase dramatically at high threshold carrier

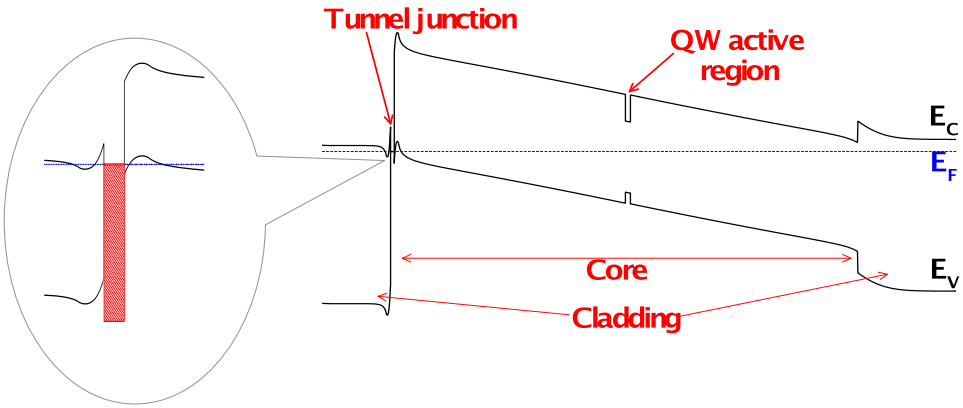

Figure 3.13: Band diagram for prototype laser employing n-type cladding and ErSb nanoparticle-enhanced tunnel junction to replace the p-type cladding.

concentrations.

3.4 Conclusion

Tunnel junctions with high electrical conductivity and low optical losses can be fabricated by embedding RE-V nanoparticles at the interface of $p-n$ junctions. The nanoparticles break the tunneling process into a two-step process with each barrier of reduced height and width compared to conventional tunnel junctions. Additionally the nanoparticles pin the fermi level at the interface of the junction which isolates the two sides. As such, each side of the tunnel junction can be independently optimized allowing for alloy grading the side with the highest component of the tunnel junction resistivity as well as independent optimization of the doping profiles.

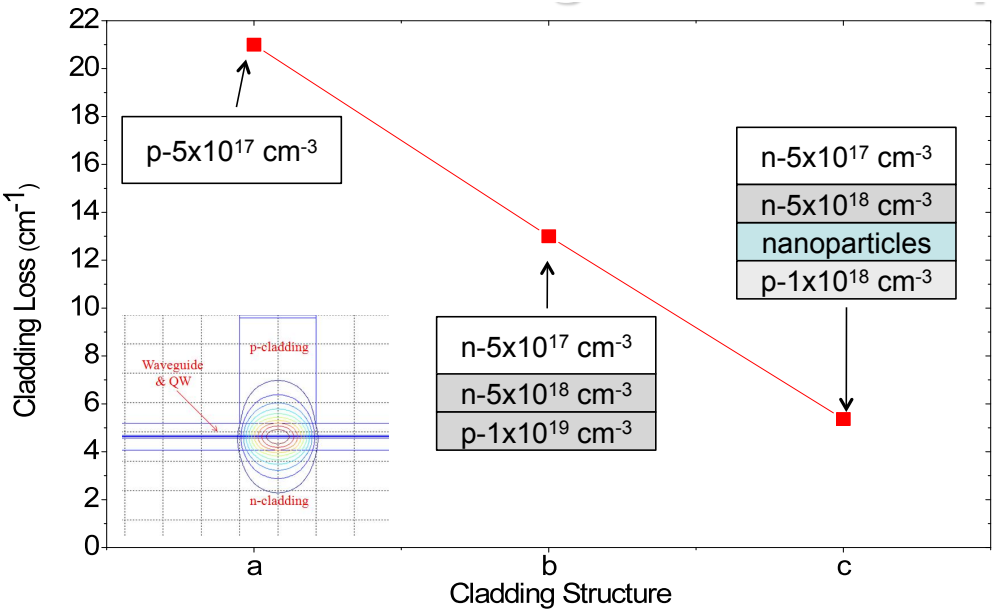

Figure 3.14: Calculated cladding loss from overlap of optical mode (shown in bottom left corner) with each layer for three cladding designs: (a) conventional low-doped p-type cladding, (b) n-type cladding with conventional tunnel junction, and (c) n-type cladding with ErSb nanoparticle-enhanced tunnel junction and reduced p-type doping.

The ErAs alignment in GaAs makes is well suited to greatly enhancing the tunnel junction resistivity as the Fermi-level pins near midgap. This results in enhancements in tunnelling currents of $\sim 10^5\times$ for optimized devices [50]. Grading the n-side of the tunnel junction had little to no benefit indicating that the p-side of the tunnel junction contributes significantly to the resistivity of the tunnel junction. An alternate interpretation is enhanced Be diffusion in the InGaAs leads to migration of the $p{-}n$ interface away from the ErAs nanoparticles reducing the efficiency in enhancing tunnel current.

The alignment of the ErSb in GaSb is near the valence band, well suited for high-conductivity tunnel junctions with low p-type doping.

Chapter 4

ErAs Nanostructures for Optical Devices

In previous Chapters, we have discussed how ErAs and ErSb can be incorporated at the interface of *p*-*n* junctions to greatly enhance tunneling currents and reduce the dependence of tunneling current on doping concentrations. With the applications of nanoparticle-enhanced tunnel junctions to multijunction solar cells and mid-IR lasers, the ability to integrate RE-V structures without degrading the optical properties of surrounding III-V materials will be critical to successfully enhancing optical devices with RE-V nanoparticle enhanced tunnel junctions.

While it has been demonstrated that the integration of ErAs nanostructures with III-V materials results in high structural quality materials, [27, 28, 30, 121] most of the devices based off these heterostructures have been based on the fast carrier recombination or phonon scattering at the ErAs nanoparticles. [29, 132] As such, optical quality of the ErAs containing materials had not been of paramount importance. In order to incorporate tunnel junctions containing ErAs or ErSb nanostructures into high-efficiency lasers and solar cells, the optical quality of the III-V materials must not be degraded. Non-radiative recombination reduces the open circuit voltage in solar cells and

increases the threshold current density in lasers.

The Gossard group incorporated ErAs nanoparticle enhanced tunnel junctions into a tandem AlGaAs/GaAs solar cell. The ErAs nanoparticle enhanced tunnel junction displayed higher efficiency than the tandem cell with conventional tunnel junction; however, the single junction GaAs cell had higher efficiency due to the increased short circuit current. While this result was particularly promising for the incorporation of ErAs nanostructures into high-quality optical devices, the experiment was insensitive to degradation in the optical quality of the tandem cell due to the poor control tunnel junction and mismatched absorption in the AlGaAs and GaAs cells [1].

Here we look in detail at the photoluminescence emission from structures grown with varying erbium cell temperature and with ErAs nanoparticles incorporated below optically active layers. The strength of the PL emission from a well designed PL structure is very sensitive to non-radiative recombination pathways induced by the integration with ErAs nanostructures. The PL structure, illustrated in Fig. 4.1, consisted of an $In_{0.15}Ga_{0.85}As$ quantum well, embedded in a GaAs absorbing region, surrounded by AlAs diffusion blocking layers. The AlAs is to prevent photogenerated carriers from diffusing to the surface or the underlying epitaxial layers. The quantum well was intentionally kept close to the underlying epitaxial layers to maximize the sensitivity to non-radiative recombination associated with defects associated with ErAs nanostructures. Growth conditions were chosen to be consistent with the highest electrical conductivity ErAs nanoparticle enhanced tunnel junctions.

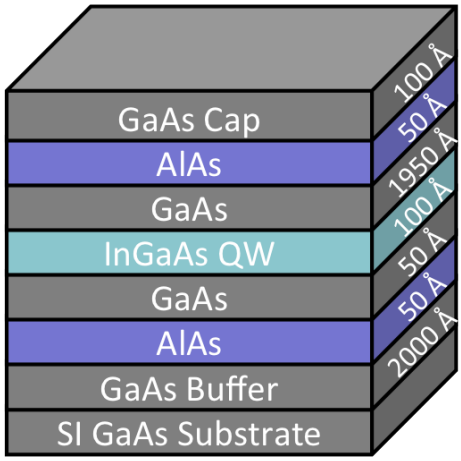

Figure 4.1: Photoluminescence structure used to quantify the optical quality of III-V layers. The AlAs barriers prevent photogenerated carriers from diffusing to the surface or the underlying epitaxial layers, providing maximum sensitivity to non-radiative recombination causing defects.

Specifically, the growth temperature was 530°C; the GaAs and AlAs growth rates were 0.3 μm/hr and 0.05 μm/hr respectively; the As/Ga BEP ratio was 15x; and the As flux held constant throughout the growth.

The band diagram for the PL structure along with critical physical processes are illustrated in Fig. 4.2. A 532 nm pump laser is absorbed primarily by the GaAs absorbing region between the AlAs carrier blocking layers. The potential process the photogenerated carriers can experience include, thermal excitation over diffusion barrier, radiative recombination in GaAs absorbing region, diffusion to InGaAs quantum well and subsequent radiative recombination, or recombine in a non-radiative manner in the GaAs or InGaAs quantum well. The two dominant processes for samples investigated appears to be ra-

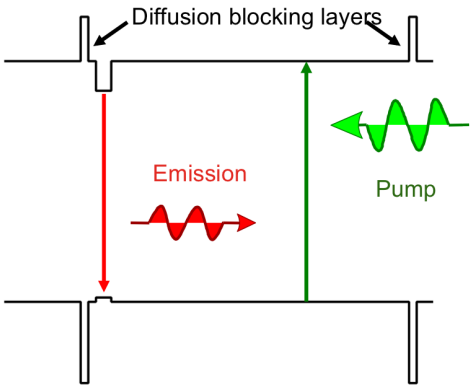

Figure 4.2: Band diagram of photoluminescence structure used to quantify the optical quality of III-V layers. Only carriers generated by absorbing the pump beam between the carrier blocking layers can contribute to emission. Because the carrier blocking layers prevent photogenerated carriers from diffusing to the underlying epitaxial layers or the surface, where nonradiative recombination would be expected, only defects in the PL structure are probed.

diative and non-radiative recombination in the InGaAs quantum well.

4.1 Parasitic Erbium Incorporation

There have been a few reports in the literature of parasitic erbium incorporating into layers grown with the erbium cell hot but the shutter closed [28, 128]. Because even moderate doping levels of erbium in GaAs result in substantial degradation in carrier lifetime [25], the erbium cell temperature is a key parameter in determining the optical quality of III-V layers, despite the closed erbium shutter.

While the origin of the parasitic erbium flux remains a matter for debate, there have been reports of parasitic incorporation around the shutters for other MBE grown materials. The so called arsenic drag effect has been shown to incorporate In, Al, and Ga into layers grown with the shutters closed and no line of sight to the substrate [133]. While the shutter prevents line of sight from the effusion cells to the sample, some molecules in the flux that would miss the sample are scattered off the As molecular flux and reach the substrate. This results in parasitic incorporation which is proportional to the As flux and the cell temperature. A similar effect has been seen in dilute-nitride materials [134].

While most university MBE machines are different, it should be noted that the MBE system that these structures were grown on was particularly unique. We have a Varian Gen II that was converted from a 2" substrate manipulator to a 3" substrate manipulator. This means that the wagon wheel (the water cooled fins between the cells) is a 2" model but the erbium cell is set back at the 3" source position. Also, the shutter on the erbium cell was a 2" shutter meaning that it is smaller and further away from the cell than the "standard" shutter position.

Samples were grown with the standard PL structure, illustrated in Fig 4.1, while varying the Er cell temperature. The peak PL intensity for each structure is shown in Fig 4.3. It is clear that the optical quality of the structures are degraded from some parasitic incorporation that is associated with the erbium cell. What is particularly alarming is the magnitude of the degra-

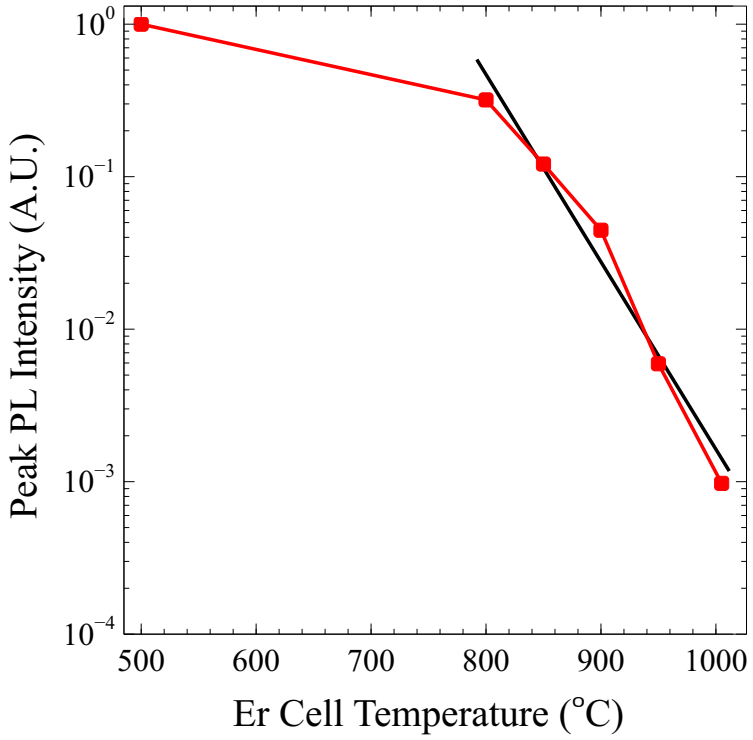

Figure 4.3: Peak PL intensity for PL structures, shown in Fig 4.1, with varying erbium cell temperature from the idle temperature of 500°C to the growth temperature of ∼1000°C.

dation. The peak PL intensity is degraded by ∼1000x when the erbium cell is at the growth temperature required for 0.05 ML/s ErAs growth rate. Additionally, the degradation is proportional to the erbium flux over the cell temperature range $800 - 1000$°C. Secondary ion mass spectrometry revealed the degradation to be non-radiative recombination associated with parasitic erbium incorporation into the PL structure.

The steady-state erbium incorporation into our PL structure was found

to be $\sim 5 \times 10^{16}$ cm^{-3} corresponding to a parasitic erbium flux of ($\sim 10^{9}$ cm^{-2}s^{-1}). This corresponded to a flux going around the shutter $\sim$1000x lower than the flux with the shutter open. This indicates the erbium cell must be cooled to the idle temperature prior to the growth of optically active layers if ErAs nanostructures are to be incorporated into optical devices.

4.2 Proximity to ErAs Nanoparticles

Originally, the motivation for looking at the optical quality of quantum wells grown in close proximity to the ErAs nanostructures was to spectrally align the surface plasmon resonance of the ErAs nanoparticles [70] to the emission wavelength of the quantum well to demonstrate plasmon-enhanced spontaneous emission in an epitaxial material system. Unfortunately, the near-IR absorption in the ErAs nanostructures appears not to be plasmonic in nature, as will be discussed in Chapter 5, so no such enhancement was observed. However, several key observations about the erbium incorporation mechanism are evident in this experiment.

Samples were grown with varying quantum well (QW) to ErAs nanoparticle separation. The spacing was varied two ways: The QW was moved within the PL structure such that the separation between the QW and the ErAs was varied. In this case the separation between the AlAs carrier blocking layer and the ErAs nanoparticles was held constant, illustrated in Fig. 4.4a; and the entire PL structure was grown after a variable GaAs spacer layer after the ErAs nanoparticle growth such that the QW to AlAs carrier blocking layer

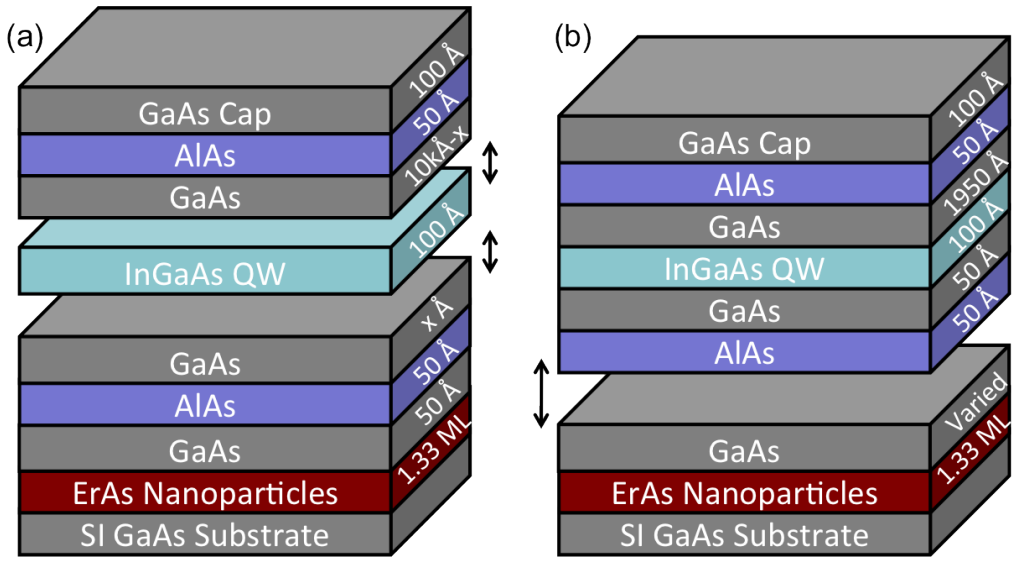

Figure 4.4: Structures investigated to observe the effect of ErAs nanoparticles on the spacing between the QW and the ErAs nanoparticles. (a) Structure consisting of a QW which is moved within a constant 1 μm absorbing region. (b) Structure consisting of a PL structure that is spaced from the ErAs nanoparticles by varying a GaAs spacer layer.

separation remained constant, illustrated in Fig. 4.4b. The PL structure in Fig. 4.4a utilized a 1 μm absorbing region compared to the 200 nm one utilized in the structure from Fig. 4.4b. The peak PL intensity for samples with and without ErAs nanoparticle layers are shown with varying QW to ErAs separation in Fig. 4.5, for the PL structure from 4.4a, and in Fig. 4.6, for PL structure from 4.4b. All of the samples show significant degradation compared to a standard sample grown with the erbium cell cooled. Each sample with an ErAs nanoparticle exhibited equal or higher PL intensity than the corresponding sample without ErAs nanoparticles. The magnitude of the en-

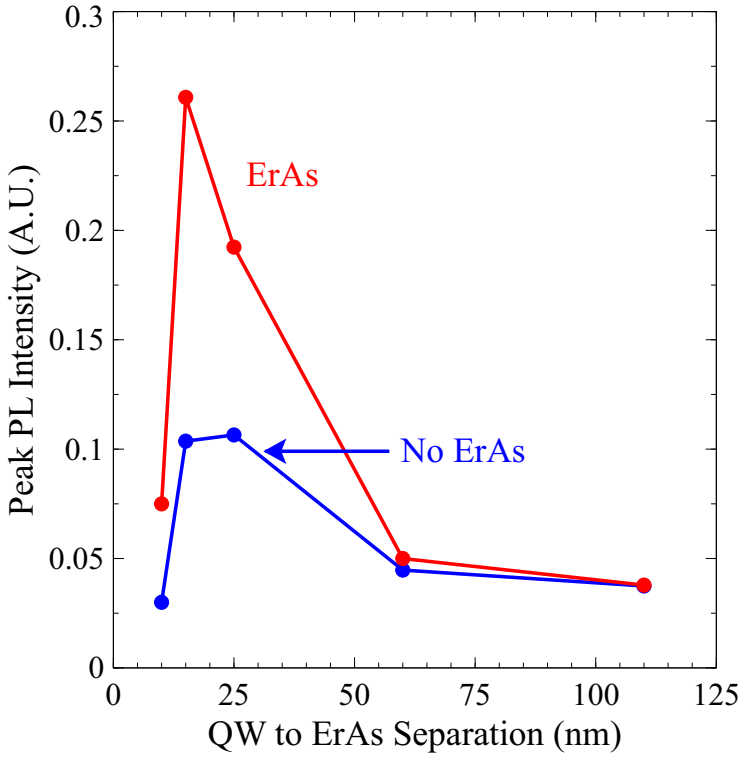

Figure 4.5: Peak photoluminescence intensity for varying spacer thickness between AlAs carrier blocking layer and embedded ErAs nanoparticle layer (structure illustrated in Figure: 4.4b). The lowest PL intesities are attributed to enhanced Er incorporation into the QW. The increased PL intensities are attributed to reduced surface concentration after the AlAs and ErAs interfaces.

hancement increases as the QW is brought into closer proximity to the ErAs nanoparticles.

The enhancement in PL intensity for QWs grown in close proximity to ErAs nanoparticles is attributed to reduction in the parasitic erbium doping after the nanoparticle layer. When ErAs nanoparticles are present at the surface, the surface erbium preferentially incorporates at the nanoparticle seeds

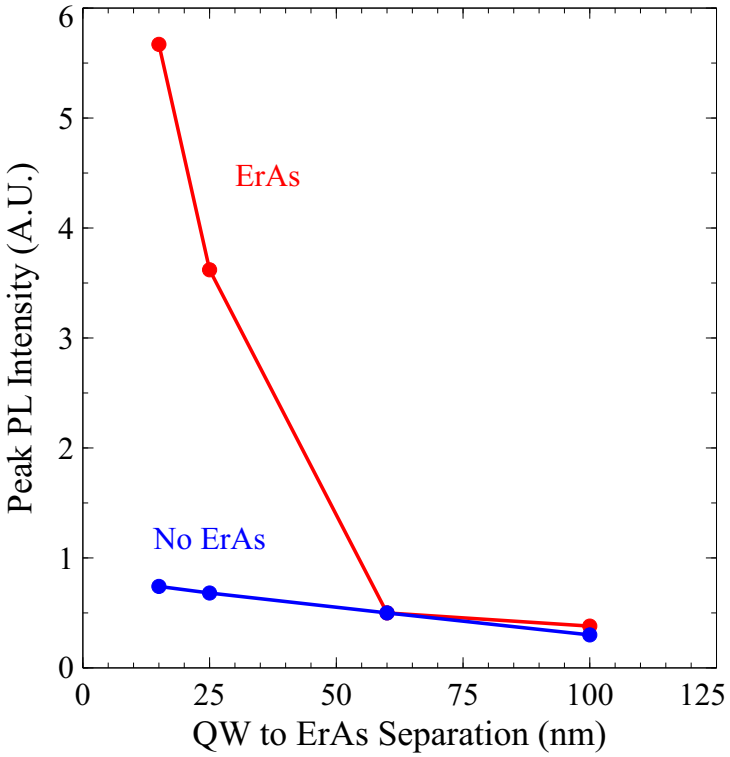

Figure 4.6: Peak photoluminescence intensity for varying spacer thickness between InGaAs quantum well and embedded ErAs nanoparticle layer(structure illustrated in Figure: 4.4a). The lowest PL intesities are attributed to enhanced Er incorporation into the QW. The increased PL intensities are attributed to reduced surface concentration after the AlAs and ErAs interfaces.

resulting in reduction of the surface density. Because the parasitic erbium doping is proportional to the surface concentration, this results in a region of low erbium doping while the surface erbium density refreshes to the steady-state level. To confirm this incorporation mechanism, secondary ion mass spectrometry (SIMS) measurements of Er, Ga, Al, In, and As concentrations, as well as other possible contaminants (O, C, Ta, Pd, Pr, Pb, W, Cr, Fe)

were conducted on the PL structure with the ErAs nanoparticle layer 15 nm from the InGaAs QW (sample structure from Fig. 4.4). The concentration profile for oxygen and erbium are shown in Fig. 4.7. Parasitic erbium in-

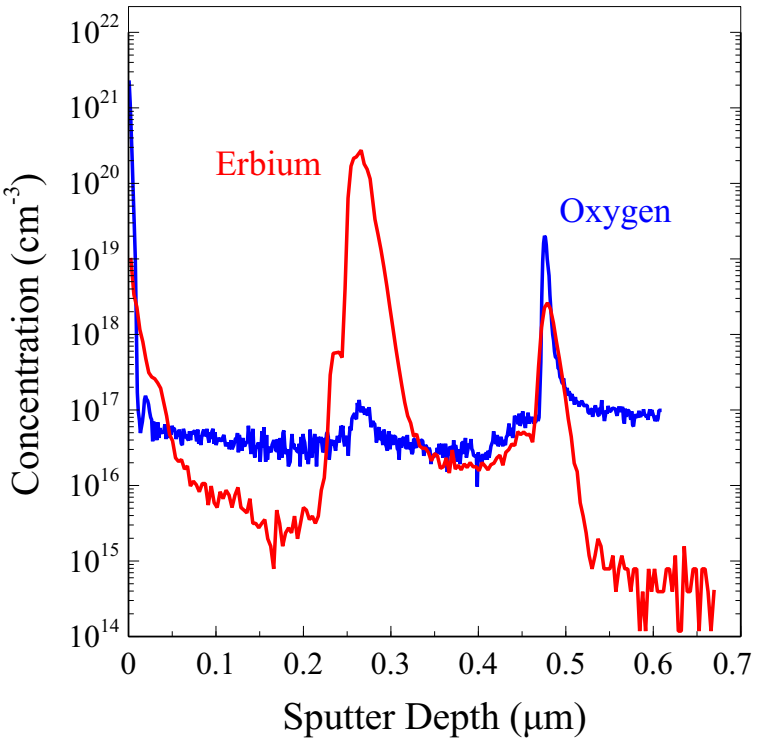

Figure 4.7: Secondary ion mass spectrometry scans of erbium and oxygen concentrations in photoluminescence structures grown with the erbium cell hot throughout the growth. The spikes in the erbium and oxygen concentration are located at the substrate/epi interface and at the ErAs nanoparticle layer. The reduction in parasitic erbium incorporation after the ErAs nanoparticle layer is due to preferential incorporation of surface erbium at the ErAs nanoparticle layer, which depletes the surface erbium concentration.

corporation into layers grown with the shutter closed but the erbium cell hot was clearly observed. The erbium incorporation prior to the growth of the

ErAs-nanoparticle-layer was ∼10 x higher than the concentration observed in the early stages of ErAs overgrowth. In the subsequent overgrowth, the erbium concentration increased until a large surface concentration was observed. While parasitic oxygen incorporation is observed at the substrate/epi interface and at the ErAs nanoparticle layer, there is no observable difference in the oxygen incorporation in close proximity to the ErAs nanoparticle layer.

4.3 Managing Parasitic Erbium

It is clear that to achieve high optical quality material in close proximity to ErAs nanoparticles, care must be taken to mitigate parasitic erbium incorporation. In particular, the parasitic erbium flux, due to the erbium effusion furnace, must be negligible, and the sample surface must be depleted of erbium prior to growing optically active layers. Because of the significant parasitic erbium flux, a growth interruption after the ErAs nanoparticle layer is required to cool the erbium cell. An illustration of the sample structure is shown in Fig. 4.8. The growth interruption is inserted after the ErAs nanoparticle layer and a thin GaAs spacer in order to allow for cooling of the erbium cell. Because our erbium cell was in a downward looking port (and the erbium charge was melted into the crucible), thermal stress from cooling the cell can be problematic. We used a slow ramp rate of ∼5°C/min resulting in ∼100 min growth interruption.

An initial attempt at overgrowing ErAs nanoparticles without degrading optical quality was to arsenic cap the wafer with the erbium cell hot in

leu of cooling the erbium cell. This would allow for batch growth of ErAs containing structure without cycling the erbium cell for each wafer. Figure 4.9 plots PL spectrum for a PL structure grown after As capping the ErAs nanoparticle layer and a thin (5 nm) GaAs spacer. After the erbium cell had been cooled to idle temperature, the sample was reloaded into the MBE and a PL structure with 200 nm absorbing region was grown after a thin GaAs spacer. The sample grown with the As-cap shows significant degradation in the PL intensity. We attribute this low PL intensity to parasitic erbium incorporation into the As-cap layer which accumulates at the surface when the As-cap is thermally desorbed. The high erbium surface concentration then

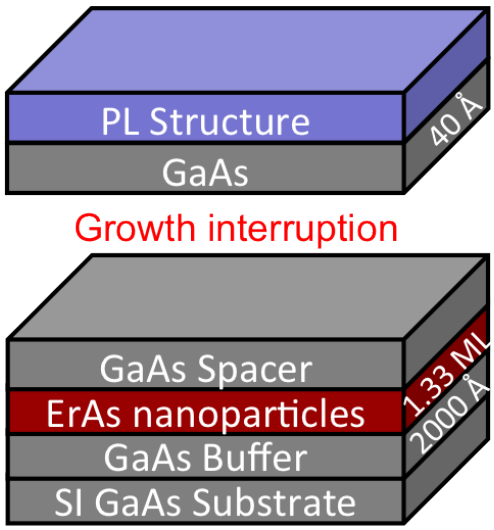

Figure 4.8: Illustration of the sample structure utilized to investigate methods of overcoming parasitic erbium incorporation into PL structures grown after ErAs nanoparticle layers. The growth interruption required to cool the erbium cell was ∼100 min.

segregates and incorporates into the subsequent PL structure.

The tendency of surface erbium to segregate and incorporate into layers grown after the ErAs nanoparticles requires some method to deplete the surface of erbium. Photoluminescence and SIMS indicated the propensity of ErAs nanoparticles to scavenge surface erbium suggesting the possible use of a near surface nanoparticle layer as a sink for surface erbium during the growth interruption. To investigate this path to realizing a low erbium surface concen-

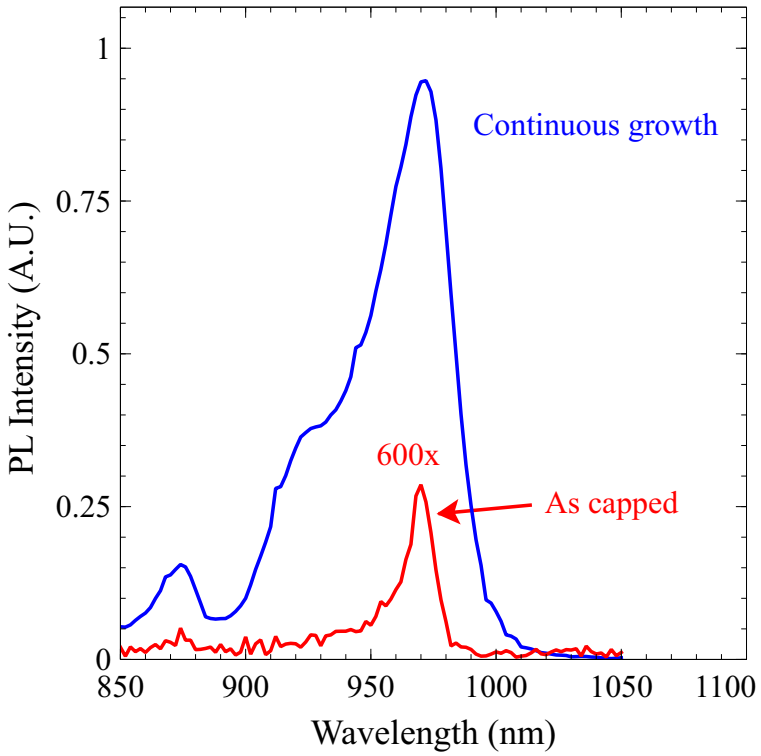

Figure 4.9: Photoluminescence spectrum for sample grown with the erbium cell idle and no ErAs nanoparticle layer as well as a sample that was As-capped after an ErAs nanoparticle layer, capped with 5 nm GaAs spacer.

tration, ErAs nanoparticle layers were grown with varying GaAs spacer prior to a growth interruption to cool the erbium cell. During the growth interruption, the substrate was heated to 600°C to enhance erbium diffusion through the GaAs spacer and to prevent parasitic oxygen from accumulating at the surface. The GaAs spacer layer thicknesses were chosen to be in 1, 3, 5, 7, 10 and 100 nm. The thicknesses were chosen to be consistent with the embedding depth of ErAs nanoparticles which tends to be $\sim 2-5$ nm. Photoluminescence spectrum for the 1 and 10 nm GaAs spacer thickness are shown in Fig. 4.10 along with a control that has no nanoparticle layer and was grown continuously with the erbium cell cooled to the idle temperature. The sample with 1 nm spacer shows very little degradation compared to control sample while the sample with 10 nm spacer is $>$ 300x lower in peak intensity. The largest difference in the PL spectrum between the control and the 1 nm spacer sample is the shoulder on the main QW peak. This corresponds to the excited state in the valence band of the QW. Because the parasitic erbium is a fast hole trap, this could imply that still some erbium is incorporating. It should be noted that the total QW to ErAs nanoparticle separation for this sample is just 15 nm making it as sensitive as possible to the surface erbium remaining at the growth interruption. Figure 4.11 plots the peak PL intensity for varying GaAs spacer thickness. There is essentially no difference between the samples with 10 and 100 nm GaAs spacers, indicating that the ErAs nanoparticles have no effect on the surface erbium when embedded 10 nm or deeper. The range between 1 nm and 10 nm shows a monotonic decrease in peak PL intensity,

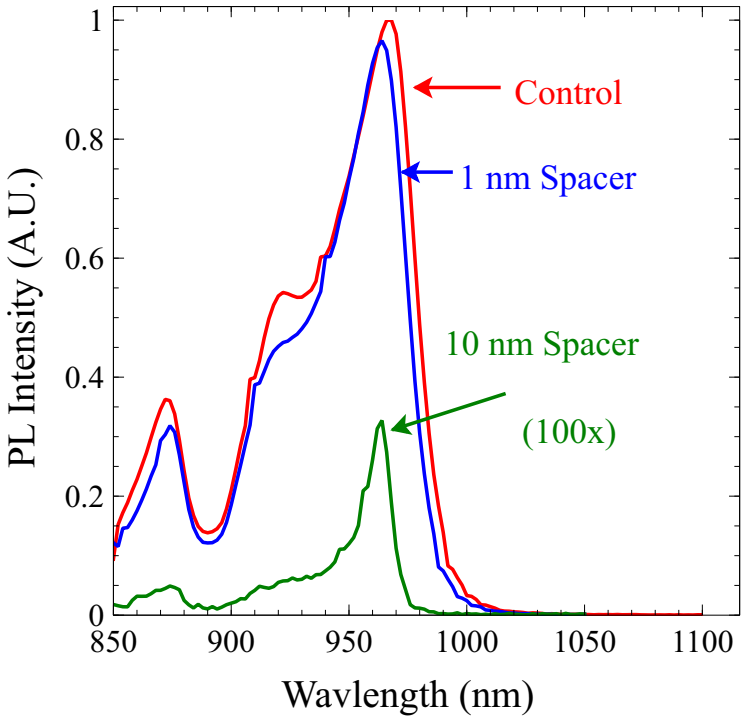

Figure 4.10: Photoluminescence spectrum for sample grown without ErAs nanoparticle layer as well as samples with 1 and 10 nm GaAs spacers.

suggesting the final surface concentration of erbium increases with the GaAs spacer thickness.

4.4 Conclusions

High optical quality III-V layers can be integrated with ErAs nanostructures, even with very little spacing between the III-V emitting layers and the ErAs nanostructures. Care must be taken to ensure that both the parasitic erbium flux and the erbium surface concentration are low prior to the

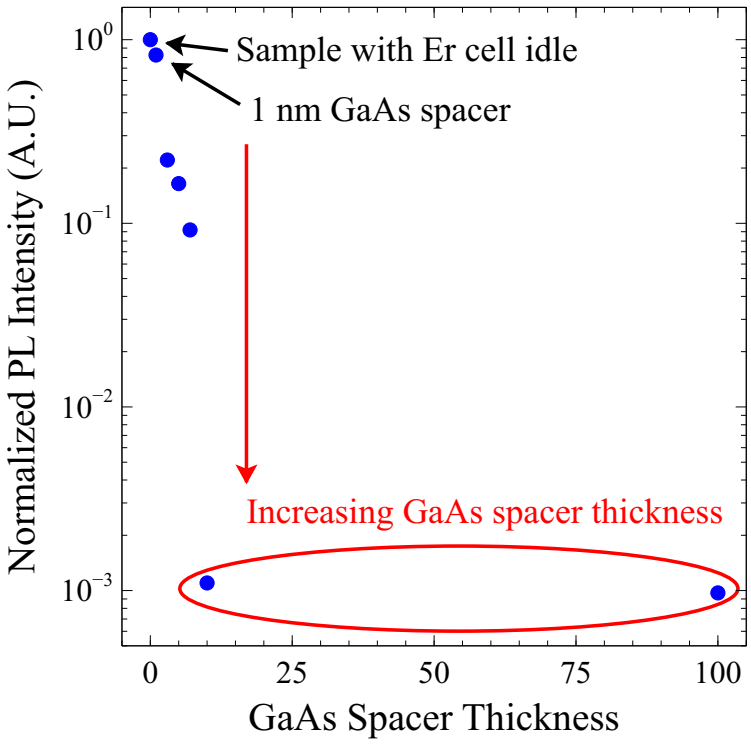

Figure 4.11: Peak PL intensity for samples grown with varying GaAs spacer layers after nanoparticle growth, prior to the growth interruption to cool the erbium cell.

growth of any optically active regions. The key parameter for realizing a low erbium surface concentration was found to be the spacing between the ErAs nanoparticle layer and the surface during the growth interruption to cool the erbium cell. This provides evidence for the diffusion of erbium through the GaAs cap to incorporate at subsurface ErAs nanoparticles.

Chapter 5

RE-V Plasmonics

5.1 Rare-Earth Pnictide IR-Absorption

There has been much debate as to the origin of the near-IR absorption features displayed by ErAs nanostructures [70, 71] and the mid-IR absorption features in ErSb [18, 72]. Several properties of the absorption suggest surface plasmon resonance as the origin of the absorption peak [70, 72]. For example, the particle morphology alters the peak absorption wavelength such that large particle result in longer wavelength absorption. Additionally, oblong particles show polarization dependence with the absorption of light polarized along the long direction at longer wavelengths.

Here, the ErAs nanoparticle morphology is tuned to spectrally shift the peak absorption wavelength to a sufficiently short wavelength for emission from a pseudomorphically-strained InGaAs quantum well. The absorption peak is aligned to the quantum well emitting structure in an effort to observe plasmon-enhanced spontaneous emission in an all epitaxial material system. Samples were grown consisting of 0.5 μm ErAs/GaAs superlattice with period spacing of 5 nm and 10 nm for the 0.25 ML and 0.5 ML ErAs depositions respectively. The reduced number of periods for the higher ErAs deposition was

to maintain constant total ErAs deposition. The transmission through the samples is shown in Fig. 5.1. The samples were grown at low temperature, 400°C, and with low deposition to generate the smallest possible particles, so as to blue shift the absorption wavelength. The blue shift of the absorption wavelength is required due to the lack of small bandgap materials that can be grown on the GaAs substrate.

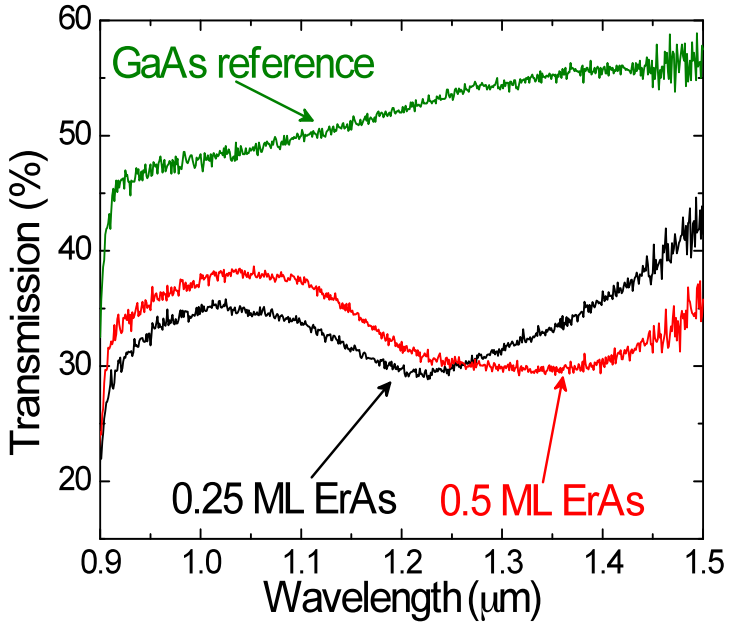

Figure 5.1: Transmission spectra for ErAs nanoparticle superlattice samples of varying ErAs deposition.

Excess compressive strain limits the emission wavelength that is reliably achievable for GaInAs QW with GaAs barriers to a room temperature peak PL wavelength of $\sim$1.15 μm. The PL spectrum for the InGaAs quantum well

is overlaid on the transmission spectrum of the 0.25 ML ErAs nanoparticle superlattice.

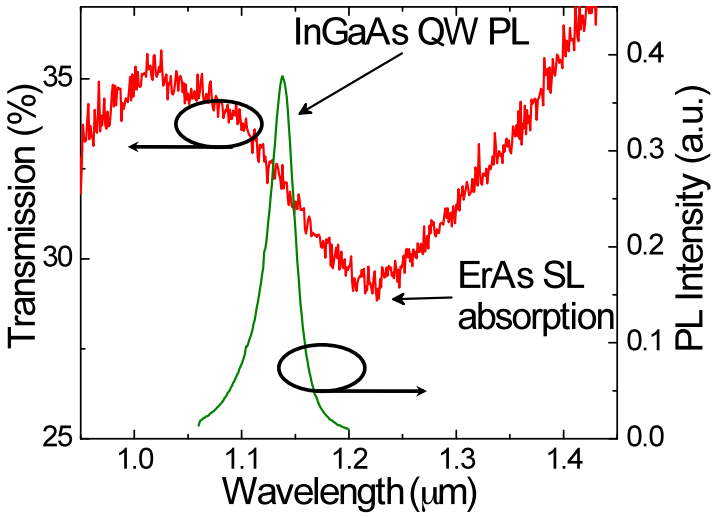

Figure 5.2: The transmission spectra of the 0.25 ML ErAs nanoparticle superlattice with PL spectrum for GaInAs quantum well photoluminescence structure overlaid.

Because the dispersion of the surface plasmon modes results in significantly enhanced photonic density of states, the radiative recombination rate is expected to be enhanced. The enhancement is given by the Purcell factor [69, 135–137]:

$$F_P = \frac{3}{4\pi^2}\left(\frac{\lambda_c}{n}\right)^3\left(\frac{Q}{V}\right), \tag{5.1}$$

where λ_c/n is the wavelength of the light in the material, Q is the quality factor and V is the mode volume of the optical cavity. It is clear that the small mode volume of the surface plasmon modes should lead to enhanced

spontaneous emission rates as well as shift in the peak PL wavelength to align with the high density of optical modes at the resonance wavelength.

Figure 5.3 plots the emission PL spectra for samples grown with and without ErAs nanoparticle grown 20 nm above the InGaAs quantum well. The ErAs was grown after the quantum well active region so the erbium cell could remain cool during the growth of the optically active region. After the quantum well was overgrown with GaAs barrier, the structure was As capped and moved into the buffer chamber. The erbium cell was then heated to the growth

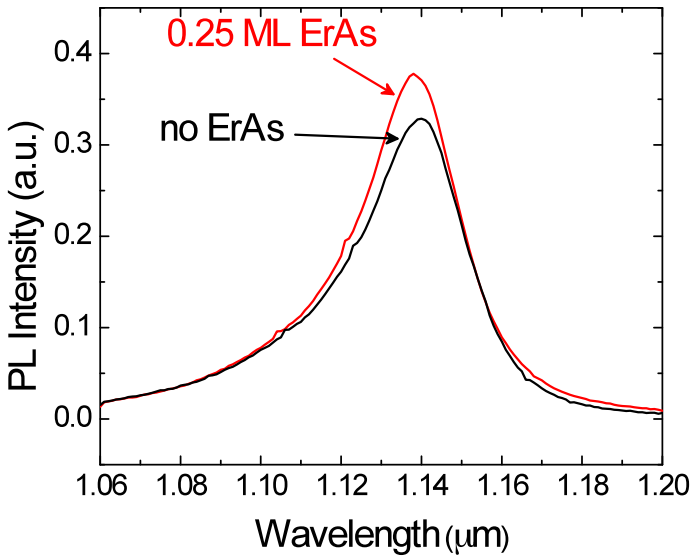

Figure 5.3: Photoluminescence spectra of PL structures growth with and without ErAs nanoparticle layers. The absorption feature of the ErAs nanoparticles is spectrally aligned to the PL emission peak, shown in Fig. 5.2, however there is nealy no difference in PL intensity and no observable shift in the emission wavelength, as would be expected for Purcell enhancement of spontaneous emission.

temperature prior to reloading the PL sample into the chamber and depositing the 0.25 ML ErAs nanoparticle layer. Several samples were grown with varying separation between the nanoparticle layer and the InGaAs quantum well, however there was no observable trend in the PL spectrum. All of the samples, displayed similar PL intensity, and no shift between sample with ErAs nanoparticle and those without was observed.

The absence of change in the emission properties of quantum wells, spectrally aligned to the ErAs absorption resonance, brought into close proximity to the ErAs nanoparticles suggests that plasmonic absorption may not be the origin of the absorption feature. Further information about the optical properties of the ErAs material is required to determine if the near-IR absorption feature is not in fact due to surface plasmon resonances.

5.2 Optical Properties of ErAs Films

There have been several reports in the literature ascribing absorption properties of RE-V nanoparticles as either band-to-band transitions [71] or as surface plasmon resonance [18, 70]. Absorption measurements on superlattices of ErAs nanoparticles exhibit absorption that shifts with particle size in the direction expected for surface plasmon resonance [138]. Additionally, the absorption spectrum changes little with temperature, consistent with plasmonic absorption. However, when a quantum well emission wavelength was spectrally aligned to the absorption resonance in the ErAs nanoparticles, no enhancement in emission was observed. In order to understand the lack of

plasmon enhancement, bulk properties of the ErAs films must be known. To measure bulk optical properties, a 500 nm ErAs film was grown at 450°C with an ErAs growth rate of 0.35 ML/s. The film was capped with 10 nm of GaAs to prevent oxidation. Figure 5.4 shows the reflectivity (a) and the transmission (b) of the ErAs film. Fitting the reflectivity and absorption to a Drude-Lorentz model with *RefFIT*[1] extracts the complex dielectric constant shown in Figure 5.5.

$$\epsilon_r^{'}(\omega) = 1 - \frac{\omega_p^2}{\omega^2 + \Gamma^2}\,, \tag{5.2}$$

and

$$\epsilon_r^{''}(\omega) = \omega_p^2 \frac{\Gamma}{\omega(\omega^2 + \Gamma^2)}\,, \tag{5.3}$$

where

$$\omega_p = \sqrt{\frac{N\,e^2}{m^*\,\epsilon_0}}\,, \tag{5.4}$$

The bulk properties of the ErAs, particularly the plasma resonance wavelength, $\lambda_p \sim 3\,\mu$m, indicates that the near-IR absorption of the ErAs nanoparticles is likely not attributable to surface plasmon resonance. In order to shift the plasma frequency for the particles to below the $1.2\,\mu$m absorption feature would require additional free carriers to be supplied by the particle surface. While the amount of charge required to shift the plasma resonance is well below the dangling bonds at the particle surface, the size of the particles with respect to the absorption wavelength also suggests that plasmon resonance is not the origin of the absorption feature. However, the magnitude of the real

[1] *RefFIT* is a fitting software package specifically designed for optical spectrum of solids.

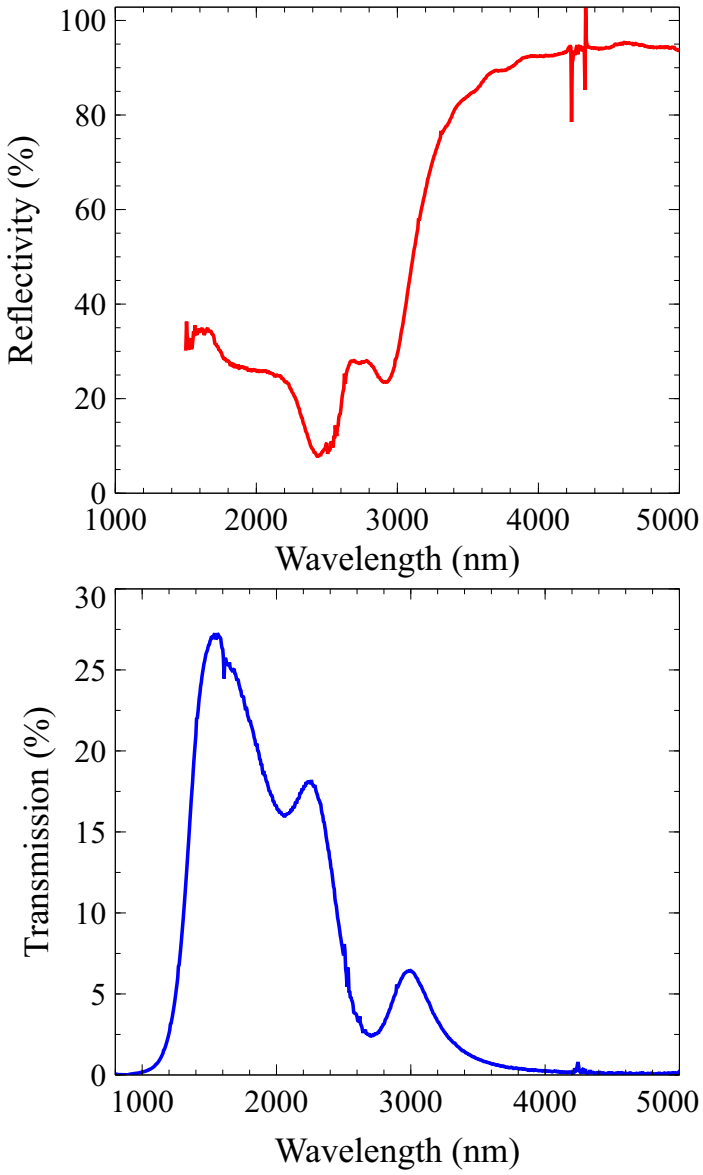

Figure 5.4: (a) Reflectivity of 500 nm ErAs film. The Drude edge appears around 3000 nm. (b) Transmission through 500 nm ErAs film. The two absorption peaks near 2200 and 2800 nm are attributed to band-to-band transitions away from zone center.

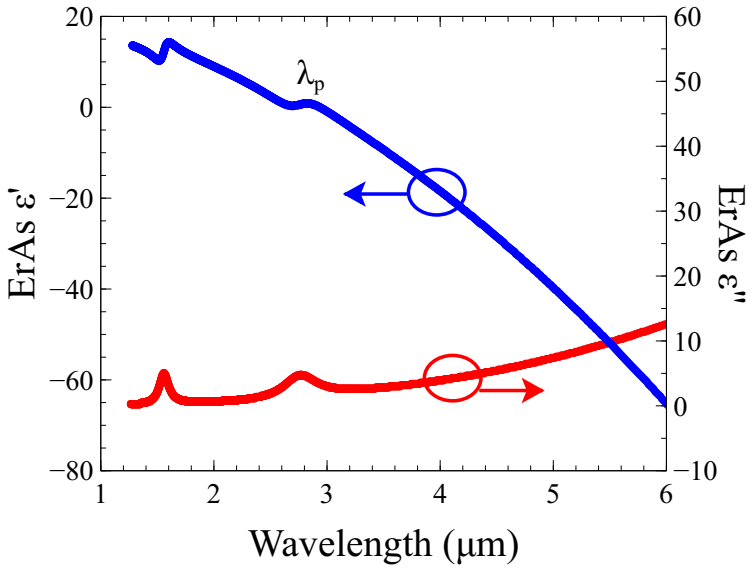

Figure 5.5: Real, $\epsilon^{'}$, and imaginary, $\epsilon^{''}$, parts of dielectric constant extracted using *RefFIT* from the transmission and reflection data of 500 nm ErAs film (Fig. 5.4). The plasma frequency, λ_p, is apparent where $\epsilon^{'}$ crosses zero.

and imaginary parts of the permitivity (Fig. 5.5) suggest that ErAs could be a promising material for plasmon-enhanced devices in the mid-IR, wavelengths that are readily accessible with intraband transitions.

5.3 Conclusions

ErAs nanoparticles exhibit absorption features in the near-infrared that are likely band transitions between conduction and valence bands away from zone center. The bulk plasma properties of ErAs films and the size of the ErAs nanostructures suggest that epitaxially embedding ErAs nanostructures for plasmonic structures will be prohibitive for current growth methods. However, ErAs films show ϵ' and ϵ" comparible to Au for wavelengths in the mid-IR making it a potential material system to investigate epitaxial plasmonics.

Chapter 6

ErAs Film Growth

Successful incorporation of RE-V nanostructures with III-V materials has resulted in epitaxially embeddable, semimetal/semiconductor heterostructures. The unique properties of nanostructures and composites enhance performance of several categories of semiconductor devices. The quality of the devices containing ErAs nanostructures, in particular the optical quality of the III-V overgrowth, is possible because of the low defect density in the III-V overgrowth of ErAs nanostructures. The RE-V can be embedded in the III-V materials, without the formation of defects, due to the ability to overcome the mismatch in rotational symmetry by seeding the overgrowth with exposed III-V layer [29]. The embedded growth mode of ErAs nanoparticles [30] and the preferential incorporation of surface erbium into subsurface ErAs nanoparticles [46] offer the possibility to overcome the mismatch in rotational symmetry that had previously prevented integration of full films [75]. In addition to the electrical applications that could benefit from epitaxially integrated metals (i.e. embedded Ohmic contacts, high-conductivity spreading layers, back gating etc.), an epitaxial metal/semiconductor heterostructure could offer new paradigms for optical devices based on surface plasmons.

6.1 Nanoparticle-Seeded Film Growth Method

A primary challenge to integrate rocksalt RE-V materials with zinc blende III-V materials is the 90 deg rotational symmetry of the rocksalt crystal structure compared to the 180 deg rotational symmetry of zinc blende crystal structure. Figure 6.1 illustrates the atomic structure of the (100) growth surface of (a) ErAs and (b) GaAs. In the overgrowth of full films of ErAs

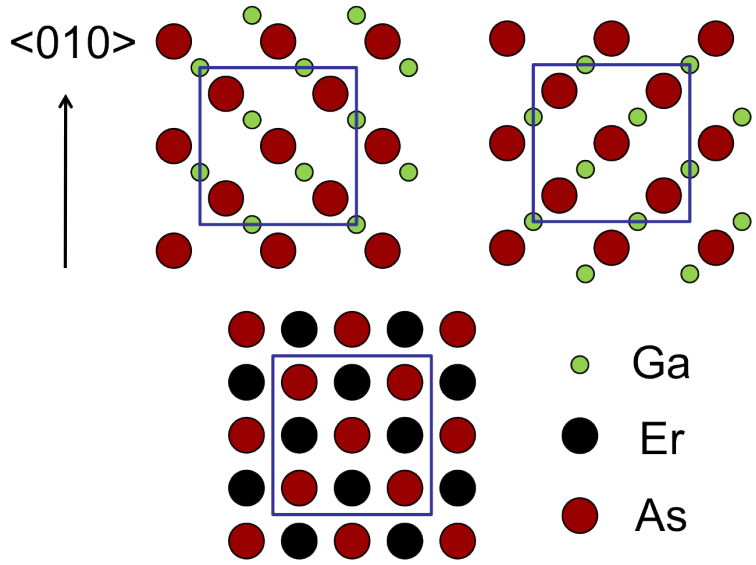

Figure 6.1: Illustration of the atomic structure of the (100) surface. (a) two unique phases of GaAs surface. (b) ErAs surface

with GaAs, the islands with the two unique phases of GaAs seed resulting in antiphase domains when the islands grow together [139]. Additionally, the GaAs grows in the Volmer-Weber growth mode [140] due to the mismatch in surface energy of GaAs and ErAs. When the islands coalesce together forming a continuous film, stacking faults form at the island boundaries [141].

These challenges are overcome by seeding ErAs film growth with nanoparticles that are overgrown with the conventional method. Figure 6.2 illustrates the nanoparticle-seeded growth method. Growth begins with embedding an ErAs nanoparticle seed layer in GaAs and overgrowing with a thin GaAs spacer layer of thickness t_{sp}. The sample is then heated to 600°C to enhance erbium diffusion and the erbium flux is reinitiated to grow the buried ErAs nanoparticles into a full film. Because of the low erbium flux, surface erbium diffuses through the GaAs spacer and preferentially incorporates at the subsurface nanoparticles without building up sufficient surface concentration to nucleate ErAs nanoparticles on the GaAs surface. The underlying nanoparticles expand laterally until they coalesce into a film. Because the film is grown through a thin GaAs spacer that was seeded by the substrate, the zinc blende symmetry is maintained and subsequent GaAs overgrowth is single-phase.

To investigate the effects of spacer thickness on the nanoparticle-seeded film growth method as well as to demonstrate the potential to suppress planar defects in the GaAs overgrowth of ErAs films, a sample with varying spacer thickness was grown for TEM imaging. The sample structure consisted of five ErAs films, each with 5 ML total ErAs deposition, embedded in GaAs. Growth conditions were chosen to be consistent with the demonstration of surface erbium incorporating into subsurface ErAs nanoparticles.[46] The ErAs nanoparticle seed layer consisted of 1.33 ML of ErAs, grown at 530°C with an ErAs growth rate of 0.05 ML/s (corresponding to an erbium cell temperature of ∼1005°C). The nanoparticles were capped with a GaAs spacer in the manner

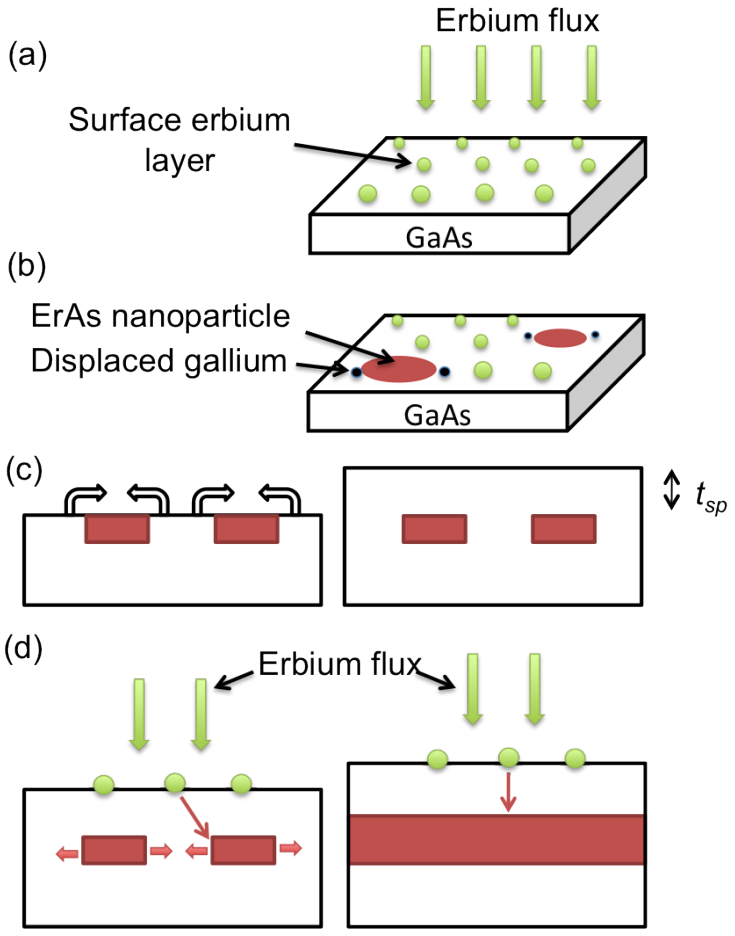

Figure 6.2: Illustration of the nanoparticle-seeded film growth method. (a) At the initation of an erbium flux, erbium accumulates at the GaAs surface. (b) Beyond the critical areal density for nanoparticle formation, ErAs nanoparticles precipitate out. The nanoparticles are embedded at the surface and have characteristic size of ∼4 ML. (c) The nanoparticles are overgrown with a thin GaAs spacer layer that is seeded by the exposed substrate. (d) ErAs film growth persists by diffusion of erbium adatoms to the nanoparticle seed layer which expands laterally until a full film is formed. The GaAs spacer layer serves as a template for single phase III-V overgrowth.

described in Chapter 2. Subsequent ErAs was grown with the erbium cell cooled to 920°C, to produce a flux of $\sim$8x10^{12} cm^{-2}s^{-1} (0.0125 ML/s effective growth rate). The GaAs spacer thickness was progressively increased from 1−3 nm, which is a range that was expected to be favorable for erbium diffusion to the subsurface ErAs. The top film was grown without a GaAs spacer layer, corresponding to the conventional layer-by-layer growth method. A 100 nm GaAs layer was grown after each ErAs film to ensure a smooth starting surface for the subsequent ErAs film.

A TEM image of the sample is shown in Fig. 6.3. The GaAs spacer

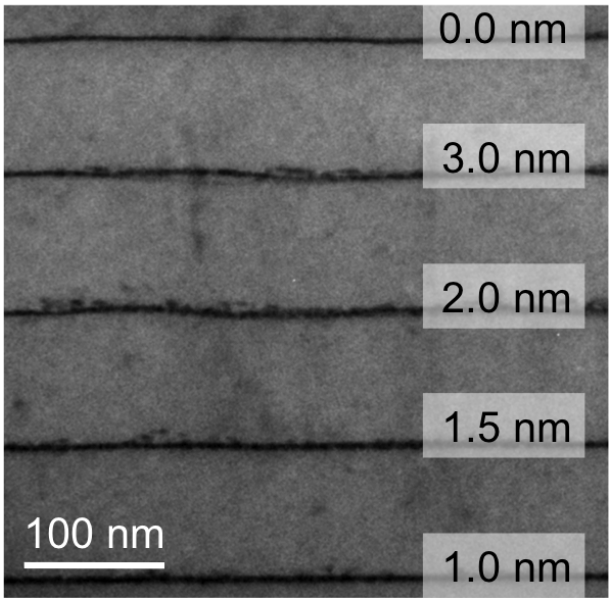

Figure 6.3: Cross-section TEM of multi-layer structure consisting of ErAs films with successively thicker GaAs spacer. The GaAs spacer thickness is overlaid on the film. The top layer has no GaAs spacer, which represents the conventional layer-by-layer growth method.

thickness (t_{sp}) is overlaid on each ErAs layer. The surface was monitored in situ with reflection high-energy electron diffraction (RHEED). A streaky GaAs 2 x 4 reconstruction was observed prior to the growth of each ErAs layer. Degradation of the GaAs overgrowth was only observed for the final ErAs film that was grown with a 0 nm spacer (i.e. the conventional growth method).

High resolution (HR) TEM images of the top film, corresponding to conventional layer-by-layer growth, and the bottom film, grown through a 1 nm GaAs spacer, are shown in Fig 6.4. The GaAs overgrowth of the conventionally grown film (Fig. 6.4a) clearly shows planar defects, consistent with twinning and antiphase domains, that are expected to form during the overgrowth of the rocksalt ErAs with the zinc blende GaAs [17]. By contrast, as shown in Fig. 6.4b, the GaAs overgrowth of the nanoparticle-seeded film, grown through a 1 nm GaAs spacer, exhibited no such planar defects. This corresponds to over twice the total erbium deposition that can be grown by the conventional method without the degradation in the GaAs overgrowth [121], validating the new growth physics. Careful inspection of the nanoparticle-seeded film indicated a modest increase in roughness and decrease in homogeneity of the ErAs film, as compared to those grown by the conventional method.

The HR-TEM images of the films grown with thicker GaAs spacer layers reveal the importance of the capping layer thickness in the nanoparticle-seeded growth method. The GaAs spacer thickness must be carefully chosen to be thin enough to sink the Er efficiently, but thick enough that it maintains a sufficiently continuous GaAs film to prevent planar defect for-

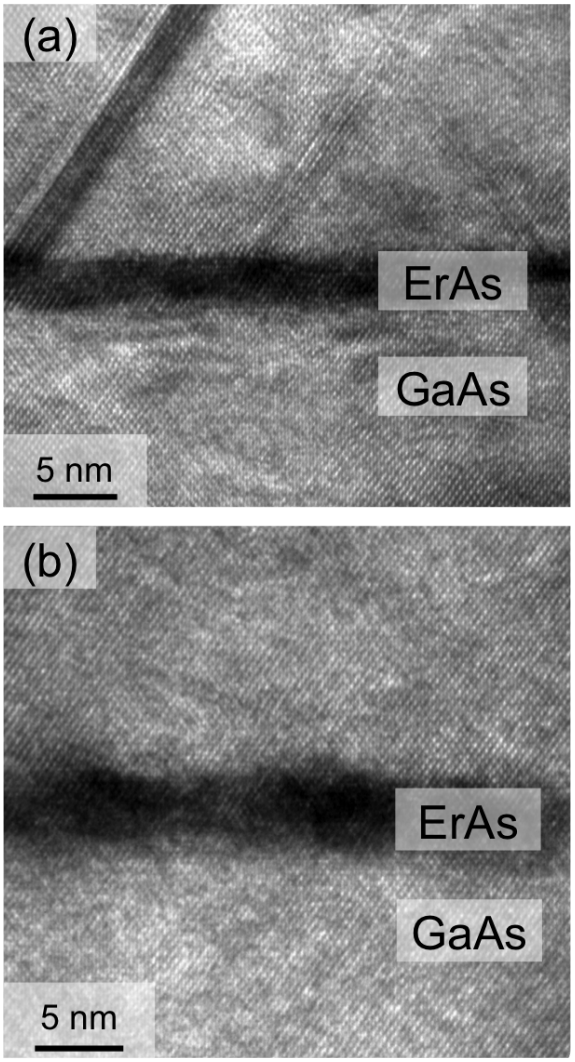

Figure 6.4: High-resolution TEM of (a) 5 ML ErAs film grown with the conventional (0 nm spacer thickness) and (b) 5 ML ErAs film growth with the nanoparticle-seeded film growth method (1 nm spacer thickness). The conventionally grown film clearly exhibits planar defects in the GaAs overgrowth while such defects are suppressed in the nanoparticle-seeded ErAs film.

mation. With increasing GaAs spacer thickness, we observed the appearance of a second nanoparticle layer and decreasing uniformity of the "film" grown at the nanoparticle seed layer. Figure 6.5 shows the HR-TEM image for the

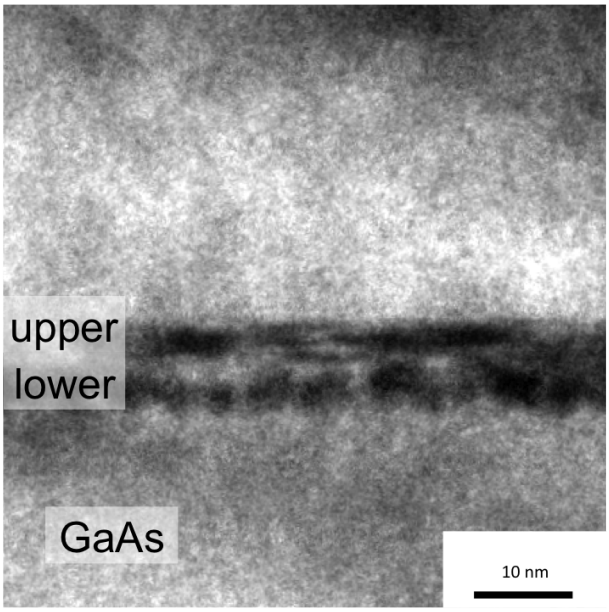

Figure 6.5: High-resolution TEM image of the nanoparticle-seeded ErAs layer grown with 3.0 nm GaAs spacer. The two distinct nanoparticle layers (denoted lower & upper) correspond to the nanoparticle seed layer (lower) and the parasitic surface nanoparticle layer (upper).

nanoparticle-seeded film grown with a 3 nm GaAs spacer. It is clear that the nanoparticle-seed layer (denoted lower) has not coalesced into a film prior to the formation of a second ErAs nanoparticle layer on the surface of the GaAs spacer (denoted upper). It is important to note, however, that the total erbium deposition at the surface during the film growth was 3.67 ML. This is more than the ∼2 ML of ErAs nanoparticles that can be overgrown at the elevated

growth temperature, without resulting in highly defective GaAs overgrowth. This implies that some of the erbium diffused to the nanoparticle-seed layer to incorporate prior to the formation of the surface nanoparticle layer. Additionally, in each of the ErAs films grown with > 1.0 nm GaAs spacers, we observed two distinct nanoparticle layers. It is important to note that we did not observe pillars, or similar features, that connected the nanoparticle-seed layers to the surface, which one might expect if the nanoparticles had a tendency to expand vertically. This is particularly promising for the future development of the film growth technique as it implies that it is favorable for the subsurface nanoparticles to expand laterally, resulting in a quasi-layer-by-layer growth mechanism.

To investigate the early stages of this nanoparticle-seeded film growth, we grew a multi-layer structure consisting of 10 layers of ErAs. Each layer was overgrown with 50 nm of GaAs and reflection high-energy electron diffraction was monitored to insure a smooth starting surface. The first layer consisted of only a 1.33 ML ErAs nanoparticle seed layer, with each additional ErAs layer containing an extra 0.5 ML of ErAs. Cross-section transmission electron microscope (TEM) images of the sample are shown in Fig. 6.6. The vertical extent of the nanoparticle seed layer and the ErAs films is larger than expected. This can be attributed to a thick TEM foil ($\sim$100 nm) and finite GaAs surface roughness at the initiation of the ErAs nanoparticle seed layer. It should be noted that the large vertical extent of the nanoparticle seed layer could mask a tendency of the ErAs nanoparticles to expand vertically during film growth.

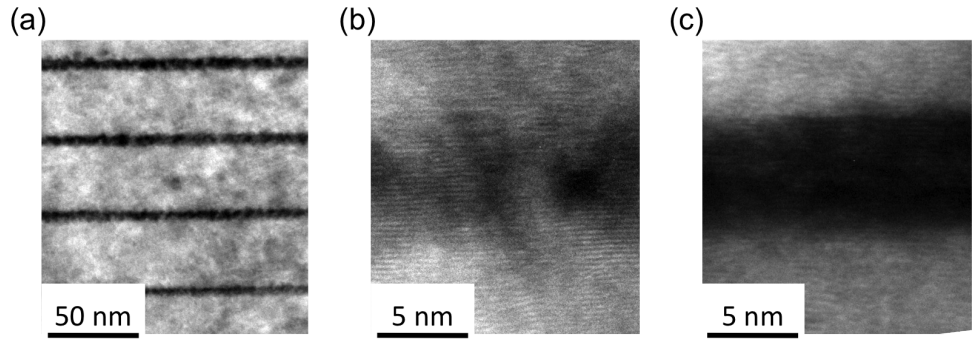

Figure 6.6: Cross-section TEM of multi-layer structure consisting of ErAs films with successively higher ErAs depositions. (a) bottom 4 layers consisting of 1.33 ML ErAs nanoparticle seed layer, 1.83 ML, 2.33 ML, and 2.83 ML from bottom to top. (b) High-resolution TEM of nanoparticle seed layer. (c) High-resolution TEM of 5.33 ML ErAs film. The vertical extent of the nanoparticle-seeded films appears to be constant with much less roughness for the full films than the nanoparticle seed layer.

6.2 Optical Investigation of ErAs Film Overgrowth

Cross-sectional TEM is great for comparing samples with high defect density, such as the overgrowth of conventional ErAs films. However, as defect density is reduced, the amount of TEM required to image defects gets prohibitively large. Even without defect density sufficient to image in TEM, device quality in the overgrowth of nanoparticle-seeded ErAs films could be degraded. Optical measurements of photoluminescence structures grown above ErAs films allows us to be sensitive to defect densities far lower than the detection limit in cross-sectional TEM. Unfortunately, unlike TEM, only a

single ErAs film can be measured per PL structure. Additionally, care must be taken to mitigate parasitic erbium incorporation potentially influencing the film growth method.

Several samples were grown with and without ErAs films for optical characterization. Similar to Chapter 4, the PL structure consisted of 10 nm InGaAs quantum well (emission wavelength of 960 nm), embedded in 200 nm GaAs absorbing region, surrounded on each side by AlAs diffusion blocking layers. The PL structure is illustrated in Fig. 4.1 and band diagram plotted in Fig. 4.2. For samples grown with ErAs films, care must be taken to insure no parasitic erbium flux is present during the growth of the PL structure and that the surface erbium concentration is low prior to growth of the PL structure. Analogous to the high optical-quality overgrowth of ErAs nanoparticle (presented in Chapter 4), the sample was held at thermal deoxidation temperature with a thin GaAs spacer above the ErAs film while the erbium cell was cooled to idle temperature. Figure 6.7 plots the PL spectra for a control sample, a 5 ML ErAs film grown with the conventional layer-by-layer method, and a 5 ML ErAs film grown with the nanoparticle-seeded film growth method. The control sample has no ErAs layer and was grown with the erbium cell idle throughout the entire growth. Both ErAs films utilized the ErAs film to sink surface erbium while cooling the erbium cell.

While the nanoparticle-seeded film growth method has succeeded in reducing the defect density to sufficiently to yield room-temperature PL signal, there is still a factor of $\sim$10 reduction in the PL intensity compared to the

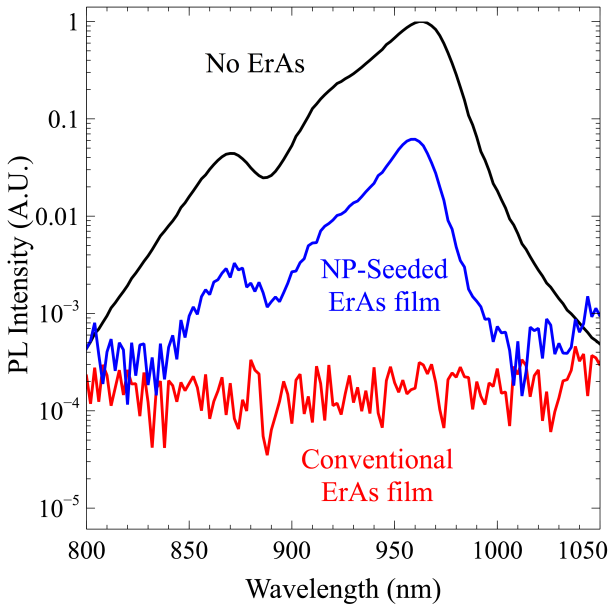

Figure 6.7: Photoluminescence spectra for ErAs-free control sample, conventionally grown ErAs film, and nanoparticle-seeded ErAs film. While the conventional ErAs film does not show any PL yield above the noise floor, the nanoparticle-seeded ErAs film exhibits only $\sim$10$\times$ degradation in the peak PL intensity.

ErAs-free sample. Because measurement of the optical quality required the management of parasitic erbium doping, the ErAs film had an additional high temperature anneal step required during the cooling of the erbium cell. One would like to distinguish if the degradation in the optical quality is intrinsic to defects formed in the overgrowth of the nanoparticle-seeded film or if the additional annealing step was the source of additional defect generation.

In order to test the origin of the degradation of optical quality, a sample employing an ErAs nanoparticle layer to sink the surface erbium was grown. This sample consisted of a 5 ML ErAs film, a 50 nm GaAs spacer, 1.33 ML ErAs nanoparticle layer, and a PL structure. The ErAs film was immediately overgrown, similar to the samples grown for TEM analysis, while the 1.33 ML ErAs nanoparticle layer was overgrown with 1 nm of GaAs and utilized to sink parasitic erbium similar to the optical quality experiments of Chap. 4. The PL spectra for the samples with the nanoparticle layer and that without were nearly identical indicating that the degradation in the optical quality is intrinsic to incorporating the ErAs film. Even so, the PL signal is $\sim$100$\times$ stronger than samples with $10^{15}\,\mathrm{cm}^{-3}$ parasitic erbium doping and would be sufficient quality for several electrical devices. Additionally, the PL measurement gives a high sensitivity to defect formation that can be used to refine the growth method and improve the overgrowth quality.

6.3 Conductivity of Erbium Arsenide Films

With the new ability to grow full films of ErAs embedded in III-V semiconductors with fewer planar defects in the III-V overgrowth, the electrical conductivity of these films is of particular interest. Previous work on ErAs nanoparticle layers consisting of < 2 ML of ErAs showed thermally activated conductivity consistent with hopping transport [142]. Increasing the ErAs deposition to > 3 ML resulted in a transition to metallic band-like transport, where the conductivity decreases at elevated temperatures. However, the highly defective GaAs overgrowth prevented the incorporation of these films into devices. The hopping transport regime is characterized by conductivity (σ) below $10^1\,\Omega^{-1}\text{cm}^{-1}$, while the band-like transport regime is characterized by $\sigma > 10^2\,\Omega^{-1}\text{cm}^{-1}$ with bulk ErAs exhibiting $\sigma{\sim}10^4\,\Omega^{-1}\text{cm}^{-1}$.

Single films of varying thickness of ErAs were grown by the nanoparticle-seeded film growth method and capped with 10 nm of GaAs. Samples were processed into transmission line method (TLM) structures by diffusing Ni/Au contacts through the GaAs layer [143] to electrically contact the ErAs films, illustrated in Fig. 6.8.

A representative resistance vs spacing measurement for a 10 ML nanoparticle-seeded ErAs film is shown in Fig. 6.9. Each of the separations showed linear I-V response. The specific contact resistivity for the 10 ML film was $7.5\,\Omega\text{cm}^2$.

The sheet resistance, extracted from the TLM measurements, and cor-

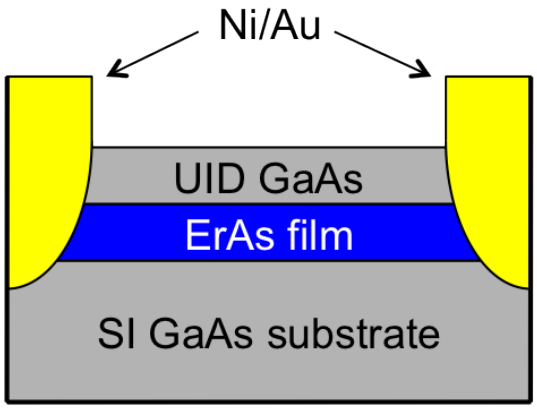

Figure 6.8: Illustration of the sample structure and contact scheme for TLM structures to measure the electrical conductivity of the ErAs films.

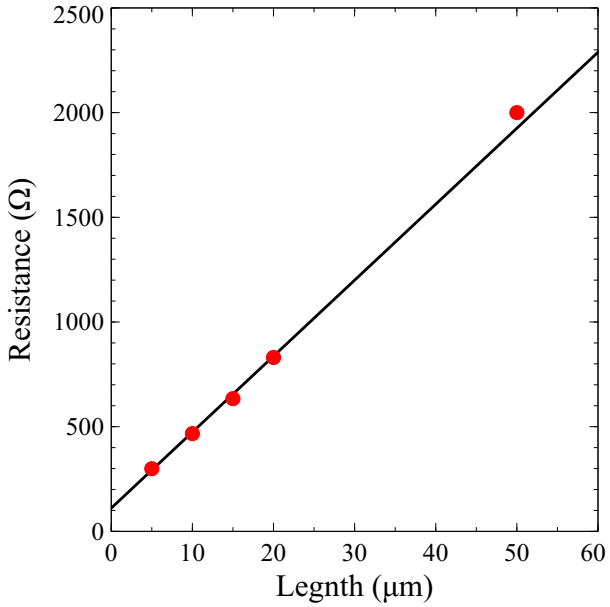

Figure 6.9: Resistance vs Length for 10 ML ErAs film grown with nanoparticle-seeded film growth method.

responding conductivity are plotted in Fig. 6.10. Because the films were grown

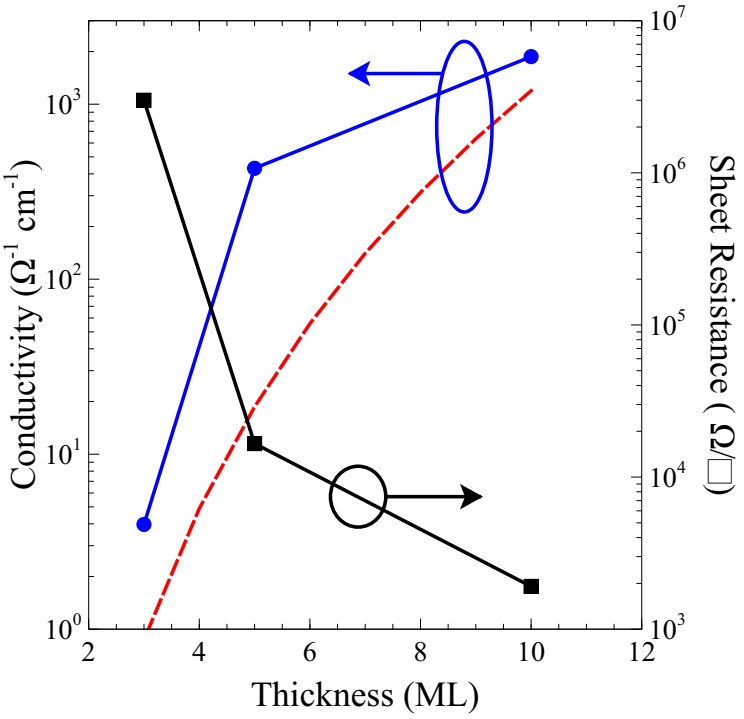

Figure 6.10: Sheet resistance and corresponding conductivity of ErAs films grown with the nanoparticle-seeded film growth technique. The dashed line is the calculated conductivity for surface roughness scattering limited transport with roughness characterized by the nanoparticle seed layer.

with a nanoparticle seed layer, the interface roughness is of particular interest. The red line corresponds to the calculated surface roughness limited conductivity [144] of ErAs films assuming the nanoparticle seed layer determines the surface roughness. We assume Gaussian roughness, giving a scattering matrix

element, M_R:

$$M_R^2 = \frac{\pi^5 \hbar^4 \Delta^2 \Lambda^2}{m^{*2} L_w^6} \exp\left(-\frac{\Lambda^2 q^2}{4}\right), \tag{6.1}$$

where Δ and Λ the characteristic height and length of the surface roughness. The surface roughness-limited mobility is then given by:

$$\mu_R = \frac{e}{m^*} < \tau_R > \propto \frac{L_w^6}{\Delta^2 \Lambda^2}, \tag{6.2}$$

where L_w is the width of the ErAs layer, m^* is the effective mass, and τ_R is the momentum scattering rate which is calculated using Fermi's Golden Rule.

The conductivity of the ErAs films of varying thickness, as well as the calculated conductivity for interface roughness-limited conductivity, are plotted in Fig 6.10. The μ_R is calculated with Δ and Λ set to 3 ML and 10 nm respectively. These values are characteristic of the nanoparticles seed layer. The conductivity reveals important details about the film properties. In particular, the measured conductivity of each ErAs film is higher than the calculated surface roughness limited conductivity for the corresponding thickness. This implies that the actual interface roughness of the films is smoother than the nanoparticle seed layer, which is consistent with a lateral growth mode for the nanoparticle-seeded film growth method. Additionally, the magnitude of the conductivity of the 5 ML film is well into the band-like transport regime, consistent with the nanoparticle seed layer having coalesced into a continuous film. The band-like transport is confirmed with temperature dependent conductivity measurements, shown in Fig. 6.11. The positive temperature

coefficient is indicative of a semimetallic film, consistent with the observations for bulk ErAs [16].

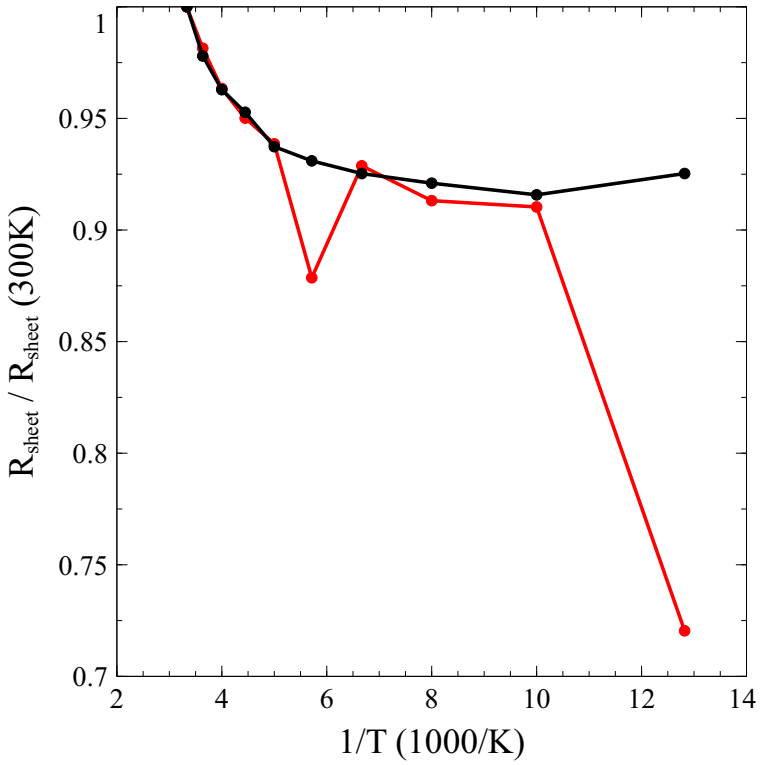

Figure 6.11: Temperature dependence of resistivity of 5 ML and 10 ML ErAs films grown with the nanoparticle-seeded film growth method. The resistivity is normalized to the room temperature conductivity.

The 5 ML film thickness is the same thickness that did not display planar defects in the GaAs overgrowth [75]. However, thicker films grown with the nanoparticle seeded film growth method $>$ 10 ML exhibited planar defects indicating a failure mechanism to the film growth technique. In order to realize optically thick films or films useful as spreading layers for electronic

devices, we must identify and correct the failure mechanism.

6.4 Erbium Incorporation Model

The nanoparticle-seeded growth method has a sufficiently large parameter space that fully optimizing the growth space via design of experiments is challenging. Therefore, it is important to have a simple model for the erbium incorporation that can qualitatively and quantitatively describe the erbium incorporation. Because there are no volatile Er_xAs_y compounds at normal III-V growth conditions and the erbium vapor pressure at the growth temperature is negligible, we can use a simple diffusion model where the only source of erbium is the flux from the erbium cell and the only sink of erbium at the nanoparticle seed layer. In this case the erbium continuity equation becomes:

$$\frac{\delta n_{Er}}{\delta t} = \bigtriangledown \cdot (n_{Er} v) = \bigtriangledown \cdot \Phi_{Er} \,, \tag{6.3}$$

where Φ_{Er} is the erbium flux, n_{Er} is the erbium density, and v is the average velocity of erbium. Because we are concerned with the steady state growth conditions where:

$$\frac{\delta n_{Er}}{\delta t} = 0 \,, \tag{6.4}$$

and the erbium flux is set by the cell temperature ($\Phi_{Er} = 8{\times}10^{12}\,\mathrm{cm^{-2}\,s^{-1}}$), we arrive at:

$$\Phi_{Er} = -D_{Er}\,\frac{\delta n_{Er}(x)}{\delta x} = \frac{D_{Er} n_0}{L} \,, \tag{6.5}$$

where D_{Er} is assumed to be constant, n_0 is the surface concentration of erbium, and L is the GaAs spacer thickness. The resulting erbium concentration pro-

files depend linearly on L. Figure 6.12 shows calculated erbium concentration profiles varying the erbium flux (Fig. 6.12a) and the GaAs spacer thickness (Fig. 6.12b). One of the critical parameters is the surface erbium concentra-

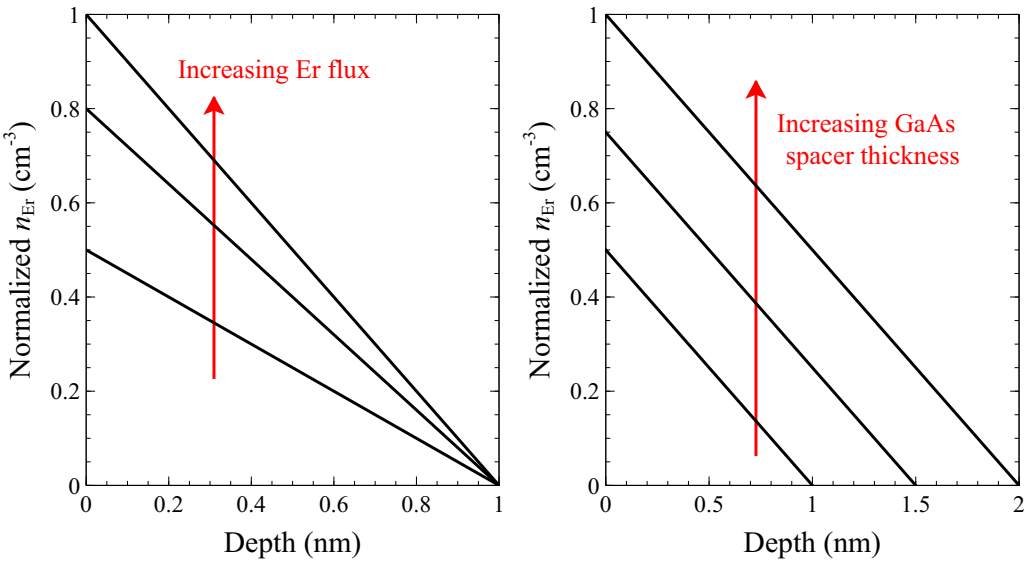

Figure 6.12: Calculated erbium concentration profiles for varying nanoparticle-seeded film growth conditions. (a) Varying erbium flux with constant GaAs spacer thickness. (b) Varying GaAs spacer thickness with constant erbium flux. The x-intercept corresponds to the location of the nanoparticles and the y-intercept corresponds to the surface concentration of erbium.

tion. Because ErAs nanoparticle formation only occurs at a critical erbium surface areal density, [46] the erbium flux and nanoparticle seed layer must be chosen such that the steady state erbium surface concentration, n_0, is below the critical density for nanoparticle formation (n_c). If n_0 exceeds n_c, a surface nanoparticle layer will form, and subsequent ErAs growth will persist at the

surface resulting in formation of planar defects in GaAs overgrowth. The formation of a second nanoparticle layer has been observed for 5 ML ErAs films grown with 3 nm GaAs spacer layer [75].

A second concern with the growth method is what happens to the displaced Ga atoms when the Er incorporates at the subsurface ErAs layer. Previous X-ray photoemission spectroscopy analysis during conventional ErAs film growth found that as erbium incorporates it displaces Ga which then reincorporates at the GaAs surface [30]. With subsequent ErAs growth this process continues, however, the GaAs-related signal decays with ErAs growth, indicating that some of the Ga is lost, potentially as doping in the ErAs film [30]. A similar process in the nanoparticle-seeded film growth method could decrease the GaAs spacer layer thickness as the ErAs film is grown, resulting in planar defects in the GaAs overgrowth.

The simple diffusion model suggests that slow ErAs growth rates and thin GaAs spacers are the growth regime to consider in order to realize arbitrarily thick ErAs films. However, there may be a tradeoff between thin GaAs spacer layers and loss of Ga to incorporation in the ErAs film. Further investigation is required to realize the full potential of RE-V/III-V heterostructures.

Chapter 7

Conclusion

Rare-earth pnictide materials were investigated for the enhancement of current optical devices, such as high-efficiency solar cells and long-wavelength lasers. Additionally, the RE-V materials are promising for the development of novel devices based on epitaxially embedded semimetal/semiconductor heterostructures. Tunnel junction were developed that exhibit simultaneously high electrical-conductivity and low optical-loss, are thermodynamically stable, and offer tunable electrical and optical properties based off the morphology of the RE-V nanoparticles. A new application of embedded nanoparticles was demonstrated to have potential to reduce the doping sensitivity of band-to-band tunnel junctions for optical devices. GaSb tunnel junctions employing ErSb nanoparticles were developed for low p-type doping tunnel junctions. Because of the small Schottky barrier for holes, the low p-type doping degrades tunneling current by less than a factor of 2 for a reduction in p-type doping from $2\times10^{19}\text{cm}^{-3}$ to $1\times10^{18}\text{cm}^{-3}$. If fact, the nanoparticle enhanced tunnel junction with $1\times10^{18}\text{cm}^{-3}$ shows enhancement in tunneling current over conventional junction with higher p-type doping.

The RE-V nanoparticles can be embedded at the interface of conven-

tional tunnel junctions to overcome the trade-off between electrical-conductivity and optical-loss. The integration of the RE-V nanostructures within optical devices was studied in detail. Parasitic erbium doping of layers grown with the erbium cell closed was identified as the source of degradation in optical properties. Because of the surface segregation of erbium during III-V growth, simply cooling the erbium cell after nanoparticle growth was insufficient to realize high optical quality material in close proximity to RE-V nanostructures. A method to deplete the surface of erbium that utilizes preferential erbium incorporation into subsurface ErAs nanoparticles, was used to demonstrate high-optical-quality III-V material, even in close proximity to the ErAs nanostructures. In fact, quantum wells, grown 15 nm from the ErAs nanoparticle layer, exhibit 95% of the peak PL intensity of ErAs free samples.

The observations in the optical quality experiments and the microscopic measurements of ErAs tunnel junctions required improvement in the model for ErAs nanostructure growth. Through the combination of surface segregation and an embedded growth mode connects the previous observations for erbium-doped GaAs and the ErAs nanostructure. The model lead to the development of a novel growth method that overcomes the mismatch in rotational symmetry that had previously prevented the overgrowth of full films. Initial investigation of the nanoparticle-seeded film growth method revealed the suppression of planar defects in the GaAs overgrowth of the ErAs films. Defect-free overgrowth has been observed for samples consisting of ErAs films with 2× the ErAs that can be grown defect-free with the conventional layer-by-layer growth. The

nanoparticle-seeded films exhibited high-conductivity and a negative temperature coefficient, consistent with bulk ErAs films. Further development of the growth method could lead to novel electronic and plasmonic devices based on epitaxially embedded RE-V/III-V heterostructures.

Several extensions of this work are currently in progress. The incorporation of the lightly doped tunnel junctions along with the dilute-nitride active regions into mid-IR diode lasers is currently being pursued. Extension of the emission wavelength beyond 4 μm is likely required to show much improvement in laser performance associated with the nanoparticle-enhanced tunnel junction. Additionally, extension of the nanoparticle-seeded film growth method to the ErSb/GaSb material system could prove beneficial. The GaSb overgrowth of ErSb films does not suffer from the islanding growth mode that plagues the GaAs overgrowth of ErAs films. As such, the only source of planar defects in this material system will be the rotational symmetry. Also, this material system is nearly lattice matched and the plasmon frequency of the ErSb layers is accessible by band-to-band transitions in the lattice-matched alloys available on the 6.1 $\AA$ material family.

Bibliography

[1] J. M. O. Zide, A. Kleiman-Shwarsctein, N. C. Strandwitz, J. D. Zimmerman, T. Steenblock-Smith, A. C. Gossard, A. Forman, A. Ivanovskaya, and G. D. Stucky, "Increased efficiency in multijunction solar cells through the incorporation of semimetallic ErAs nanoparticles into the tunnel junction," *Appl. Phys. Lett.* **88** no. 16, (2006) 162103.

[2] K. C. R. Chiu, J. M. Poate, L. C. Feldman, and C. J. Doherty, "Interfacial order in epitaxial $NiSi_2$," *Appl. Phys. Lett.* **36** no. 7, (1980) 544–547.

[3] S. C. Wu, Y. S. Li, F. Jona, and P. M. Marcus, "Epitaxy of silicon on nickel silicide," *Phys. Rev. B* **32** no. 10, (Nov, 1985) 6956–6958.

[4] J. Y. Veuillen, C. d Anterroches, and T. A. N. Tan, "Growth of silicon thin films on erbium silicide by solid phase epitaxy," *J. Appl. Phys.* **75** no. 1, (1994) 223–226.

[5] J. C. Bean and J. M. Poate, "Silicon/metal silicide heterostructures grown by molecular beam epitaxy," *Appl. Phys. Lett.* **37** no. 7, (1980) 643–646.

[6] R. T. Tung, J. M. Gibson, and J. M. Poate, "Formation of ultrathin single-crystal silicide films on Si: Surface and interfacial stabilization of Si-NiSi_2 epitaxial structures," *Phys. Rev. Lett.* **50** no. 6, (Feb, 1983) 429–432.

[7] A. Y. Cho and P. D. Dernier, "Single-crystal-aluminum schottky-barrier diodes prepared by molecular-beam epitaxy (MBE) on GaAs," *J. Appl. Phys.* **49** no. 6, (1978) 3328–3332.

[8] W. I. Wang, "The dependence of Al Schottky barrier height on surface conditions of GaAs and AlAs grown by molecular beam epitaxy," *J. Vac. Sci. Tech., B* **1** no. 3, (1983) 574–580.

[9] G. A. Prinz and J. J. Krebs, "Molecular beam epitaxial growth of single-crystal Fe films on GaAs," *Appl. Phys. Lett.* **39** no. 5, (1981) 397–399.

[10] M. W. Ruckman, J. J. Joyce, and J. H. Weaver, "Interdiffusion and reaction at the Fe/GaAs(110) interface," *Phys. Rev. B* **33** no. 10, (May, 1986) 7029–7035.

[11] T. Sands, "Stability and epitaxy of NiAl and related intermetallic films on III-V compound semiconductors," *Appl. Phys. Lett.* **52** no. 3, (1988) 197–199.

[12] T. Sands, J. P. Harbison, W. K. Chan, S. A. Schwarz, C. C. Chang, C. J. Palmstrøm, and V. G. Keramidas, "Epitaxial growth of

GaAs/NiAl/GaAs heterostructures," *Appl. Phys. Lett.* **52** no. 15, (1988) 1216–1218.

[13] C. J. Palmstrøm, "Epitaxy of dissimilar materials," *Ann. Rev. Mat. Sci.* **25** no. 1, (1995) 389–415.

[14] W. R. L. Lambrecht, B. Segall, A. G. Petukhov, R. Bogaerts, and F. Herlach, "Spin-orbit effects on the band structure and Fermi surface of ErAs and $Er_xSc_{1-x}As$," *Phys. Rev. B* **55** no. 15, (Apr, 1997) 9239–9242.

[15] C. J. Palmstrøm, K. C. Garrison, S. Mounier, T. Sands, C. L. Schwartz, N. Tabatabaie, J. S. J. Allen, H. L. Gilchrist, and P. F. Miceli, "Growth of epitaxial rare-earth arsenide/(100)GaAs and GaAs/rare-earth arsenide/(100)GaAs structures," *J. Vac. Sci. Tech., B* **7** no. 4, (1989) 747–752.

[16] C. J. Palmstrøm, T. L. Cheeks, H. L. Gilchrist, J. G. Zhu, C. B. Carter, B. J. Wilkens, and R. Martin, "Effect of orientation on the Schottky barrier height of thermodynamically stable epitaxial metal/GaAs structures," *J. Vac. Sci. Tech., A* **10** no. 4, (1992) 1946–1953.

[17] A. Guivarc'h, Y. Ballini, Y. Toudic, M. Miener, P. Auvray, B. Guenais, J. Caulet, B. L. Merdy, B. Lambert, and A. Regreny, "ErSb/GaSb(001) and GaSb/ErSb/GaSb(001) heterostructures and [ErSb,GaSb] superlattices: Molecular beam epitaxial growth and characterization," *J. Appl. Phys.* **75** no. 6, (March, 1994) 2876.

[18] M. P. Hanson, D. C. Driscoll, C. Kadow, and A. C. Gossard, "Metal/semiconductor superlattices containing semimetallic ErSb nanoparticles in GaSb," *Appl. Phys. Lett.* **84** no. 2, (Jan, 2004) 221–223.

[19] C. J. Palmstrøm, N. Tabatabaie, and J. S. J. Allen, "Epitaxial growth of ErAs on (100)GaAs," *Appl. Phys. Lett.* **53** no. 26, (1988) 2608–2610.

[20] T. Sands, C. J. Palmstrøm, J. P. Harbison, V. G. Karamidas, N. Tabatabaie, T. Cheeks, R. Ramesh, and Y. Silberberg, "Stable and epitaxial metal/III-V semiconductor heterostructures," *Mat. Sci. Rep.* **5** no. 3, (1990) 99.

[21] J. G. Zhu, C. B. Carter, C. J. Palmstrøm, and S. Mounier, "Microstructure of epitactically grown GaAs/ErAs/GaAs," *Appl. Phys. Lett.* **56** no. 14, (1990) 1323–1325.

[22] I. Poole, K. E. Singer, A. R. Peaker, and A. C. Wright, "Growth and structural characterization of molecular beam epitaxial erbium-doped GaAs," *J. Crys. Growth* **121** no. 1-2, (1992) 121–131.

[23] S. Gupta, S. Sethi, and P. K. Bhattacharya, "Picosecond carrier lifetime in erbium-doped-GaAs," *Appl. Phys. Lett.* **62** no. 10, (1993) 1128–1130.

[24] K. E. Singer, P. Rutter, A. R. Peaker, and A. C. Wright, "Self-organizing growth of erbium arsenide quantum dots and wires in

gallium arsenide by molecular beam epitaxy," *Appl. Phys. Lett.* **64** no. 6, (1994) 707–709.

[25] S. Sethi, T. Brock, P. Bhattacharya, J. Kim, S. Williamson, D. Craig, and J. Nees, "High-speed metal-semiconductor-metal photodiodes with Er-doped GaAs," *IEEE Electron Device Lett.* **16** no. 3, (Mar., 1995) 106–108.

[26] P. Rutter, K. E. Singer, and A. R. Peaker, "The incorporation of erbium into molecular beam epitaxy grown gallium arsenide," *J. Crys. Growth* **182** no. 3-4, (1997) 247 – 254.

[27] H. Yamaguchi and Y. Horikoshi, "Growth of GaAs/ErAs/GaAs structures by migration-enhanced epitaxy," *Appl. Phys. Lett.* **60** no. 19, (1992) 2341–2343.

[28] N. Jourdan, H. Yamaguchi, and Y. Horikoshi, "Dependence of ErAs clustering and Er segregation in ErAs/GaAs heterostructures on growth temperature," *Jap. J. Appl. Phys.* **32** no. Part 2, No. 12B, (1993) L1784–L1787.

[29] C. Kadow, S. B. Fleischer, J. P. Ibbetson, J. E. Bowers, A. C. Gossard, J. W. Dong, and C. J. Palmstrøm, "Self-assembled ErAs islands in GaAs: Growth and subpicosecond carrier dynamics," *Appl. Phys. Lett.* **75** no. 22, (1999) 3548–3550.

[30] B. D. Schultz and C. J. Palmstrøm, "Embedded assembly mechanism of stable metal nanocrystals on semiconductor surfaces," *Phys. Rev. B* **73** no. 24, (June, 2006) 241407.

[31] P. Pohl, F. H. Renner, M. Eckardt, A. Schwanhausser, A. Friedrich, O. Yuksekdag, S. Malzer, G. H. Dohler, P. Kiesel, D. Driscoll, M. Hanson, and A. C. Gossard, "Enhanced recombination tunneling in GaAs pn junctions containing low-temperature-grown-GaAs and ErAs layers," *Appl. Phys. Lett.* **83** no. 19, (2003) 4035–4037.

[32] S. Preu, F. H. Renner, S. Malzer, G. H. Döhler, L. J. Wang, M. Hanson, A. C. Gossard, T. L. J. Wilkinson, and E. R. Brown, "Efficient terahertz emission from ballistic transport enhanced $n{-}i{-}p{-}n{-}i{-}p$ superlattice photomixers," *Appl. Phys. Lett.* **90** no. 21, (2007) 212115.

[33] W. Kim, J. Zide, A. Gossard, D. Klenov, S. Stemmer, A. Shakouri, and A. Majumdar, "Thermal conductivity reduction and thermoelectric figure of merit increase by embedding nanoparticles in crystalline semiconductors," *Phys. Rev. Lett.* **96** no. 4, (Feb, 2006) 045901.

[34] W. Kim, S. L. Singer, A. Majumdar, D. Vashaee, Z. Bian, A. Shakouri, G. Zeng, J. E. Bowers, J. M. O. Zide, and A. C. Gossard, "Cross-plane lattice and electronic thermal conductivities of ErAs:InGaAs/InGaAlAs superlattices," *Appl. Phys. Lett.* **88** no. 24, (2006) 242107.

[35] J. M. O. Zide, J.-H. Bahk, R. Singh, M. Zebarjadi, G. Zeng, H. Lu, J. P. Feser, D. Xu, S. L. Singer, Z. X. Bian, A. Majumdar, J. E.

Bowers, A. Shakouri, and A. C. Gossard, "High efficiency semimetal/semiconductor nanocomposite thermoelectric materials," *J. Appl. Phys.* **108** no. 12, (2010) 123702.

[36] P. G. Burke, H. Lu, N. G. Rudawski, S. Stemmer, A. C. Gossard, J.-H. Bahk, and J. E. Bowers, "Electrical properties of Er-doped $In_{0.53}Ga_{0.47}As$," *J. Vac. Sci. Tech., B* **29** no. 3, (2011) 03C117.

[37] L. E. Cassels, T. E. Buehl, P. G. Burke, C. J. Palmstrøm, A. C. Gossard, G. Pernot, A. Shakouri, C. R. Haughn, M. F. Doty, and J. M. O. Zide, "Growth and characterization of TbAs:GaAs nanocomposites," *J. Vac. Sci. Tech., B* **29** no. 3, (2011) 03C114.

[38] H. Lu, P. G. Burke, A. C. Gossard, G. Zeng, A. T. Ramu, J.-H. Bahk, and J. E. Bowers, "Semimetal/semiconductor nanocomposites for thermoelectrics," *Adv. Mater.* **23** no. 20, (2011) 2377–2383.

[39] C. Kadow, A. W. Jackson, A. C. Gossard, S. Matsuura, and G. A. Blake, "Self-assembled ErAs islands in GaAs for optical-heterodyne THz generation," *Appl. Phys. Lett.* **76** no. 24, (2000) 3510–3512.

[40] J. E. Bjarnason, T. L. J. Chan, A. W. M. Lee, E. R. Brown, D. C. Driscoll, M. Hanson, A. C. Gossard, and R. E. Muller, "ErAs:GaAs photomixer with two-decade tunability and 12 μW peak output power," *Appl. Phys. Lett.* **85** no. 18, (2004) 3983–3985.

[41] J. D. Zimmerman, E. R. Brown, and A. C. Gossard, "Tunable all epitaxial semimetal-semiconductor schottky diode system: ErAs on InAlGaAs," *J. Vac. Sci. Tech., B* **23** no. 5, (2005) 1929–1935.

[42] S. Preu, S. Malzer, G. H. Döhler, H. Lu, A. C. Gossard, and L. J. Wang, "Efficient III–V tunneling diodes with ErAs recombination centers," *Semicond. Sci. Tech.* **25** no. 11, (2010) 115004.

[43] AM1.5 spectrum is available from the National Renewable Energy Laboratory website: http://rredc.nrel.gov/solar/spectra/am1.5/.

[44] W. Shockley and H. J. Queisser, "Detailed balance limit of efficiency of p–n junction solar cells," *J. Appl. Phys.* **32** no. 3, (1961) 510–519.

[45] C. Amano, H. Sugiura, A. Yamamoto, and M. Yamaguchi, "20.2% efficiency $Al_{0.4}Ga_{0.6}As$/GaAs tandem solar cells grown by molecular beam epitaxy," *Appl. Phys. Lett.* **51** no. 24, (1987) 1998–2000.

[46] A. M. Crook, H. P. Nair, and S. R. Bank, "Surface segregation effects of erbium in GaAs and implications for optical devices containing ErAs nanostructures," *Appl. Phys. Lett.* **98** (Mar., 2011) 121108.

[47] M. W. Wiemer, H. B. Yuen, V. A. Sabnis, M. J. Sheldon, and D. Fushman, "Functional integration of dilute nitrides into high efficiency III-V solar cells," June, 2010. US Patent Application No: 12/819,534.

[48] S. Arafin, A. Bachmann, K. Kashani-Shirazi, and M.-C. Amann, "Electrically pumped continuous-wave vertical-cavity surface-emitting lasers at $\sim$2.6 μm," *Applied Physics Letters* **95** no. 13, (2009) 131120–3.

[49] M. G. Peters, B. J. Thibeault, D. B. Young, J. W. Scott, F. H. Peters, A. C. Gossard, and L. A. Coldren, "Band-gap engineered digital alloy interfaces for lower resistance vertical-cavity surface-emitting lasers," *Appl. Phys. Lett.* **63** no. 25, (1993) 3411–3413.

[50] H. P. Nair, A. M. Crook, and S. R. Bank, "Enhanced conductivity of tunnel junctions employing semimetallic nanoparticles through variation in growth temperature and deposition," *Appl. Phys. Lett.* **96** no. 22, (2010) 222104.

[51] K. Petrov, S. Waltman, E. Dlugokencky, M. Arbore, M. Fejer, F. Tittel, and L. Hollberg, "Precise measurement of methane in air using diode-pumped 3.4 μm difference-frequency generation in PPLN," *Appl. Phys. B* **64** (1997) 567–572.

[52] P. Werle, K. Maurer, R. Kormann, R. Mücke, F. D'Amato, T. Lancia, and A. Popov, "Spectroscopic gas analyzers based on indium-phosphide, antimonide and lead-salt diode-lasers," *Spectrochem. Acta. A* **58** no. 11, (2002) 2361–2372.

[53] G. Belenky and L. Vorobiev, "Studies of heavily strained and strain-compensated type-I GaSb based heterostructures for

development of high efficiency coherent sources operating in the range of $2.3 - 3.5\,\mu$m," *Defense Technical Information Center* (June, 2005) 1–11.

[54] M. Wolbarsht, "Laser surgery: CO_2 or HF," *IEEE J. Quantum Electron.* **20** no. 12, (Dec., 1984) 1427–1432.

[55] J. Rattunde, C. Mermelstein, R. Keifer, and J. Wagner, *Mid-infrared Semiconductor Optoelectronics*. Springer, 2006.

[56] G. Kipshidze, T. Hosoda, W. Sarney, L. Shterengas, and G. Belenky, "High-power $2.2\,\mu$m diode lasers with metamorphic arsenic-free heterostructures," **23** no. 5, (Mar, 2011) 317–319.

[57] S. Bank, H. Bae, L. Goddard, H. Yuen, M. Wistey, R. Kudrawiec, and J. Harris, "Recent progress on $1.55\,\mu$m dilute-nitride lasers," *IEEE J. Quantum Electron.* **43** no. 9, (2007) 773 –785.

[58] L. Buckle, B. Bennett, S. Jollands, T. Veal, N. Wilson, B. Murdin, C. McConville, and T. Ashley, "Growth of dilute GaNSb by plasma-assisted MBE," *J. Crys. Growth* **278** no. 1-4, (2005) 188 – 192. 13th International Conference on Molecular Beam Epitaxy.

[59] W. Shan, W. Walukiewicz, J. W. Ager, E. E. Haller, J. F. Geisz, D. J. Friedman, J. M. Olson, and S. R. Kurtz, "Band anticrossing in GaInNAs alloys," *Phys. Rev. Lett.* **82** no. 6, (Feb., 1999) 1221–1224.

[60] D. Z. Garbuzov, R. U. Martinelli, H. Lee, P. K. York, R. J. Menna, J. C. Connolly, and S. Y. Narayan, "Ultralow-loss broadened-waveguide high-power 2 μm AlGaAsSb/InGaAsSb/GaSb separate-confinement quantum-well lasers," *Appl. Phys. Lett.* **69** no. 14, (1996) 2006–2008.

[61] G. Belenky, L. Shterengas, D. Wang, G. Kipshidze, and L. Vorobjev, "Continuous wave operated 3.2 μm type-I quantum-well diode lasers with the quinary waveguide layer," *Semicond. Sci. Tech.* **24** no. 11, (2009) 115013.

[62] D. Z. Garbuzov, R. U. Martinelli, H. Lee, R. J. Menna, P. K. York, L. A. DiMarco, M. G. Harvey, R. J. Matarese, S. Y. Narayan, and J. C. Connolly, "4 W quasi-continuous-wave output power from 2 μm AlGaAsSb/InGaAsSb single-quantum-well broadened waveguide laser diodes," *Appl. Phys. Lett.* **70** no. 22, (1997) 2931–2933.

[63] T. Hosoda, G. Kipshidze, L. Shterengas, and G. Belenky, "Diode lasers emitting near 3.44 μm in continuous-wave regime at 300 K," *Electron. Lett.* **46** no. 21, (Oct., 2010) 1455–1457.

[64] W. L. Barnes, A. Dereux, and T. W. Ebbesen, "Surface plasmon subwavelength optics," *Nature* **424** no. 6950, (Aug, 2003) 824–830.

[65] S. Nie and S. R. Emory, "Probing single molecules and single nanoparticles by surface-enhanced raman scattering," *Science* **275** no. 5303, (Feb, 1997) 1102–1106.

[66] K. Li, M. I. Stockman, and D. J. Bergman, "Self-similar chain of metal nanospheres as an efficient nanolens," *Phys. Rev. Lett.* **91** no. 22, (Nov, 2003) 227402.

[67] T. Kalkbrenner, M. Ramstein, J. Mlynek, and V. Sandoghdar, "A single gold particle as a probe for apertureless scanning near-field optical microscopy," *J. Microsc.* **202** no. 1, (2001) 72–76.

[68] D. M. Schaadt, B. Feng, and E. T. Yu, "Enhanced semiconductor optical absorption via surface plasmon excitation in metal nanoparticles," *Appl. Phys. Lett.* **86** no. 6, (2005) 063106.

[69] J. Vuckovic, M. Loncar, and A. Scherer, "Surface plasmon enhanced light-emitting diode," *IEEE J. Quantum Electron.* **36** no. 10, (Oct, 2000) 1131–1144.

[70] E. R. Brown, A. Bacher, D. Driscoll, M. Hanson, C. Kadow, and A. C. Gossard, "Evidence for a strong surface-plasmon resonance on ErAs nanoparticles in GaAs," *Phys. Rev. Lett.* **90** no. 7, (Feb, 2003) 077403.

[71] M. A. Scarpulla, J. M. O. Zide, J. M. LeBeau, C. G. V. de Walle, A. C. Gossard, and K. T. Delaney, "Near-infrared absorption and semimetal-semiconductor transition in 2 nm ErAs nanoparticles embedded in gaas and alas," *Appl. Phys. Lett.* **92** no. 17, (2008) 173116.

[72] M. P. Hanson, A. C. Gossard, and E. R. Brown, "Infrared surface plasmon resonances due to Er-V semimetallic nanoparticles in III-V semiconductor matrices," *Journal of Applied Physics* **102** no. 4, (2007) 043112–8.

[73] A. C. Young, J. D. Zimmerman, E. R. Brown, and A. C. Gossard, "1/f noise in all-epitaxial metal-semiconductor diodes," *Appl. Phys. Lett.* **88** no. 7, (2006) 073518.

[74] U. Singisetti, J. D. Zimmerman, M. A. Wistey, J. Cagnon, B. J. Thibeault, M. J. W. Rodwell, A. C. Gossard, S. Stemmer, and S. R. Bank, "ErAs epitaxial Ohmic contacts to InGaAs/InP," *Appl. Phys. Lett.* **94** no. 8, (Feb., 2009) 083505 –083505–3.

[75] A. M. Crook, H. P. Nair, D. A. Ferrer, and S. R. Bank, "Suppression of planar defects in the molecular beam epitaxial growth of GaAs/ErAs/GaAs heterostructures," *Appl. Phys. Lett.* **99** no. 7, (2011) 072120.

[76] J. P. A. van der Wagt, *Reflection High-Engery Electron Diffraction During Molecular-Beam Epitaxy*. PhD thesis, Stanford, 1995.

[77] B. A. Joyce, "Molecular beam epitaxy," *Reports on Progress in Physics* **48** no. 12, (1985) 1637.

[78] A. Cho, *Molecular Beam Epitaxy*. American Institue of Physics, 1994.

[79] E. Larkins and J. Haris Jr., *Molecular Beam Epitaxy of High-quality GaAs and AlGaAs*. Noyes Publications, 1995.

[80] K. Cheng, "Molecular beam epitaxy technology of III-V compound semiconductors for optoelectronic applications," **85** no. 11, (Nov., 1997) 1694–1714.

[81] Q. Xie, J. E. V. Nostrand, J. L. Brown, and C. E. Stutz, "Arsenic for antimony exchange on gasb, its impacts on surface morphology, and interface structure," *J. Appl. Phys.* **86** no. 1, (1999) 329–37.

[82] R. Kaspi, W. T. Cooley, and K. R. Evans, "In situ composition control of III-$As_{1-x}Sb_x$ alloys during molecular beam epitaxy using line-of-sight mass spectrometry," *J. Crys. Growth* **173** no. 1-2, (1997) 5–13.

[83] E. Selvig, B. O. Fimland, T. Skauli, and R. Haakenaasen, "Calibration of the arsenic mole fraction in mbe grown $GaAs_ySb_{1-y}$ and $Al_xGa_{1-x}As_ySb_{1-y}$ (y<0.2)," *J. Crys. Growth* **227-228** (2001) 562 – 565.

[84] G. Almuneau, E. Hall, S. Mathis, and L. A. Coldren, "Accurate control of Sb composition in AlGaAsSb alloys on InP substrates by molecular beam epitaxy," *J. Crys. Growth* **208** no. 1-4, (2000) 113 – 116.

[85] P. Gopaladasu, J. L. Cecchi, K. J. Malloy, and R. Kaspi, "Response surface modeling of the composition of $AlAs_ySb_{1-y}$ alloys grown by molecular beam epitaxy," *J. Crys. Growth* **225** no. 2-4, (2001) 556–560.

[86] A. Semenov, V. Sorokin, V. Solov'ev, B. Mel'tser, and S. Ivanov, "Special features of Sb_2 and Sb_4 incorporation in MBE-grown AlGaAsSb alloys," *Semiconductors* **38** no. 3, (2004) 266–272.

[87] J. G. Kim, L. Shterengas, R. U. Martinelli, and G. L. Belenky, "High-power room-temperature continuous wave operation of 2.7 and 2.8 μm In(Al)GaAsSb/GaSb diode lasers," *Appl. Phys. Lett.* **83** no. 10, (2003) 1926–1928.

[88] S. Simanowski, C. Mermelstein, M. Walther, N. Herres, R. Kiefer, M. Rattunde, J. Schmitz, J. Wagner, and G. Weimann, "Growth and layer structure optimization of 2.26 μm (AlGaIn)(AsSb) diode lasers for room temperature operation," *J. Crys. Growth* **227-228** (2001) 595–599.

[89] S. Simanowski, M. Walther, J. Schmitz, R. Kiefer, N. Herres, F. Fuchs, M. Maier, C. Mermelstein, J. Wagner, and G. Weimann, "Arsenic incorporation in molecular beam epitaxy (MBE) grown (AlGaIn)(AsSb) layers for $2.0 - 2.5\,\mu$m laser structures on GaSb substrates," *J. Crys. Growth* **201-202** (1999) 849 – 853.

[90] S. Simanowski, N. Herres, C. Mermelstein, R. Kiefer, J. Schmitz, M. Walther, J. Wagner, and G. Weimann, "Strain adjustment in (GaIn)(AsSb)/(AlGa)(AsSb) QWs for $2.3 - 2.7\,\mu$m laser structures," *J. Crys. Growth* **209** no. 1, (2000) 15 – 20.

[91] C. E. C. Wood and B. A. Joyce, "Tin-doping effects in GaAs films grown by molecular beam epitaxy," *J. Appl. Phys.* **49** no. 9, (1978) 4954–4961.

[92] J. J. Harris, D. E. Ashenford, C. T. Foxon, P. J. Dobson, and B. A. Joyce, "Kinetic limitations to surface segregation during MBE growth of III-V compounds: Sn in GaAs," *Appl. Phys., A* **33** (1984) 87–92. 10.1007/BF00617613.

[93] S. Naritsuka, O. Kobayashi, and T. Maruyama, "Numerical model for oxygen incorporation into AlGaAs layer grown by molecular beam epitaxy," *Jap. J. Appl. Phys.* **42** no. Part 2, No. 9A/B, (2003) L1041–L1043.

[94] J. F. Xu, P. M. Thibado, C. Awo-Affouda, F. Ramos, and V. P. LaBella, "Anomalous Mn depth profiles for GaMnAs/GaAs(001) thin films grown by molecular beam epitaxy," *J. Vac. Sci. Tech., B* **25** no. 4, (2007) 1476–1480.

[95] R. Serna, M. Lohmeier, P. M. Zagwijn, E. Vlieg, and A. Polman, "Segregation and trapping of erbium during silicon molecular beam epitaxy," *Appl. Phys. Lett.* **66** no. 11, (1995) 1385–1387.

[96] J. Moison, F. Houzay, F. Barthe, J. Gérard, B. Jusserand, J. Massies, and F. Turco-Sandroff, "Surface segregation in III-V alloys," *J. Crys. Growth* **111** no. 1-4, (1991) 141–150.

[97] A. J. Noreika, W. J. Takei, M. H. Francombe, and C. E. C. Wood, "Indium antimonide-bismuth compositions grown by molecular beam epitaxy," *J. Appl. Phys.* **53** no. 7, (1982) 4932–4937.

[98] H. Morkoç, C. Hopkins, C. A. Evans, and A. Y. Cho, "Chromium and tellurium redistribution in GaAs and $Al_{0.3}Ga_{0.7}As$ grown by molecular beam epitaxy," *J. Appl. Phys.* **51** no. 11, (1980) 5986–5991.

[99] S. Naritsuka, O. Kobayashi, K. Mitsuda, and T. Nishinaga, "Oxygen incorporation mechanism in AlGaAs layers grown by molecular beam epitaxy," *J. Crys. Growth* **254** no. 3-4, (2003) 310–315.

[100] S. R. Bank, *High-Performance* 1.55 μm *GaInNAsSb lasers grown on GaAs.* PhD thesis, Stanford University, 2006.

[101] A. J. Ptak, D. J. Friedman, and S. Kurtz, "Effects of temperature, nitrogen ions, and antimony on wide depletion width GaInNAs," *J. Vac. Sci. Tech., B* **25** no. 3, (2007) 955–959.

[102] M. A. Wistey, S. R. Bank, H. B. Yuen, H. Bae, J. S. Harris, and Jr., "Nitrogen plasma optimization for high-quality dilute nitrides," *J. Crys. Growth* **278** no. 1-4, (2005) 229 – 233. 13th International Conference on Molecular Beam Epitaxy.

[103] M. M. Oye, T. J. Mattord, G. A. Hallock, S. R. Bank, M. A. Wistey, J. M. Reifsnider, A. J. Ptak, H. B. Yuen, J. James S. Harris, and J. Archie L. Holmes, "Effects of different plasma species (atomic N,

metastable N_2^*, and ions) on the optical properties of dilute nitride materials grown by plasma-assisted molecular-beam epitaxy," *Appl. Phys. Lett.* **91** no. 19, (2007) 191903.

[104] H. P. Nair, A. M. Crook, K. M. Yu, and S. R. Bank, "Structural and optical studies of nitrogen incorporation into GaSb-based GaInSb quantum wells," *Appl. Phys. Lett.* **100** no. 2, (2012) 021103.

[105] S. B. Zhang and S.-H. Wei, "Nitrogen solubility and induced defect complexes in epitaxial GaAs:N," *Phys. Rev. Lett.* **86** no. 9, (Feb., 2001) 1789–1792.

[106] P. Krispin, S. G. Spruytte, J. S. Harris, and K. H. Ploog, "Electron traps in Ga(As,N) layers grown by molecular-beam epitaxy," *Appl. Phys. Lett.* **80** no. 12, (2002) 2120–2122.

[107] J. S. Harris, R. Kudrawiec, H. B. Yuen, S. R. Bank, H. P. Bae, M. A. Wistey, D. Jackrel, E. R. Pickett, T. Sarmiento, L. L. Goddard, V. Lordi, and T. Gugov, "Development of GaInNAsSb alloys: Growth, band structure, optical properties and applications," *Phys. Stat. Sol. (b)* **244** no. 8, (July, 2007) 2707–2729.

[108] D. W. Elsaesser, Y. K. Yeo, R. L. Hengehold, K. R. Evans, and F. L. Pedrotti, "Er-related deep centers in GaAs doped with Er by ion implantation and molecular beam epitaxy," *J. Appl. Phys.* **77** no. 8, (1995) 3919–3926.

[109] H. Cotal, C. Fetzer, J. Boisvert, G. Kinsey, R. King, P. Hebert, H. Yoon, and N. Karam, "III-V multijunction solar cells for concentrating photovoltaics," *Energy Environ. Sci.* **2** no. 2, (2009) 174–192.

[110] G. Almuneau, E. Hall, S. Nakagawa, J. K. Kim, D. Lofgreen, O. Sjolund, C. Luo, D. R. Clarke, J. H. English, and L. A. Coldren, "Molecular beam epitaxial growth of monolithic 1.55 μm vertical cavity surface emitting lasers with AlGaAsSb/AlAsSb bragg mirrors," *J. Vac. Sci. Tech., B* **18** no. 3, (2000) 1601–1604.

[111] G. Belenky, L. Shterengas, D. Donetsky, M. Kisin, and G. Kipshidze, "Advances in type-i gasb based lasers," *Jap. J. Appl. Phys.* **47** no. 10, (2008) 8236–8238.

[112] T. Hosoda, G. Belenky, L. Shterengas, G. Kipshidze, and M. V. Kisin, "Continuous-wave room temperature operated 3.0 μm type-I GaSb-based lasers with quinternary AlInGaAsSb barriers," *Appl. Phys. Lett.* **92** no. 9, (2008) 091106.

[113] D. Garbuzov, H. Lee, V. Khalfin, R. Martinelli, J. Connolly, and G. Belenky, "$2.3 - 2.7\,\mu$m room temperature CW operation of InGaAsSb-AlGaAsSb broad waveguide SCH-QW diode lasers," **11** no. 7, (Jul, 1999) 794 –796.

[114] L. Esaki, "New phenomenon in narrow germainu $p - n$ junctions," *Phys. Rev.* **109** no. 2, (Jan, 1958) 603–604.

[115] S. M. Sze and K. K. Ng, *Physics of Semiconductor Devices*. Wiley Interscience, 3rd ed., 2007.

[116] O. Dier, M. Sterkel, M. Grau, C. Lin, C. Lauer, and M.-C. Amann, "Tunnel junctions for ohmic intra-device contacts on GaSb-substrates," *Appl. Phys. Lett.* **85** no. 12, (2004) 2388–2389.

[117] A. Bachmann, S. Arafin, and K. Kashani-Shirazi, "Single-mode electrically pumped GaSb-based VCSELs emitting continuous-wave at 2.4 and 2.6 μm," *New Journal of Physics* **11** no. 12, (2009) 125014.

[118] I. Vurgaftman, C. L. Canedy, C. S. Kim, M. Kim, W. W. Bewley, J. R. Lindle, J. Abell, and J. R. Meyer, "Mid-infrared interband cascade lasers operating at ambient temperatures," *New J. Phys.* **11** no. 12, (2009) 125015.

[119] S. Ahmed, M. R. Melloch, E. S. Harmon, D. T. McInturff, and J. M. Woodall, "Use of nonstoichiometry to form GaAs tunnel junctions," *Appl. Phys. Lett.* **71** no. 25, (1997) 3667–3669.

[120] C. Kadow, J. A. Johnson, K. Kolstad, and A. C. Gossard, "Growth-temperature dependence of the microstructure of ErAs islands in GaAs," *J. Vac. Sci. Tech., B* **21** no. 1, (2003) 29–32.

[121] C. Kadow, J. A. Johnson, K. Kolstad, J. P. Ibbetson, and A. C. Gossard, "Growth and microstructure of self-assembled ErAs islands in GaAs," *J. Vac. Sci. Tech., B* **18** no. 4, (2000) 2197–2203.

[122] J. J. M. Law, E. T. Yu, G. Koblmüller, F. Wu, and J. S. Speck, "Low defect-mediated reverse-bias leakage in (0001) gan via high-temperature molecular beam epitaxy," *Appl. Phys. Lett.* **96** no. 10, (2010) 102111.

[123] P. Tejedor, L. Díez-Merino, I. Beinik, and C. Teichert, "Conductive atomic force microscopy study of InAs growth kinetics on vicinal GaAs (110)," *Appl. Phys. Lett.* **95** no. 12, (2009) 123103.

[124] B. Galiana, I. Rey-Stolle, I. Beinik, C. Algora, C. Teichert, J. Molina-Aldareguia, and P. Tejedor, "Characterization of antiphase domains on GaAs grown on Ge substrates by conductive atomic force microscopy for photovoltaic applications," *Solar Energy Materials and Solar Cells* **95** no. 7, (2011) 1949–1954.

[125] K. W. Park, V. D. Dasika, H. P. Nair, A. M. Crook, S. R. Bank, and E. T. Yu, "Local current measurement of GaAs pn junctions with embedded ErAs nanoparticles," *submitted to Appl. Phys. Lett.* (2012) .

[126] A. M. Crook, H. P. Nair, and S. R. Bank, "High-performance nanoparticle-enhanced tunnel junctions for photonic devices," *Phys. Stat. Sol. (c)* **7** no. 10, (2010) 2544–2547.

[127] J. Pan, J. McManis, L. Grober, and J. Woodall, "Gallium-arsenide deep-level pin tunnel diode with very negative conductance," *Electronics Letters* **39** no. 19, (2003) 1411–1412.

[128] J. D. Zimmerman, *Growth and use of epitaxially grown ErAs semimetal to enhance III-V Schottky diode and tunnel junction performance*. PhD thesis, University of California, Santa Barbara, Santa Barbara, CA, Mar, 2008.

[129] I. Vurgaftman and J. R. Meyer, "Band parameters for nitrogen-containing semiconductors," *J. Appl. Phys.* **94** no. 6, (2003) 3675–3696.

[130] O. Dier, C. Lauer, and M. C. Amann, "n-InAsSb/p-GaSb tunnel junctions with extremely low resistivity," *Electronics Letters* **42** no. 7, (2006) 419–420.

[131] A. Chandola, R. Pino, and P. S. Dutta, "Below bandgap optical absorption in tellurium-doped GaSb," *Semicond. Sci. Tech.* **20** no. 8, (2005) 886.

[132] D. C. Driscoll, M. Hanson, C. Kadow, and A. C. Gossard, "Electronic structure and conduction in a metal–semiconductor digital composite: ErAs:InGaAs," *Appl. Phys. Lett.* **78** no. 12, (2001) 1703–1705.

[133] Z. Wasilewski, S. Rolfe, and R. Wilson, "Contamination in molecular beam epitaxy: the role of arsenic drag effect," *J. Crys. Growth* **175-176** no. Part 2, (1997) 1270–1277.

[134] F. Ishikawa, S. Wu, M. Kato, M. Uchiyama, K. Higashi, and M. Kondow, "Unintentional aluminum incorporation related to the

introduction of nitrogen gas during the plasma-assisted molecular beam epitaxy," *J. Crys. Growth* **311** no. 7, (2009) 1656–1649.

[135] E. M. Purcell, "Proceedings of the american physical society," *Phys. Rev.* **69** no. 11-12, (June, 1946) 674.

[136] I. Gontijo, M. Boroditsky, E. Yablonovitch, S. Keller, U. K. Mishra, and S. P. DenBaars, "Coupling of InGaN quantum-well photoluminescence to silver surface plasmons," *Phys. Rev. B* **60** no. 16, (Oct., 1999) 11564–11567.

[137] M. Boroditsky, R. Vrijen, T. F. Krauss, R. Coccioli, R. Bhat, and E. Yablonovitch, "Spontaneous emission extraction and purcell enhancement from thin-film 2-D photonic crystals," *J. Lightwave Technol.* **17** no. 11, (Nov, 1999) 2096.

[138] M. P. Hanson, *Erbium-V Semimetal and III-V Semiconductor Composite Materials*. PhD thesis, University of California, Santa Barbara, 2007.

[139] M. Grundmann, "Formation of epitaxial domains: Unified theory and survey of experimental results," *Phys. Stat. Sol. (b)* **248** no. 4, (2011) 805–824.

[140] M. Volmer and A. Weber, "Novel growth mechanism in heteroepitaxial semiconductor growth," *Z. Phys. Chem* **119** no. 277, (1926) 126.

[141] J. G. Zhu, C. J. Palmstrøm, and C. B. Carter, "Lattice matched GaAs/$Sc_{0.3}Er_{0.7}As$/GaAs heterostructures grown on various substrate orientations," *J. Appl. Phys.* **77** no. 9, (1995) 4321–4328.

[142] C. Kadow, *Self-assembled ErAs islands in GaAs for photomixer devices*. PhD thesis, University of California, Santa Barbara, 2000.

[143] D. E. Brehmer, K. Zhang, C. J. Schwarz, S.-P. Chau, S. J. Allen, J. P. Ibbetson, J. P. Zhang, C. J. Palmstrøm, and B. Wilkens, "Resonant tunneling through ErAs semimetal quantum wells," *Appl. Phys. Lett.* **67** no. 9, (1995) 1268–1270.

[144] H. Sakaki, T. Noda, K. Hirakawa, M. Tanaka, and T. Matsusue, "Interface roughness scattering in GaAs/AlAs quantum wells," *Appl. Phys. Lett.* **51** no. 23, (Dec, 1987) 1934–1936.